EXPERIMENTAL AND ANALYTICAL STUDIES OF TITANOMAGNETITE IN SYNTHETIC AND NATURAL SAMPLES

A THESIS SUBMITTED TO THE GRADUATE DIVISION OF THE
UNIVERSITY OF HAWAI‘I IN PARTIAL FULFILLMENT
OF THE REQUIREMENTS FOR THE DEGREE OF

MASTER OF SCIENCE

IN

GEOLOGY AND GEOPHYSICS

MAY 2010

By:
Lisa T. Petrochilos

Thesis Committee:

Julia E. Hammer, Chairperson
Michael D. Fuller
Michael O. Garcia

We certify that we have read this thesis and that, in our opinion, it is satisfactory in scope and quality as a thesis for the degree of Master of Science in Geology and Geophysics.

THESIS COMMITTEE

_____
Chairperson

_____

_____

ACKNOWLEDGEMENTS

I am very grateful to Julie Bowles for sharing her experimental sample and data, and her instruction and assistance both at the University of Hawai‘i at Mānoa and the Institute for Rock Magnetism, Minneapolis, MN. Thank to David Cuomo and Stefanie Brachfeld for magnetic measurements of the samples. I would like to thank to Malcom Rutherford for supplying a sample. I also thank to Eric Hellebrand for enormous assistance with EPMA. I appreciate Owen Neill for his support for EPMA and countless other occasions. I also thank to Gary Huss for assistance with SEM. Thanks to Carrie Brugger for advice as a senior student of the “team”. My deepest gratitude goes toward my advisors Julia Hammer and Michael Fuller. I am appreciative the great opportunities that they provided with me and what I learnt through the projects and from them. I would like to thank my committee member Michael Garcia for his advice as an experienced scientist and mentor. Also, I appreciate for copious assistance from my co-authors Pavel Zinin, Lydie Bonal, and Stuart Gilder in every aspect. Special thanks to Nicolas, my partner in life, for moral support, patience, and advice as a professional. Thanks to my friend, Svetlana Natarov for a moral support and sometimes inspiring discussions. Finally, I would like to thank my family in Japan. The projects were funded by NASA Grant NNG05GL92G to JH, IRM Visiting Fellowship to LP, NSF grant EAR0609577 to MF, DFG Grant STA 1026/2-1 to SG.

ABSTRACT

Titanomagnetite is a major rock-forming, spinel-structured oxide mineral that is ubiquitous in a wide range of rock types. Despite its typically small volumetric abundance, titanomagnetite is the chief carrier of magnetic remanence in Earth's crust. Thus, it is a phase of both petrologic and rock magnetic importance. This thesis is a two-part thesis on titanomagnetite. In Part I, experimentally produced titanomagnetite solid solution is subjected to conditions intended to induce subsolidus exsolution. A series of experiments was performed in an attempt to quantify the kinetics of the process and understanding the mechanism by which exsolution occurs. Additional experiments at elevated temperature were performed to evaluate the temperature dependence of the exsolution process. The run products are compared with previously synthesized samples containing exsolved Fe-Ti-Mg-Al oxides in order to constrain the conditions and compositional controls on the exsolution process. Part II is a manuscript that was submitted to the Earth and Planetary Science Letters that describes a technique by which the Ti content of titanomagnetite may be determined by Raman spectroscopy.

TABLE OF CONTENTS

LIST OF TABLES

Part I

Part II

LIST OF FIGURES

Part I

PART I

EXPERIMENTAL EXPLORATION OF TITANOMAGNETITE EXSOLUTION

Collaborators: Julie A. Bowles[1], David M. Cuomo[2], and Stefanie A. Brachfeld[2]

[1] Institute for Rock Magnetism, University of Minnesota
[2] Montclair State University

1. INTRODUCTION

Titanomagnetite ($Fe_{3-x}Ti_xO_4$, $0 \leq x \leq 1$) solid solution exsolution is a compositional unmixing that produces a cloth-textured intergrowth of two unmixed phases whose compositions are close to their end-members, magnetite (Fe_3O_4) and ulvöspinel (Fe_2TiO_4) (Figure 1.1). Titanomagnetites having undergone this exsolution have been observed mainly in massive ore deposits or basic plutonic environment (Price, 1980). However, this type of exsolution is rare in the Earth's crustal because oxidizing conditions favor the so-called oxy-exsolution of titanomagnetite that produces ilmenite 'trellis'-type of lamellae in magnetite (Haggerty, 1991) (Figure 1.1a). Initially homogeneous titanomagnetite grains that have undergone oxy-exsolution are less likely to subsequently produce exsolution, *sensu stricto* (the primary concern of this thesis), because the formation of ilmenite solid solution depletes the host in Ti and reduces the thermodynamic driving force for additional unmixing. Thus, the process by which initially homogeneous igneous titanomagnetite evolves into other phases depends critically on the oxidation state of the system.

One important consequence of the exsolution process is a change in the magnetic character of the rock that hosts titanomagnetite crystals. A recent study (Evans et al., 2006) of the magnetic characteristics of naturally exsolved titanomagnetite confirmed a smaller magnetic domain size in an exsolved sample compared to a non-exsolved sample. Magnetic domain size is important because it contributes to the strength and stability of remanence that a rock may acquire: single-domain (SD) or pseudo-single-domain (PSD) grains are good magnetic remanence recorders, in contrast with large, multidomain (MD) particles. A change in domain state is intrinsic to exsolution: fine magnetite particles in

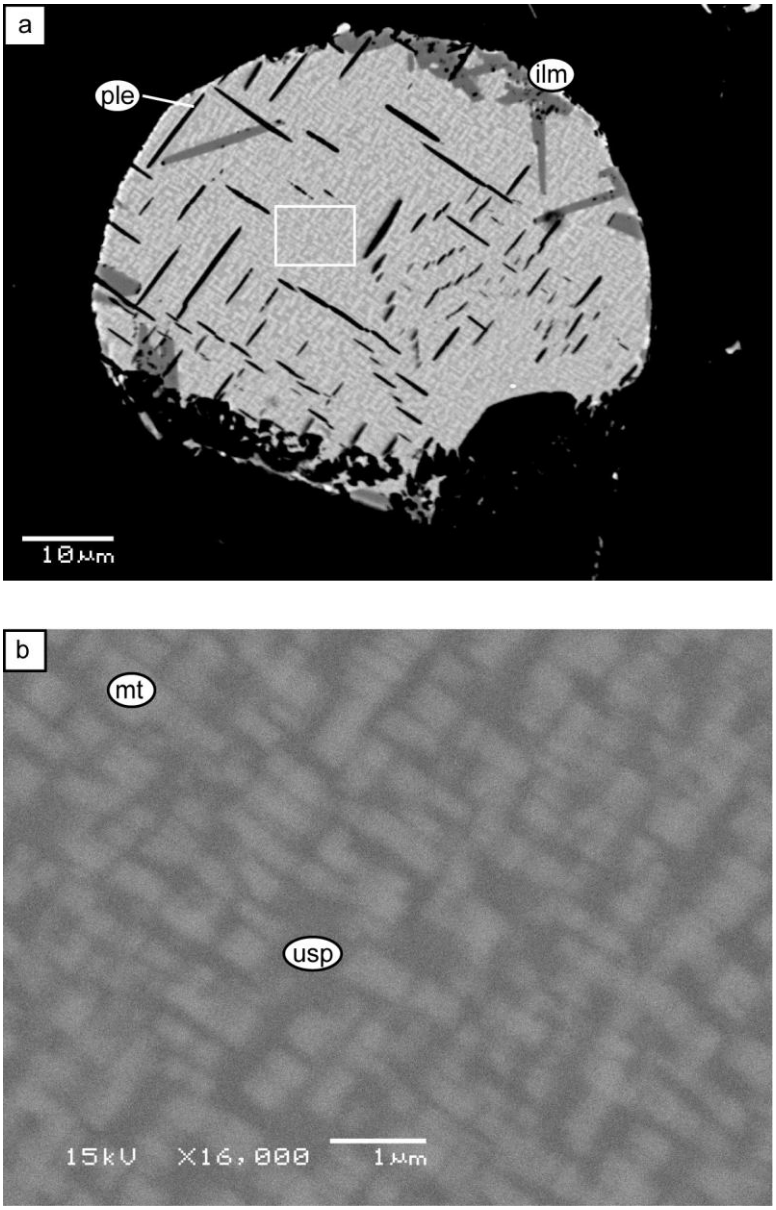

Figure 1.1. Back-scattered electron images of a natural titanomagnetite grain with exsolution and oxy-exsolution. (a): A whole titanomagnetite grain. The exsolved phases are magnetite, ulvöspinel, ilmenite, pleonaste, in the order of increasing darkness. In the BSE images, elements with higher atomic number appear in lighter tone. Cloth texture of the titanomagnetite solid solution exsolution and trellis texture of ilmenite oxy-exsolution are contrasted. (b): A high-magnification image of a region shown with white rectangle in (a), exhibiting prisms of magnetite-rich end-members in ulvöspinel-rich host. The sample is cumberlandite from Rhode Island, kindly provided by MJ Rutherford. The image was obtained using JEOL J5900 scanning electron microscope at University of Hawai‘i at Mānoa. Abbreviations: mt=magnetite, usp=ulvöspinel, ilm=ilmenite, ple=pleonaste.

exsolved titanomagnetite are separated by non-magnetic ulvöspinel matrix. Evans and Wayman (1974) proposed that the dispersed magnetite particles behave as SD grains. However, the link between exsolution textures and magnetic characteristics is not simple. Recent direct observations of the magnetic behavior of exsolved titanomagnetite at the nanometer scale reveal complex magnetostatic interactions between fine magnetite prisms within exsolved grains (Harrison et al., 2002; Feinberg et al., 2006). Such inter-prism magnetic interactions could result in non-uniform magnetizations similar to PSD or MD particles, and could reduce the stability and the intensity of magnetic remanence. The collective behavior of prisms also depends on the degree of separation between the prisms (Muxworthy et al., 2003; Krása et al., 2009). Evans et al. (2006) revisit the sample described by Evans and Wayman (1974), and conclude that although individual prisms are SD in size, hysteresis properties of bulk samples are consistent with SD-PSD domain state. The explanation for this apparent discrepancy revealed by first order reversal curve (FORC) analysis is that magnetostatic interactions increase the effective magnetic domain size.

Intense magnetic anomalies were detected in the crust of Mars by the Global Surveyor spacecraft. Mars no longer possesses a magnetic field, so the magnetization is remarkable not only for its intensity but because it is a remanent magnetization that has persisted for billions of years (Acuña et al., 1998; Acuña et al., 1999; Connerney et al., 1999; Purucker et al., 2000; Connerney et al., 2001). Considering its likely igneous origin, the magnetic remanence in Martian crust is likely to be due to thermoremanent magnetization (TRM). TRM is acquired by magnetic minerals cooled below their Curie temperatures (T_C) in a magnetic field. One possible carrier of strong, stable remanent

magnetization is exsolved titanomagnetite, a mineral that is particularly relevant for the intrusive environment (Hargraves, 2001). The presence of titanomagnetite in Martian meteorites and the moderate oxidation state (corresponding to the solid buffering assemblage range between QFM-3 log units and QFM; Herd et al., 2002; Herd et al., 2006) of the Martian crust make titanomagnetite exsolution a plausible process. Indeed, large (MD-size) grains of titanomagnetite crystallize during slow-cooling of synthetic Martian basalt, as evidenced bycontrolled-atmosphere experiments performed at quartz-fayalite-magnetite (QFM) buffer conditions (Bowles et al., 2009). If these grains subsequently undergo exsolution (without oxidizing), there is potential for attainment of SD-PSD state capable of retaining a strong, stable TRM, as described above. Thus, examination of the exsolution process in the titanomagnetite of candidate basalts is a necessary first step in evaluating this mineral as the primary carrier of the intense magnetization of the Mars crust.

A first-order concern in evaluating the efficacy of exsolution for affecting the thermal remanent magnetization (TRM) of Martian basalt is whether the consolute (i.e., peak solvus) temperature of impurity-bearing titanomagnetite solvus occurs above or below the Curie temperature of exsolved magnetite grains. Early experimental studies of the titanomagnetite solid solution series conclude that this solvus has a consolute point at ~600 ºC or less, with the solvus skewed slightly toward the magnetite end-member (Kawai, 1956; Vincent et al., 1957; Price, 1981; Lindsley, 1981) (Figure 1.2). The T_C of magnetite is near 580 ºC, the T_C of ulvöspinel is -153 ºC, and the T_C of intermediate titanomagnetite compositions are linearly proportional to the ratio of magnetite to ulvöspinel components (Merrill and McElhinny, 1983; Figure 1.2). Therefore, TRM can

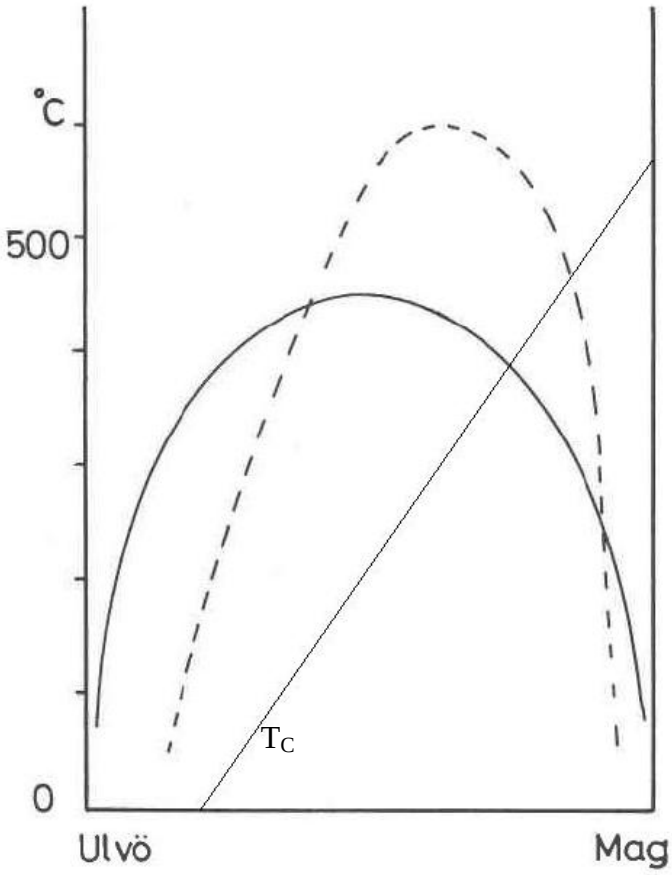

Figure 1.2. A schematic diagram of representative solvi of titanomagnetite solid solution. Curie temperature (T_C) is also shown in the diagram. The solvus in dashed line is suggested by Vincent et al. (1957) and solid line is from Price (1981). Modified from Price (1981) Fig. 1.

be acquired by magnetite that formed due to exsolution at a limited range of temperature ~450-600 ºC according to the solvus of Vincent et al. (1957). However, titanomagnetite in natural systems usually contains some impurities (Deer et al., 1962; Frost and Lindsley, 1991). The consolute temperature of titanomagnetite is presumed higher in Al-bearing oxides, given that the consolute temperature of magnetite-hercynite ($FeAl_2O_4$) solid solution is ~850 ºC (Turnock and Eugster, 1962). The work by Bowles and Hammer, and new data presented here test the hypothesis that oxides forming directly from multicomponent basaltic liquids contain sufficient Al and other cations to drive exsolution at temperatures exceeding T_C, and therefore promote acquisition of TRM of the exsolved magnetite-rich phase.

Other goals motivating this study are the determination of the kinetics and mechanism of titanomagnetite exsolution. Earlier works employed homogenization experiments (Kawai, 1956; Vincent et al., 1957; Price, 1981; Lindsley, 1981) to infer the shape and temperature range of the binary titanomagnetite solvus. In this type of experiment, naturally exsolved titanomagnetite or synthetic mixtures of magnetite and ulvöspinel are annealed at various temperatures and durations to drive homogenization of the two phases. Homogenization experiments allow mapping of the binary solvus in temperature-composition space. However, so-called "forward" experiments, in which an initially homogeneous grain is held at subsolvus temperature to drive exsolution, are needed to address the chemical reaction pathway and rate by which exsolution occurs in nature. No such experiments have been reported in the literature. The difficulty of experimental production of the titanomagnetite exsolution is attributed to sluggish reaction rates at the necessary run temperatures (Harrison and Putnis, 1999).

Elucidating the mechanism by which exsolution usually requires analysis of samples by Transmission Electron Microscopy (TEM) (Putnis, 1992). Two primary mechanisms have been proposed: nucleation and spinodal decomposition (Gibbs, 1961). Nucleation may be either heterogeneous or homogeneous; heterogeneous nucleation occurs when a new phase form at defects (i.e., sample surface and grain boundaries), while homogeneous nucleation occurs in uniform bulk material. Nucleation leads to a texture in which the new phase is discrete, localized in space, and chemically uniform. In contrast, spinodal decomposition leads to a broader, chemically non-uniform distribution of the exsolved phase (Yund and McCallister, 1970). The wavelength of compositional fluctuation in spinodal decomposition is characteristically as small as ~100 Å (Harrison and Putnis, 1999) (Figure 1.3), whereas the spatial scale separating nuclei is in the order of 1000 Å. Note that the exsolution can be either incoherent or coherent, in the later case the lattice planes between new phases and matrix phases remain continuous, and the exsolution texture is in a predictable crystallographic orientation. For instance, the preferred orientation for spinel-structured lamellae forming in a spinel-structured host is along {100} according to the observations of coherent spinodal decomposition in natural and synthetic samples (Harrison and Putnis, 1999; Golla-Schindler et al., 2005). Conditions for which each mechanism takes place are shown in the temperature vs. composition phase diagram (Figure 1.4). Thus, if the mechanism and the end-member compositions of exsolved phases are known, it allows us to map a solvus that corresponds to a particular mechanism as in Figure 1.4 specifically for titanomagnetite solid solution. While nucleation can occur anywhere within the chemical solvus (curve 1 in Figure 1.4), spinodal decomposition is limited to the field within the chemical spinodal (curve 2 in

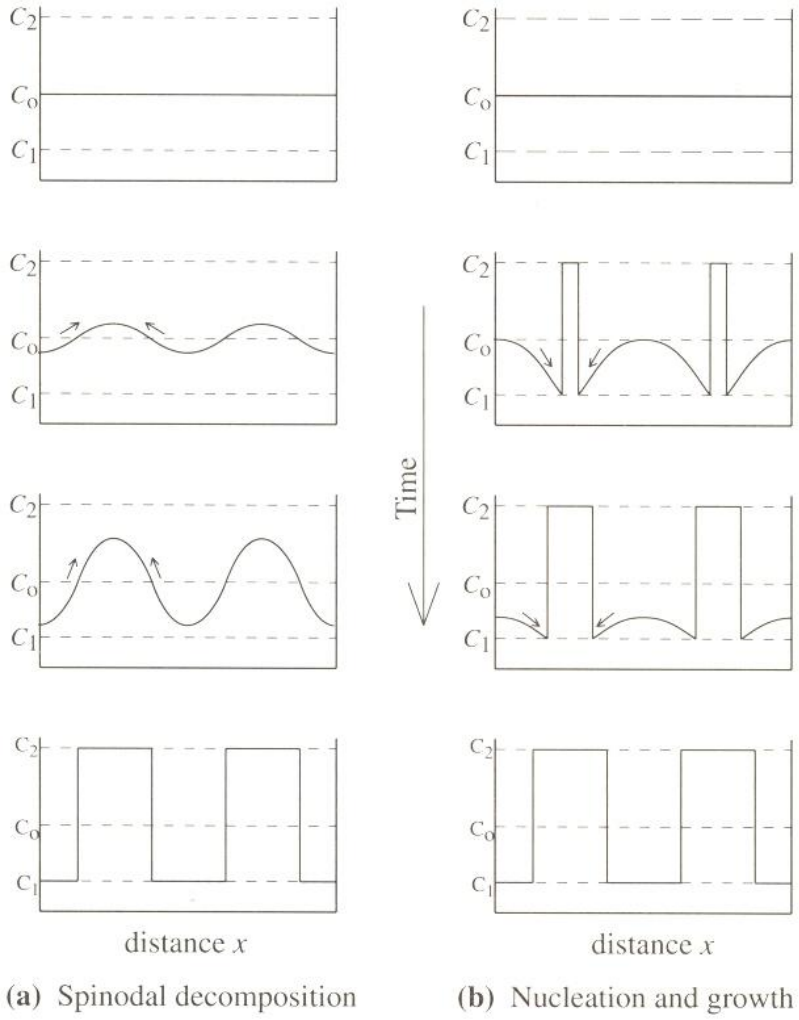

Figure 1.3. A schematic diagram of a development of compositional fluctuations in two mechanisms of exsolution. The distance axes are arbitrary: the wavelength for (a) is shorter relative to (b). C_0 is the initial composition of the solid solution and C_1 and C_2 are the equilibrium compositions of the exsolved two-phase intergrowth. Adapted from Putnis (1992) Figure 11.38.

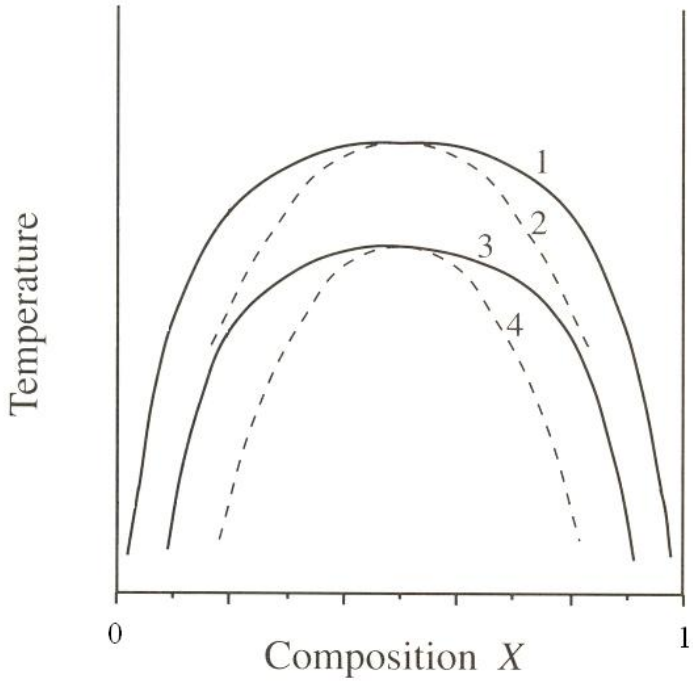

Figure 1.4. A schematic diagram of a chemical (incoherent) and coherent solvi and spinodals. The numbers represent: (1) the chemical solvus, (2) the chemical spinodal, (3) the coherent solvus, and (4) the coherent spinodal. Modified from Putnis (1992) Figure 11.40.

Figure 1.4). Furthermore, coherent exsolution is constrained at lower temperature due to strain energy contributing to the free energy of the solid solution. The upper limit boundaries under which coherent nucleation or spinodal decomposition can take place are defined as the coherent solvus and spinodal (curves 3 and 4 in Figure 1.4).

To date, the kinetics of spinel oxide exsolution are unconstrained by experiment or theory. By comparison, clinopyroxene exsolution is a well investigated and similar problem (Weinbruch et al., 2003). However, even for clinopyroxene, no consensus on rate laws has emerged. The conventional determination of the kinetics of exsolution uses the wavelength of exsolution lamellae, measured by TEM. Because TEM analysis is beyond the scope of this work, we sought to observe development of exsolution by either the nucleation or spinodal decomposition mechanism through evolution of the bulk magnetic properties of samples created in time-series experiments. We anticipated that T_C would help identify the mechanism. Because T_C corresponds closely to the compositions of magnetic minerals, changes in bulk T_C could indicate the emergence of titanomagnetite or magnetite during the incipient stages of exsolution. Theory predicts that if the exsolving phase evolves gradually from titanomagnetite toward magnetite with increasing volume fraction at a given temperature, then the exsolution mechanism is spinodal decomposition. Conversely, if the exsolving phase composition is immediately rich in the magnetite component and unvarying through time, then the mechanism is more consistent with the nucleation mechanism.

JA Bowles and JE Hammer conducted exsolution experiments to test whether the consolute temperature of non-pure titanomagnetite solvus is indeed higher than for pure titanomagnetite, and to evaluate the ability of exsolved titanomagnetite to acquire TRM.

Two starting materials were utilized: basalts synthesized having the compositional character of (a) the SNC meteorites, and (b) the Martian surface ascertained by Thermal Emission Spectroscopy (TES) applied to Martian surface similarly to the previous experimental study by Bowles et al. (2009). The results included observation of micrometer scale exsolution textures in oxide phases and changes in bulk magnetic properties compared to the starting materials. These experiments will be termed "Group 1" of which a representative pair has been selected for detailed analyses in this study: samples MAm-E-03 and MB2-E-03. The starting materials for these runs are samples MAm-36 and MB2-31, respectively. Both the starting materials and run products were characterized petrologically and magnetically in this study.

New time-series experiments (MAm/MB2 -E-09 – E-13) were conducted to infer exsolution mechanisms and investigate the time-dependent changes with a growth of the exsolution texture, as described above. In addition, two sets of experiments (MAm/MB2 -E-14 – E-15) were conducted at different temperatures as a part of a planned series of experiments in which temperature is the primary variable. The new exsolution experiments are conceived similarly to the Group 1 experiments (with important differences to be described in detail in this thesis), and termed Group 2 experiments. Group 2 also employed two bulk compositions (MAm-51 and MB2-48) based on the characteristics of the SNC meteorites and TES basalts, with the intention of matching the starting materials used in Group 1.

The ensuing sections of Part I of this thesis provide detailed experimental methods, petrologic and magnetic analytical results, new constraints on the position of the solvus in multicomponent Fe-Ti-Al-Mg spinel-structured oxide, and discussion of

titanomagnetite exsolution occuring in both pilot (Group 1) and follow-on (Group 2) experiments.

2. METHODS

2.1 Experimental Methods

2.1.1 Starting Material Synthesis

The steps of starting material synthesis procedure are summarized as follows, where the product for each step is denoted in parentheses.

(1) Mixing of raw reagent powders (reagent mixture)

(2) Fusion of reagent mixtures to check composition (fused glass beads)

(3) Conditioning of reagent mixtures to reduce Fe and drive off CO_2 (conditioned reagent)

(4) Conditioning of a Pt crucible with Fe (conditioned crucible)

(5) High temperature treatment on conditioned reagents for production of starting materials for subsolidus annealing experiments, or exsolution experiments (crystalline starting materials)

The procedure is the same for Groups 1 and 2 experiments except where noted.

2.1.1.1 Starting Material Composition Selection

The starting materials with two different bulk compositions were employed for the Groups 2 experiments similarly to Group 1. They are namely ‘meteorite-type’ or ‘M-type’ composition and ‘terrestrial-type’ or ‘T-type’ composition, where the former is characteristically Fe-rich and Al-poor (atomic ratio Fe/Al = 1.5) and the latter has an opposite nature to the former (Fe/Al = 0.4). The values of wt.% for all other elements except Ca are the same for both compositions (Table 2.1). The purpose of having two different bulk compositions was to cover a range of possible compositions of basaltic crustal materials in Mars. Although T-type composition has recently been suggested to be

Table 2.1. Bulk compositions of starting materials and CIPW normative mineralogy

	Meteorite-type			Terrestrial-type		
			Groups 1, 2		Group 1	Group 2
	A*[a]	A*mod[b]	MAm-34	B2[b]	MB2-30	MB2-50
SiO_2	51.40	51.16	53.64	51.20	52.31	43.08
TiO_2	1.63	1.61	1.30	1.60	1.47	2.28
Al_2O_3	9.13	8.70	8.99	17.01	16.65	20.89
FeO(t)	18.90	18.90	17.69	8.48	8.53	8.40
MnO	-	0.53	0.48	0.53	0.50	0.59
MgO	7.27	7.04	6.32	7.04	7.46	8.84
CaO	8.77	8.44	8.48	10.50	10.36	13.35
Na_2O	2.13	2.28	1.88	2.28	2.00	1.56
K_2O	0.75	0.76	0.75	0.76	0.71	0.52
P_2O_5	0.49	0.50	0.50	0.50	0.47	0.52
Cr_2O_3	-	0.10	0.04	0.10	0.04	0.03
Total	100.5	100.0	100.1	100.0	100.5	100.1
Fe/Al	1.47	1.54	1.40	0.35	0.36	0.29
Normative mineralogy[c]						
Quartz	2.73	2.97	8.92	1.97	4.14	0.00
Total feldspar	35.29	35.02	34.06	57.66	55.12	59.64
Total feldspathoid	0.00	0.00	0.00	0.00	0.00	2.68
Total pyroxene	53.25	52.60	48.15	34.07	34.81	11.60
Olivine	0.00	0.00	0.00	0.00	0.00	18.60
Apatite	1.06	1.09	1.09	1.09	1.02	1.13
Ilmenite	3.08	2.21	2.46	3.04	2.78	4.33
Magnetite	4.53	5.93	5.27	2.08	2.05	2.00

[a] SNC-like composition used in Hammer (2006) and Brachfeld and Hammer (2006).

[b] Desired SNC-like and Earth-like composition for this study, which was also used in Bowles et al. (2009).

[c] FeO and Fe_2O_3 were computed from FeO(t) using method of Kilinc et al. (1983) and assuming 1200 °C and fO_2 at QFM for the samples with superscripts a and b (Bowles et al., 2009), and 1070 °C and QFM for the rest. The program Magma by Wholetz was used for the CIPW norm calculation for the last group.

unlikely composition for the most of the Martian crust (McSween et al., 2009), it will still be introduced here as a part of our work. The selection of compositions, chemical characteristics, and CIPW normative mineralogies of the starting materials are described in detail in Bowles et al. (2009).

2.1.1.2 Mixing of Reagents

The starting materials were synthesized from powdered oxide, carbonate, and phosphate reagents. First, the target oxide wt.% values of the starting material was converted into proportions of weights of the reagent powders and a Microsoft Excel spreadsheet was prepared for calculation. This was used to calculate the target weights for each reagent given a desired total weight of the mixture. Then, slightly excessive amounts of the reagents were placed in Coors porcelain crucibles with lids (~4-cm-tall) individually and then held in an oven (Type F6000 Furnace, Barnstead International) at temperatures and durations specific to reagents to eliminate hydration and carbonation (Appendix A). At the end of the heating treatment, the reagents were taken out from the oven and placed in a portable desiccator to transport to another oven (single wall laboratory oven, Blue M) at ~100 ºC or a desiccator in which the reagents were kept. The least hygroscopic reagents were the first to go through this procedure, and the most hygroscopic reagent MgO was the last. The reagents were taken out of the oven or the desiccator and transported to the scale for weighing using a portable desiccator. The same scale (AG 135, Mettler Toledo) was used for all weighing procedures in this study. The hygroscopic reagents were the first to be weighed. The actual weight of MgO (the first reagent weighed) was used to obtain the target weights of the rest of the reagents using the spreadsheet. The reagents were weighed in turn and were immediately poured into a

mortar half-filled with ethanol to avoid an escape of the powders. The reagents in the mortar were gently mixed with a pestle to obtain a homogeneous mixture. The mortar was lightly covered with a piece of paper to avoid contamination, and was placed on the top of the oven (Blue M) at ~30 ºC for a few hours to hasten the ethanol evaporation from the mixture, then stored in a desiccator. Only reagent mixture for T-type sample was prepared for Group 2 sample. The same reagent mixture as Group 1 experiment was used for Group 2 M-type sample (Table 2.1).

Fused glass beads of the each reagent mixture were produced to obtain more accurate composition (Table 2.1) compared to the composition obtained from weights of the reagents (Appendix B). The fusion was conducted at 1215 ºC for M-type (sample MAm-34) and 1280 ºC for T-type (sample MB2-30) for Group 1 by Bowles. It was conducted at 1340 ºC for Group 2 T-type material (sample MB2-50). They are all above liquidus (T_L) obtained using MELTS algorithm (Ghiorso and Sack, 1995). They were conducted at quartz-fayalite-magnetite (QFM) buffer curve using a Deltech furnace with flowing H_2-CO_2 to control fO_2. The detailed settings and procedures for Deltech furnace are described in Appendices C and D. The sample ~0.005 g was held at the experimental condition for 1, 1, and 2 h for each mixture, and drop-quenched (Table 2.2). The temperature and duration were considered to be sufficient to obtain homogeneous, crystal-free melt and yet not enough for significant amount of Fe in the sample to migrate toward Pt wire on which the sample was placed. This migration of Fe to Pt will be discussed in detail in section 2.1.1.4. The temperature and duration values for the latter T-type material were higher than the ones used for the former because the former had not been analyzed and suspected to be insufficiently heated to obtain a homogeneous mixture.

Table 2.2. Sample experimental parameters and petrologic data

Sample[a]	Reagent batch#	Expt group#	Kind	Starting material	Sample container	Recovered sample mass [g]	Buffer/Monior[b]	T_f[c] [ºC]	Duration [day]	Phases[d]	Exsolution types[e]
Meteorite-type:											
MAm-34	1	1, 2	fused bead	n.a.	Pt wire	~0.005	none	1215	1 h	gl, timt (tr.)	n.a.
MAm-36	1	1	crystalline starting material	n.a.	Pt capsule	0.2760	fay+qtz+mt	1065	100 h	cpx, gl, hem, femgal, pl	n.a.
MAm-51	1	2	crystalline starting material	n.a.	Pt crucible	3.0215	sensor	1070	100 h	cpx, gl, pl, timt	n.a.
MAm-E-03	1	1	group 1 representative	MAm-36	Ag capsule	n.d.	fayalite	710	54	cpx, gl, mt, timt, femgal, femg, pl, [gl*], ol? (t.r.)	1, 2
MAm-E-09	1	2	time-series	Mam-51	Ag capsule	0.1477	fay+qtz+mt, Fe powder	650	21	cpx, gl, pl, timt, gl*	none
MAm-E-10	1	2	time-series	Mam-51	Ag capsule	0.1418	fay+qtz+mt, Fe powder	650	32	cpx, gl, pl, timt, gl*	none
MAm-E-11	1	2	time-series	Mam-51	Ag capsule	0.1286	fay+qtz+mt, Fe powder	650	48	cpx, pl, gl*, timt, gl	none
MAm-E-12	1	2	time-series	Mam-51	Ag capsule	0.1038	fay+qtz+mt, Fe powder	650	111	cpx, pl, gl*, timt, gl	none
MAm-E-13	1	2	time-series	Mam-51	Ag capsule	0.1136	fay+qtz+mt, Fe powder	650	158	cpx, pl, gl*, timt, gl? (tr.)	none
MAm-E-14	1	2	high-temperature	Mam-51	Ag capsule	0.1042	fay+qtz+mt, Fe powder	790	88	cpx, pl, gl*, timt, mt, ol (tr.)	1
MAm-E-15	1	2	high-temperature	Mam-51	Ag capsule	0.1017	fay+qtz+mt, Fe powder	750	88	cpx, pl, gl*, timt, ol (tr.)	none

See next page for notes.

Table 2.2 (Continued). Sample experimental parameters and petrologic data

Sample[a]	Reagent batch#	Expt group#	Kind	Starting material	Sample container	Recovered sample mass [g]	Buffer/Monitor[b]	T_f[c] [°C]	Duration [day]	Phases[d]	Exsolution types[e]
Terrestrial-type:											
MB2-30 (fused bead)	1	1	fused bead	n.a.	Pt wire	~0.005	none	1280	1 h	gl	n.a.
MB2-50 (fused bead)	2	2	fused bead	n.a.	Pt wire	0.0054	none (pre-checked with sensor)	1340	2 h	gl	n.a.
MB2-31 (starting material)	1	1	crystalline starting material	n.a.	Pt capsule	0.2770	fay+qtz+mt	1070	100 h	pl, cpx, gl, hem, femgal	n.a.
MB2-48 (starting material)	2	2	crystalline starting material	n.a.	Pt crucible	3.3142	sensor	1070	100 h	pl, cpx, gl, timt, ilm	n.a.
MB2-E-03	1	1	group 1 representative	MB2-31	Ag capsule	n.d.	fayalite	710	54	pl, cpx, gl, femgal, femg, mgf (tr.), timt? (tr.), mt? (tr.), ol? (tr.)	2, 3, 1?
MB2-E-09	2	2	time-series	MB2-48	Ag capsule	0.1769	fay+qtz+mt, Fe powder	650	21	pl, cpx, gl, timt, ilm, ol	none
MB2-E-10	2	2	time-series	MB2-48	Ag capsule	0.1785	fay+qtz+mt, Fe powder	650	32	pl, cpx, gl, timt, ilm, ol	none
MB2-E-11	2	2	time-series	MB2-48	Ag capsule	0.1108	fay+qtz+mt, Fe powder	650	48	pl, cpx, gl, timt, ilm, ol, chr (tr.)	none
MB2-E-12	2	2	time-series	MB2-48	Ag capsule	0.1037	fay+qtz+mt, Fe powder	650	111	pl, cpx, gl, timt, ilm, ol	none
MB2-E-13	2	2	time-series	MB2-48	Ag capsule	0.1068	fay+qtz+mt, Fe powder	650	158	pl, cpx, gl, timt, ilm, ol	none
MB2-E-14	2	2	high-temperature	MB2-48	Ag capsule	0.1095	fay+qtz+mt, Fe powder	790	88	pl, cpx, [gl*], timt (tr.), ilm (tr.), ol	none
MB2-E-15	2	2	high-temperature	MB2-48	Ag capsule	0.1039	fay+qtz+mt, Fe powder	750	88	pl, cpx, [gl*], timt, ilm, ol	none

[a] Starting materials MAm-36 (Group 1 by Bowles) and MAm-51 (Group 2) are both from the same reagent mixture, whose composition was measured in MAm-34. Starting materials for MB2-31 (Group 1 by Bowles) and MB2-48 (Group 2) are from different reagent mixtures, whose compositions were measured in MB2-30 and MB2-50, respectively.

[b] Phase abbreviations: fay=fayalite, qtz=quartz, mt=magnetite.

[c] Starting materials were first brought to T_i, 1225 °C for M-type (MAm-series) and 1290 °C for T-type (MB2-series), then cooled to T_f and held for the listed duration, then quenched.

[d] Phases are listed in order of approximate decreasing volumetric abundance. Phase abbreviations: cpx=clinopyroxene, gl=glass, hem=hematite, femgal=Fe-Mg-Al spinel oxide, pl=plagioclase, timt=titanomagnetite, mt=magnetite, femg=Fe-Mg spinel oxide, gl*=devitrified glass, ol=olivine, mgf=magnesioferrite, ilm=ilmenite, (tr.)=trace phase, [ ]=groundmass or very fine grained crystals.

[e] Exsolution types are listed in approximate decreasing volumetric abundance. Exsolution types: (1) magnetite - Al-bearing titanomagnetite, (2) Fe-Mg-Al spinel oxide - Fe-Mg spinel oxide, (3) Fe-Mg-Al spinel oxide - Al-bearing magnesioferrite.

For the Group 2 T-type material, the bead did not fall into the water upon quench and remained attached to the zap wire. Thus, the sample holder was pulled to near the top of the furnace chamber to cool sufficiently fast while the gas was flowing. The retrieved glass beads were naturally dried and a grain mount or thin section was made for the each bead using epoxy for electron probe microanalysis (EPMA).

2.1.1.3 Conditioning of the Reagent Mixture

The mixtures of the reagents were conditioned at 925 ºC and fO_2 at QFM controlled by flowing H_2-CO_2 for ~4 h to decarbonate reagents and reduce ferric/ferrous ratio.

First, the Deltech furnace was heated to the experimental temperature (925 ºC) and H_2-CO_2 gas was inserted to attain QFM condition measured by a fO_2 sensor (Appendices C and D). Approximately 3.5 g and 4.0 g for M- and T-type reagent mixtures were placed in a boat-shaped ceramic container (VWR Combustion Boat 7 mL, VWR International) and were inserted at the center of the alumina tube. Upon conditioning, both ends of the alumina tube were sealed with rubber plugs to which short cupper tubes were inserted to lead one side to the H_2-CO_2 gas input from the Deltech furnace and another to the output bubbler (see Appendix D). The bubbler side of the alumina tube was filled with Alumina-Silica Bulk Fiber (Zircar Ceramics) to delay gas escape to the output and to enhance gas mixing within the tube. The gas valve from the Deltech furnace was opened and the alumina tube was placed in the Mini-Mite Tube Furnace (Lindberg/Blue M) at 925 ºC at the center of the furnace where the K-type thermocouple was located. This horizontal tube furnace was located inside a fume hood in case of gas leakage. The furnace setting is illustrated in Appendix E. The temperature

displayed by the horizontal tube furnace was monitored and the time at which the temperature recovered to the target value was considered to be the starting time of the conditioning. A subsequent overshooting of the temperature usually observed for this type of furnaces was neglected for the determination of the starting time because of a short duration (a few minutes) of the overshooting. The sample was held for ~4 h at this temperature. At the end of the conditioning, the alumina tube was taken out from the furnace while gases were flowing, and air-cooled. Subsequently, the gas supply was terminated.

For the Group 1 experiment conducted by Bowles, the Deltech furnace was used instead of the horizontal tube furnace for this procedure. Also, an alumina crucible with a lid was employed for the sample container. Because the sample must have been manually inserted or withdrawn from the top of the open furnace chamber, the sample insertion was conducted without flowing gas and at very slow rate to avoid damage on the chamber due to a thermal stress. The air-cooling of the sample was conducted by keeping the sample near the top of the furnace at cooler temperatures while gases were being turned on or off.

2.1.1.4 Production of Crystalline Starting Materials

A Pt crucible (~2-cm-tall, bucket-shaped) was selected for the sample container for this procedure, firstly because Pt had a melting point above the maximum experimental temperature (1290 ºC) and reacted minimally with starting materials under the experimental conditions. Secondly, it could accommodate large amount of sample (>3 g for both compositions) compared to capsules made of Pt tubing (O.D. = 5 mm, length = = ~3 cm) that was employed by Bowles for Group 1 which accommodated only ~0.5 g of

sample. As a matter of fact, the crucible allowed us to produce enough starting materials for the whole series of exsolution experiments (7 runs in total for each composition with each run containing >0.1 g of starting material), while it can induce sample heterogeneity due to large sample size (see section 3.1.1).

Although Pt has low reactivity with samples in contact, it is known that Fe in samples tends to migrate into Pt where the amount of Fe at saturation in Pt is a function of temperature and fO_2 (Hammer, 2006) as mentioned in the previous section (see section 2.1.1.2). Therefore, the crucible was conditioned by saturating Pt with Fe at experimental condition before the crystalline starting material production step, which will be described here first. This procedure was also conducted for Pt capsules in experiments for Group 1 by Bowles. This process also lowered a recyclability of their Pt capsules for experimental runs compared to the crucible because of accumulating damages on the capsules upon sample recovery. Sample recovery from the Pt capsules and crucible was conducted by pressurizing the containers over the samples inside using a pair of pliers for the capsules and a vise for the crucible to break samples into pieces. The Pt malleability apparently decreased after conditioning of Pt and the capsule wall sometimes tore after a few experimental runs although crucible was not damaged.

The conditioning of the Pt crucible was conducted by annealing the Pt crucible containing a material with a similar Fe concentration and bulk composition as the starting materials at temperature $>T_L$ and QFM for 6 h in the Deltech furnace with flowing H_2-CO_2. Only one Pt crucible was employed to synthesize both M-and T-type starting materials. Because T-type starting material had lower Fe content, the conditioning of Pt crucible was first conducted for T-type composition, followed by a synthesis of the T-

type starting material. The crucible was then conditioned for M-type composition, followed by a production of M-type starting material. The conditioning was repeated twice for the initial one to make certain that the crucible was saturated with Fe under the first experimental condition. Natural basalt lava erupted and quenched at the ocean in 2008 in the Island of Hawai‘i (HI), collected and provided by JE Hammer in 2008 was used for the initial conditioning of the Pt crucible. The Fe_2O_3 content of this basalt was assumed to be 12.5 wt.%, the reported average Hawaiian basalt erupted recently (Garcia et al., 2000). Therefore, it is not too far from the T-type starting material in both FeO(t) concentration and bulk composition (Table 2.1). This basalt was powdered (<0.124 mm) using a mortar and pestle, and approximately 6.0 and 6.5 g were used for the T-type conditionings of the Pt crucible. The conditioning for the M-type composition was conducted using the same powdered natural basalt (~5.9 g) with additional FeO by adding Fe_3O_4 oxide powder (~0.6 g) in order to replicate FeO(t) content of M-type composition (~19 wt.%). Two holes were made on the upper facing walls of the Pt crucible to accommodate a handle made of Pt wire. This allowed the crucible to be hung from the sample holder by its handle (Appendices C and D). The crucible was then deformed manually to have an elliptical opening at its top in order to fit in the Deltech furnace chamber without a contact with an inner chamber wall. Basalt or modified basalt powder was manually packed into the Pt crucible that reaches ~6 mm from the top of the crucible. A general annealing procedure using Deltech furnace is described in Appendices C and D. The furnace was set to reach the target temperatures for the actual samples 1290 ºC and 1225 ºC (furnace set point 1340 ºC and 1267 ºC) for the T-type (the first two conditionings) and M-type (the last conditioning before the actual M-type

starting material) compositions, respectively. After duration of 6 h at the target temperature and QFM, the sample was quenched while the gas was flowing. The basalt used for this Pt crucible conditioning procedure were retrieved from the crucible in a manner described earlier, kept aside, and new basalt powder was used for each conditioning. Before the crucible was used for synthesis of the starting materials, it was soaked in fluoroboric acid (50%) for 4-5 days to remove silicate residue from the conditioning. The crucible was rinsed with distilled water in an ultrasonic bath a few times after an exposure to the acid.

The procedure for the synthesis of the Group 2 starting material (MAm-51 for M-type and MB2-48 for T-type) was similar to that of the conditioning of the Pt crucible, except for the temperature treatment (Table 2.2). The temperature was programmed to first reach the target value for each composition, 1290 ºC for T-type and 1225 ºC for M-type, dwell for 6 h, and cool to 1070 ºC at the rate of 4 ºC h^{-1}. The sample was drop-quenched after being held for 100 h at the final temperature to attain crystalline starting materials that were analogous to slowly intruded materials with analyzable crystal size. These were all at QFM using flowing H_2-CO_2. The sample recovery and cleaning of the Pt crucible are also as described above.

The crystalline material synthesis method used by Bowles for Group 1 (MAm-36 for M-type and MB2-31 for T-type) is as appears in Bowles et al. (2008). The temperature and duration settings were the same as Group 2. The differences from Group 2 is that it was conducted using Deltech furnace as well, but the evacuated silica capsule with solid state buffer was used to maintain fO_2 at QFM instead of flowing H_2-CO_2.

2.1.2 Exsolution Experiments

2.1.2.1 Sample Preparation

The split of the starting material was sealed in an Ag capsule along with a solid state QFM buffer placed in a Pt capsule to monitor fO_2 (Figure 2.1). The Ag capsule was sealed in an evacuated silica capsule along with Fe^0 reagent powder placed in an Ag capsule as an oxygen getter to avoid departure from QFM toward higher fO_2.

More than ~0.1 g (>7-8 pieces) of splits of the starting material was selected and placed in an Ag capsule (O.D. = 5 mm) whose bottom had been welded-closed. Welding of Ag capsule as well as any welding involved in the course of procedure in this study was conducted using an oxy-acetylene torch (Smith Equipment) where the both gases were 5 psi. The selection of the splits from the starting materials was made so that there were enough numbers of splits for the exsolution runs for a thin section and magnetic analyses, and ideally some left-over as a back-up. Also, the grains that seemed to have been in contact with the Pt crucible upon production of the starting material and the other part were included in each exsolution run to avoid a possible bias of the starting material selection. The two types of grains were distinguished by an obvious smooth surface of the former type. A solid state QFM buffer was prepared to be sealed in the Ag capsule along with the sample. The buffer consisted of fayalite (Fe_2SiO_4) (~0.08 g), silica (SiO_2) (~0.008 g), and magnetite (Fe_3O_4) (~0.008 g) reagents. Fayalite was natural mineral and coarse-grained (0.06-0.19 in, Alfa Aesar) unlike other reagent powders, therefore, they were powdered in a similar way as natural basalt (see section 2.1.1.4) in order to maximize its surface area and an efficiency of the buffer assemblage. The buffer works

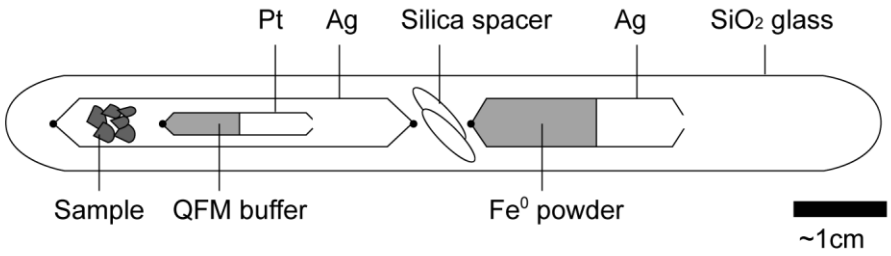

Figure 2.1. A schematic diagram of the exsolution experiment sample assemblage. The sample is sealed in an Ag capsule along with QFM buffer in a Pt capsule. This capsule is enclosed in an evacuated silica capsule together with iron powder in a crimped Ag capsule that works as an extra oxygen getter. For precise size of the parts, see section 2.1.2.1.

by the following chemical reaction:

$$3Fe_2SiO_4 + O_2 = 3SiO_2 + 2Fe_3O_4 \qquad \text{Eq. (2.1)}$$

As oxidation takes place, the reaction proceeds forward, and the compounds on the right hand side of the equation start to dominate in the buffer assemblage. The weight proportion of fayalite was made an order of magnitude larger compared to the other compounds to avoid oxidation in the system based on the susceptibility of long-duration-experiments to oxidation reported from the previous experiments. Weighed buffer constituents were combined and it was placed in a Pt capsule (O.D. = 4 mm) whose bottom was closed by welding. The capsule was tapped to compact the buffer, and the top was loosely crimped. The Pt capsules were recycled for the following experimental runs after removal of the buffers from the previous runs. The removed buffers were kept aside to make a grain mount to be observed under transmitted light photomicroscope. A departure from QFM buffer curve could be recognized by disappearance or dominance of buffer constituent(s) of only one side of Eq. (2.1). The Pt buffer capsule was placed in the Ag capsule on the top of the starting material, and the top of Ag capsule was welded to shut. Upon welding to seal the Ag capsule, ~2/3 of the capsule from its bottom was wrapped with a wet paper towel to avoid alteration of the sample and the buffer due to heating. In addition to QFM solid state buffer, Fe^0 reagent powder (~0.5 g) was employed as an oxygen getter to make certain to avoid oxidation of the sample. The Fe^0 powder was placed in an Ag capsule (O.D. = 5 mm) whose bottom was welded-closed. It was tapped to compact the powder and the top of the capsule was crimped to close. Unlike the Pt capsules used for a QFM buffer, the Ag capsule for Fe^0 was not recycled mainly due to its low cost. The sealed Ag capsule containing the starting material and buffer was gently

slid into a silica tube ({I.D., O.D.} = {7 mm, 9 mm} or {I.D., O.D.} = {6 mm, 11 mm}) whose bottom end had been welded-shut. Then, a few pieces of broken silica tube were inserted as a spacer between the sample Ag capsule and the Ag capsule containing Fe^0 that was inserted next. The part of the silica tube where the sample and the oxygen getter were located was wrapped with a wet paper towel upon welding of the silica tube to narrow the channel of the tube that would become another end of the silica capsule. A part of the silica tube ~1cm in length was heated by a torch flame by moving and rotating the silica tube over the torch fixed in position with a holder. A care was taken try not to tilt the tube too much and spill Fe^0 powder. Once the silica tube started to glow in orange, it was gently stretched while still being heated and rotated to make a narrow channel (<2-3 mm), and removed from the flame before the channel closed. A silica tubing with a thicker wall was employed for the longest duration run for a further protection form anticipated oxidation by an invasion of oxygen into the silica capsule from the surrounding. However, it was not efficient in welding probably because the torch was not powerful enough to keep the entire circumference of the larger-outer-diameter-tubing to be hot enough. Also, the welded ends could have been as thin as those of the tubing with a thinner wall because welding of the thicker-walled tubing was forced by an extreme stretching of the tube. Therefore, the effect of this alternative was uncertain. When the temperature of the welded part was cooled enough to be handled safely, the open end of the silica tube was connected to an evacuator (model 5KC36LN26J, GE Motors and Industrial Systems). Between the evacuator and the silica tube, a glassware that worked as a vapor getter was placed in the line. The glassware was placed in a container ~1/3 filled with liquid N_2. A manometer (model TCG531, Duniway Stockroom) was coupled

with the evacuator for pressure readings. Complete sealing of the connections by rubber hoses was ensured using grease. The evacuation of the silica tube was conducted for >20 min to achieve pressure lower than 30 mtorr. Once the target pressure was reached, the narrowed portion of the silica tube was welded to close with the torch fixed in position while it is still under evacuation. The silica capsule was rested to cool down in a beaker to keep its vertical position. The evacuator was turned off and the other part of the silica tube remained attached to the evacuating system was removed after it cooled enough and the pressure recovered near 1 atm. This silica tube was used for another exsolution run. Absence of holes at the welded tip of the silica capsule was usually confirmed visually. If incomplete sealing was still suspected, the capsule was submerged into water for a further confirmation.

2.1.2.2 Experimental Setting and Procedure

The Group 1 representative was run at 710 ºC for 54 days (samples MAm/MB2 -E-03) (Table 2.2 and Figure 2.2). The Group 2 experiments consist of time-series (samples MAm/MB2 -E-09 – E-13) and high-temperature series (samples MAm/MB2 -E-14 – E-15) (Table 2.2 and Figure 2.2). The temperature for the time-series, 650 ºC, was selected so that it was high enough for the kinetics and yet low enough to be subsolvus for non-pure titanomagnetite system based on the Group 1 experiment that yielded optically observable exsolution. The durations for the time-series runs were 21, 32, 48, 111, and 158 days. The duration in order of days was selected assuming the kinetics to be relatively slow. The time intervals between the runs were made so that they are natural-log-linear, assuming that the reaction rate generally slows down with prolonged duration passing a reaction peak. The high-temperature experiments run at 750 and 790 ºC for 88

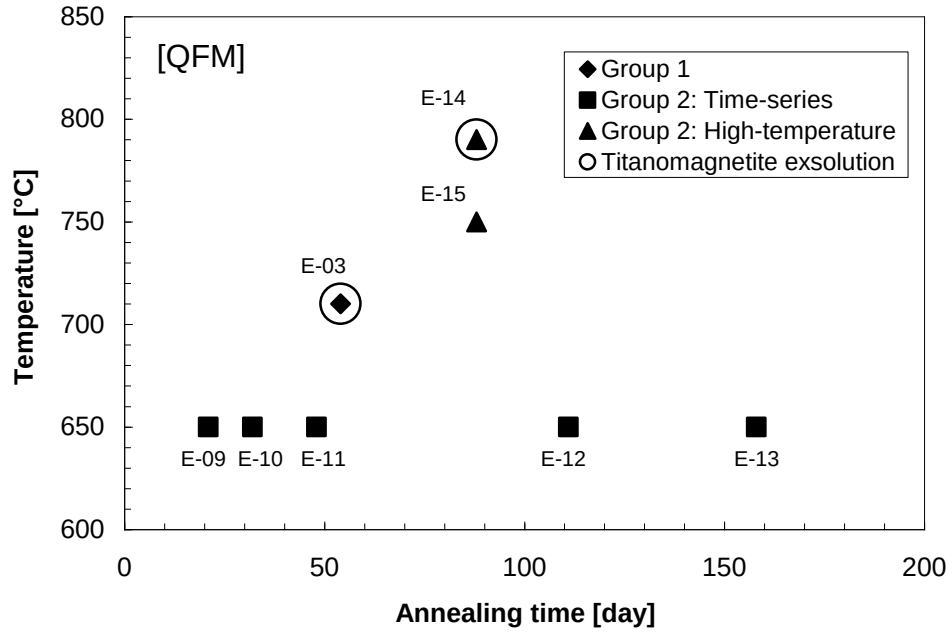

Figure 2.2. A temperature vs. time plot of the experimental conditions. All experiments are at quartz-fayalite-magnetite (QFM) buffer curve using each of two different bulk compositions, M- and T-types.

days were originally intended to be part of planned temperature-series experiments in relation to Group 1. Thus, the temperature and duration of the high-temperature series seems to be inconsistent with the time-series of Group 2. It is introduced in this thesis because of their common starting material and an attainment of titanomagnetite in one of the samples.

The isothermal annealing experiments were conducted using horizontal tube furnace (Figure 2.3). The samples for each composition were paired and placed in an alumina tube, where the samples were located ~1 cm inward from the edge of the tube. The tube containing the samples was placed near the center in a tube furnace that had been heated beforehand to the target temperature. Five of the horizontal furnaces were used in the series of experiments. For each furnace, a furnace temperature set point that corresponds to the target sample temperature at the sample position (center of the furnace, or hot spot) was determined. It was conducted by trial and error, adjusting the furnace temperature set point to obtain the right temperatures at the sample position measured by an external K-type thermocouple. An alumina tube with a pair of dummy silica capsules were placed at the sample position and the K-type thermocouple was inserted to read the temperature at the center of the furnace.

The alumina tube containing samples was taken out of the furnace and air-cooled. The silica capsules were taken out of the alumina tube immediately after to hasten the air-cooling. Once the capsules were cool enough, they were broken to retrieve the samples. All materials in the silica capsule were kept. The QFM buffer was examined for sample oxidation status as described in section 2.1.2.1. The Fe^0 powder was also checked if there is no significant difference before and after annealing. Usually a few pieces of the sample

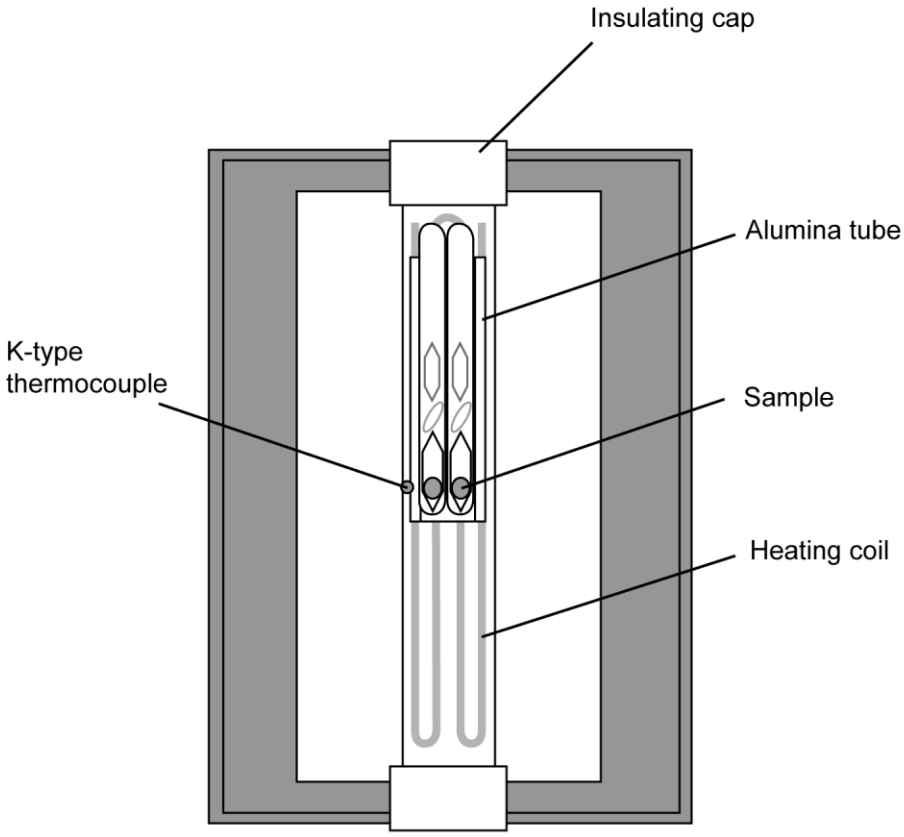

Figure 2.3. A schematic diagram of the exsolution experiment. The diagram is showing a top view of the tube furnace when the lid is opened. Samples for the same anneal duration from M- and T-type compositions were paired and placed in the center of the furnace inside an alumina tube (cut away view here), at the furnace hot spot.

were selected for compositional analyses, and thin section was made.

2.2 Analytical Methods

The analytical techniques introduced here are standard methods. Therefore, the descriptions are brief. In addition to the following techniques, Raman spectroscopy was employed to infer structure of the oxide phases. The method is identical to that in Part II. Additional techniques employed whose data were determined not to be essential are listed in Appendix F.

2.2.1 Electron Probe Microanalysis

The electron probe microanalysis (EPMA) was performed on thin section or grain mount of fused glass beads of reagent mixtures for Groups 1 and 2, and thin sections of the crystalline starting material samples of Groups 1 and 2 using JEOL JXA-8500F Field Emission Hyperprobe at the University of Hawai‘i at Mānoa. For the crystalline starting materials and the annealed samples, only oxide crystals were the target of the spot analysis. An accelerating voltage was 15 keV for all the samples. Electron beam current and diameter were 10 nA and 10 μm respectively for the glass analyses, and 8-25 nA and near zero-1 μm for the oxide crystals. The lower values for the beam current and diameter were used for small grains or finely exsolved phase attempting to minimize data contamination from the surroundings. Other detailed measurement information is listed in Appendix G. Na was measured first to minimize its loss before measurement. A possible loss of Na and K was corrected by time-dependant intensity corrections incorporated in ProbeForWindows software (Donovan, et al., 2007). Compositions were obtained from raw counts using a ZAF intensity correction.

The glass bead for the Group 1 M-type composition was found to contain Fe-Ti oxide crystals that were decided to be negligible since they were ~0.6 % of the whole area of the sample in BSE image, as determined using software ImageJ. The bead for the Group 2 T-type composition did not fall into the water upon quench as mentioned above (see section 2.1.1.2). However, its compositional homogeneity and absence of crystals were confirmed by EPMA. For fused beads, 10 measurements were obtained for each sample. Similarly, obtainment of (1) at least 10 spot analyses on different grains and (2) possibly multiple analyses within grains were attempted, for oxide phases. For some samples, the attempt (1) was not achieved due to a scarcity of the measureable grains (e.g., Group 2 T-type high-temperature run at 790 ºC (MB2-E-14)). Attempt (2) was achieved for exsolved oxide phases. It was also achieved for some samples of Group 2 time-series runs with shorter duration. However, it was not carried out for the longer duration runs since no intra-grain compositional heterogeneity was observed for the shorter-duration samples. SiO_2 content was measured for the oxide grains to evaluate the quality of the spot analyses. The data with $SiO_2 > 0.5$ wt.% were considered to be contaminated by the surrounding silicates or glass and they were not included for data interpretations.

2.2.2 Bulk Magnetic Measurements

The data for the Group 1 samples were collected by JA Bowles and the Group 2 high-temperature samples were collected by LT Petrochilos at the Institute for Rock Magnetism, University of Minnesota. The Group 2 starting materials and the time-series samples were collected by DM Cuomo at the Montclair State University.

A split or multiple splits of >20 mg (a few pieces) of the sample were allocated for the bulk magnetic measurements. The measurements by Bowles or Petrochilos were conducted on the whole spilt. Those by Cuomo were performed on individual chips to obtain the average.

Magnetic hysteresis curves, coercivity of remanence (H_{cr}) and saturation magnetization (M_s) versus temperature curves (M_s-T) were measured on a Princeton Measurement Corporation Vibrating Sample Magnetometer (VSM) for all samples. The hysteresis curves were measured at room temperature with a peak field of 1 T and increment of 2 mT for the Group 1 and Group 2 high-temperature samples, and 5 mT for the Group 2 time-series samples. The hysteresis parameters (M_s, saturation remanent magnetization (M_{rs}), coercivity (H_c)) were obtained using a linear paramagnetic correction derived from the high field slope. The H_{cr} was measured by demagnetizing the imparted 1-T isothermal remanence with a back field until the remanence vanishes. The increment of the back field was 0.5 mT for Group 1 starting materials, 1 mT for Group 1 annealed runs, 10 mT for the Group 2 starting materials and the time-series samples, and 2 mT for the Group 2 high-temperature runs. The M_s-T curves were measured from 30-600 ºC at 1 T for Group 1, 30-700 ºC at 50 mT for Group 2 starting materials and the time-series samples, and 30-700 ºC at 1 T for the Group 2 high-temperature runs. Curie temperatures (T_C) for Group 1 and Group 2 high-temperature runs were determined by the intersecting-two-tangents method (Grommé et al., 1969).

3. RESULTS

The key aspects of the results can be classified into 2 categories that pertain to: (1) the experimental variables (bulk composition (M-type vs. T-type), annealing time, and annealing temperature) and (2) non-pure titanomagnetite exsolution, respectively. For the first category, the different modal abundance of minerals in crystalline starting materials corresponding to a difference in bulk compositions was confirmed in both Groups 1 and 2. It was as expected from the previous studies (Hammer, 2006; Brachfeld and Hammer, 2006; Bowles et al., 2009). In addition, difference in oxide phase assemblages between Groups 1 and 2 crystalline starting materials were observed. None of the experimental variables listed above seem to be responsible for this. The reasons are examined in Discussion section (see section 4.1). A progressive oxide composition change with time and temperature was present in Group 2 samples. For the second category, non-pure titanomagnetite exsolution was present in Group 1 M-type annealed sample and Group 2 M-type high-temperature run at 790 °C. The detailed experimental results are described in the sections below.

3.1 Petrologic Characterization

3.1.1 Starting Material Bulk Compositions

The bulk compositions of M-type starting material for Groups 1 and 2 (MAm-34), and Group 1 T-type material (MB2-30) were nearly the same as their target compositions (Table 2.1). That for Group 2 T-type material was distinct from the target value or Group 1 sample. For the T-type starting materials, Group 2 has lower SiO_2 (-9.23 wt.%) and higher Al_2O_3 (+4.24 wt.%) and CaO (+3.00 wt.%), with respect to Group 1. It has olivine

and feldspathoid as normative minerals (18.6 and 2.68 wt.%, respectively), but lacking quartz, where the opposite is true for Group 1.

The rest of petrologic descriptions in this section are focused on oxides. Identities of the oxide phases were determined based on their compositions from EPMA (Appendices H-J) as well as structure inferred from Raman spectra (Appendix K). From EPMA data, Fe (atoms per unit formula) was calculated into Fe^{2+} and Fe^{3+} with 3 and 4 oxygen bases (3=rhombohedral, 4=spinel) using a method of Droop (1987), and corrected oxide totals were obtained. The oxygen basis that yielded a more reasonable corrected oxide total (usually closer to 100 wt.%) was decided to be the right one. Raman spectra have distinct peaks dependant on structure of the materials. Spinel oxide is known to have 5 distinct peaks at maximum depending on its composition, where the major peak is at ~670 cm^{-1} (see Part II of this thesis). Hematite has ~7-9 major peaks, where the prominent peaks are at ~230, 300 and 1300 cm^{-1} (de Faria et al., 1997; Wang et al., 2004). Ilmenite has 4 distinct peaks where the prominent ones are at ~230 and 690 cm^{-1} (Wang et al., 2004). The approximate spectral peaks were compared to known spectral peaks of the magnetite (titanomagnetite) and hematite to determine the structures of measured oxide grains. Determination of oxide phase structure form EPMA and Raman agreed well. The validity of the compositional data with relatively low corrected totals is supported by the fact that the standard magnetite used for EPMA calibration (Magnetite, Minas Gerais, USNM 114887) has a low corrected oxide total (98.1 wt.% as a published value. But EPMA data on the same standard as a bench standard were always below 98 wt.%). Systematically high corrected totals (up to ~103 wt.%) obtained from the exsolved oxide phases might be due to stoichiometry close to ideal (i.e., no vacancy or excess oxygen in

the structure) because of cation ordering under low temperature annealing and/or secondary fluorescence of cations from surroundings. The labeled numbers for some data points in these diagrams correspond to those in the BSE images introduced in textural descriptions. Magnetite (Mt; Fe_3O_4), ulvöspinel (Usp; Fe_2TiO_4), magnesioferrite (Mgf; $MgFe_2O_4$), hercynite (Hc; $FeAl_2O_4$), and chromite (Chr; $FeCr_2O_4$) were selected as end-member minerals of spinel-structured oxide phases for all the experiments. They were the most appropriate end-members based on the abundance and partitioning of elements in the exsolved oxide crystals in all the experiments. For the rhombohedral oxide phases, hematite (Hem; Fe_2O_3), ilmenite (Ilm; $FeTiO_3$), and Geikielite (Gk; $MgTiO_3$) were chosen based on elemental abundance in those phases. The characteristic values of oxide compositions in terms of these end-members reported in the text below are median values for each sample rather than the average. The median was chosen because of the observed textural and compositional heterogeneity in time-series samples attributed to the starting material (Appendix L). The maximum differences in major oxides concentrations among rock chips in the case in Appendix L are 8.66 wt.% and 6.16 wt.% for TiO_2 and FeO(t), respectively. If any of the end-members are minor (<5%), they are combined to be denoted as component "Z" similarly to the notations appear in Bowles et al. (2009). The compositions of the two end-members in the exsolved samples are taken to be those the furthest apart as obtained by EPMA.

3.1.2 Experimental Group 1: Pilot Experiments

3.1.2.1 Meteorite-Type

The phase assemblage in the starting material of the crystalline starting material

(MAm-36) is clinopyroxene, glass, hematite ($Hem_{87}Ilm_3Gk_{10}$), Fe-Mg-Al spinel oxide ($Mt_{16}Mgf_{68}Hc_{10}Z_6$), and plagioclase, in the approximate order of decreasing volumetric abundance (Table 2.2). Clinopyroxene crystals in this sample are euhedral feathery dendrites with a slight but complex zoning. Plagioclase is a trace phase in this sample, which occurs as euhedral and equant, fine decorative crystals on clinopyroxene (Figures 3.1a and b). The hematite grains are either equant or hopper, and euhedral with ~1-30 μm in diameter. The hopper grains commonly have melt inclusions. They appear in back-scattered electron (BSE) images as lighter-toned opaque phase (Figures 3.1a - c). The Fe-Mg-Al spinel oxide grains are commonly equant, euhedral, and ~1-30 μm in diameter, but some grains have a hopper texture with little melt inclusions. In contrast to hematite grains, they are darker-toned in BSE images, reflecting their compositional difference (Figures 3.1a - c). In BSE images, element with higher atomic number appear with a lighter tone. Some oxide grains have both phases within the grains with a sharp phase boundary based on this tone difference. In such grains, the tone contrast between the two phases is accentuated (Figures 3.1a and c).

The annealed run from this starting material (MAm-E-03) has the same phase assemblage as its starting material (MAm-36), except for the onset of the exsolution in oxide phases and devitrification (Table 2.2). The textural changes are also associated with these new phases. The devitrified parts of glass appear in the BSE image as clusters of possibly equant very fine-grained (submicron) crystals (Figures 3.2a and e). Its identity is uncertain since the crystals were too small to be quantitatively analyzed. The exsolution of the oxide phases recognized visually in the BSE images took place for many grains but not all. There are two texturally distinct exsolved oxide phases in the sample. One has

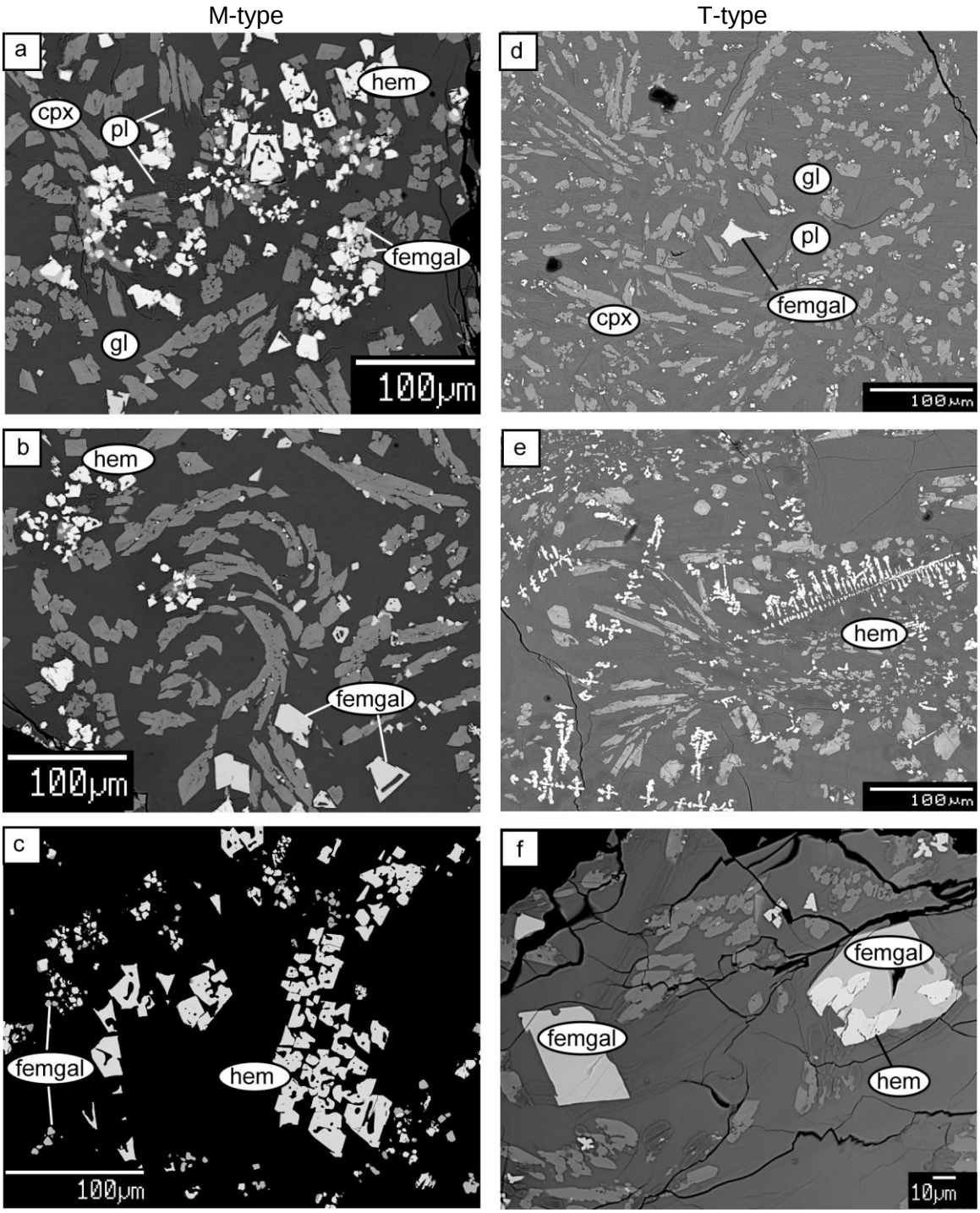

Figure 3.1. Back-scattered electron images of the Group 1 starting materials (MAm-36, MB2-31). (a-c): M-type (MAm-36). (d-f): T-type (MB2-31). The images in (d) and (e) were obtained by JA Bowles at University of Hawai‘i at Mānoa, using JEOL J5900 scanning electron microscope. The rest is from electron microprobe (see section 2.2.1). See text for detailed textural descriptions. Abbreviations: cpx=clinopyroxene, pl=plagioclase, gl=glass, hem=hematite (lighter tone), femgal=Fe-Mg-Al spinel oxide (darker tone).

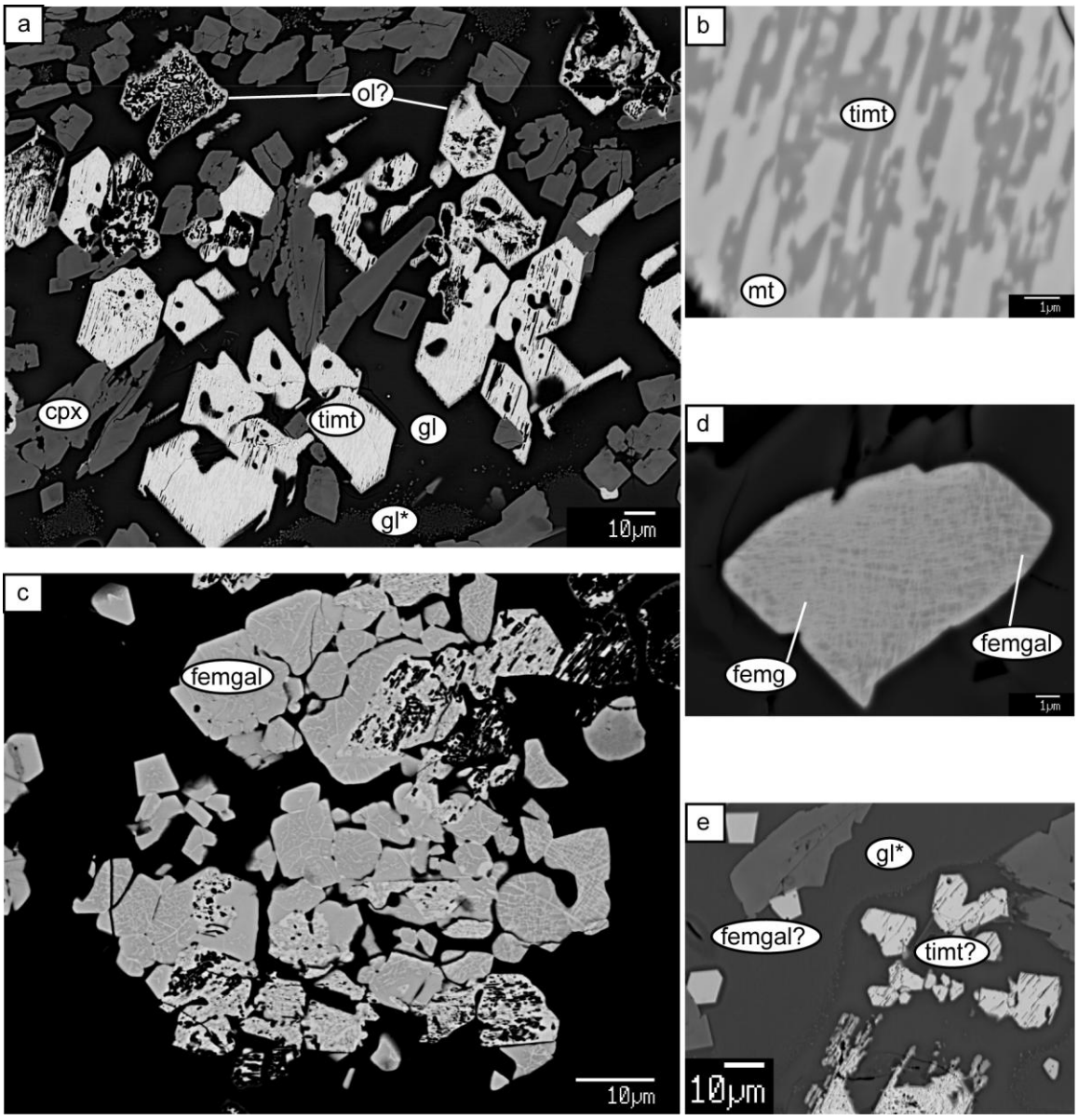

Figure 3.2. Back-scattered electron images of the Group 1 M-type annealed sample at 710 °C for 54 days (MAm-E-03). (a-b): Type (1) exsolution, magnetite (light) – Al-bearing titanomagnetite (dark). Some grains are highly porous and some have olivine (?) reaction rim. (c-d): Type (2) exsolution, Fe-Mg spinel oxide (light) – Fe-Mg-Al spinel oxide (dark). (e): Non-exsolved oxide phases. See text for detailed textural descriptions. Abbreviations: cpx=clinopyroxene, gl=glass, gl*=devitrified glass, timt=titanomagnetite, ol=olivine, mt=magnetite, femgal=Fe-Mg-Al spinel oxide, femg=Fe-Mg spinel oxide.

magnetite ($Mt_{90}Mgf_7Z_3$) and Al-bearing titanomagnetite ($Mt_{60}Usp_{29}Hc_6Z_5$) as end-members (Figures 3.2a and b). Another is exsolved Fe-Mg-Al spinel oxide (Figures 3.2c and d). The intergrowth of lamellae for this type of exsolution was too fine in this sample, therefore, only mixed microprobe analysis was possible. The obtained composition is $Mt_{37}Usp_2Mgf_{42}Hc_{12}Chr_7$. The non-exsolved grains are Fe-Mg-Al spinel oxide ($Mt_{34}Mgf_{49}Hc_{13}Z_4$) (Figure 3.2e). Let us call the two distinct exsolutions Types (1) and (2), respectively. The oxide crystals underwent Type (1) exsolution consist of dark-toned lamellae of Al-bearing titanomagnetite and light-toned magnetite host in BSE images (Figures 3.2a and b). The thickness of Al-bearing titanomagnetite lamellae is ~0.5 μm and that of magnetite host is usually ~ 0.2-1 μm. An intra-grain distribution of the lamellae and host is nearly homogeneous. However, there are occasionally large blobs (~5 μm diameter) of magnetite host within grains. The exsolved grains usually have pores along the exsolution texture. In addition, some grains have reaction rim in contact with glass. Although this rim is too thin to be analyzed, it was assumed to be fayalitic olivine that also occurs in high temperature M-type run at 790 °C in Group 2 (MAm-E-14) as a reaction rim on titanomagnetite (see section 3.1.3.2.1). For Type (2) exsolution, the exsolved grains consist of light-toned, threaddy lamellae of Fe-Mg spinel oxide and dark-toned Fe-Mg-Al spinel oxide host (Figures 3.2c and d). The identities of the exsolved phases for this type were adapted from texturally and compositionally similar exsolved oxide phase in the T-type sample in the Group 1 experiment assuming they are an identical solid solution exsolution (see section 3.1.2.2). It was because the Type (2) exsolution in this sample was too fine-textured to perform quantitative analyses on each exsolution end-member. Unlike Type (1), light-toned lamellae is typically thin (<0.2-μm-

thick) although it can densely populate within a grain as in Figure 3.2d. Also, regardless of an apparent preferred right-angle-mutual-intergrowth of the lamella, their orientation can vary within a grain in a curvy manner. An intra-grain distribution of the lamellae and host is heterogeneous, unlike in Type (1).

The compositional characteristics of the oxide phases suggest that hematite in starting material is parental to Type (1) exsolution in the annealed run product (Figures 3.3 and 3.4a - c). Similarly, Fe-Mg-Al spinel oxide in starting material is most likely parental to Type (2) exsolution. In Type (1) exsolution, Ti and Al partition into titanomagnetite phase whereas Fe partitions into magnetite phase (Figures 3.4a - b and 3.5). There seems to be a slight co-variation of Fe and Mg although Mg is a trace element in this system (Figure 3.5). For Type (2) exsolution, see section 3.1.2.2 in which compositional data are available. A minor number of oxide grains in annealed run product that do not texturally exhibit exsolution are compositionally similar to the Fe-Mg-Al spinel oxide phase from its starting material (Figures 3.3 and 3.4a - c).

3.1.2.2 Terrestrial-Type

The phase assemblage in the starting material of this sample (MB2-31) is plagioclase, clinopyroxene, glass, Fe-Mg-Al spinel oxide ($Mt_{16}Mgf_{67}Hc_8Z_9$), and hematite ($Hem_{85}Ilm_5Gk_{10}$) in the approximate order of decreasing volumetric abundance (Table 2.2). In contrast to the M-type starting material (MAm-36), plagioclase is the most abundant phase in this sample. Both plagioclase and clinopyroxene occur as feathery dendrites with a slight but complex zoning (Figures 3.1d - f). Unlike in the M-type starting material, both oxide phases are subhedral dendrites in this sample. Although the

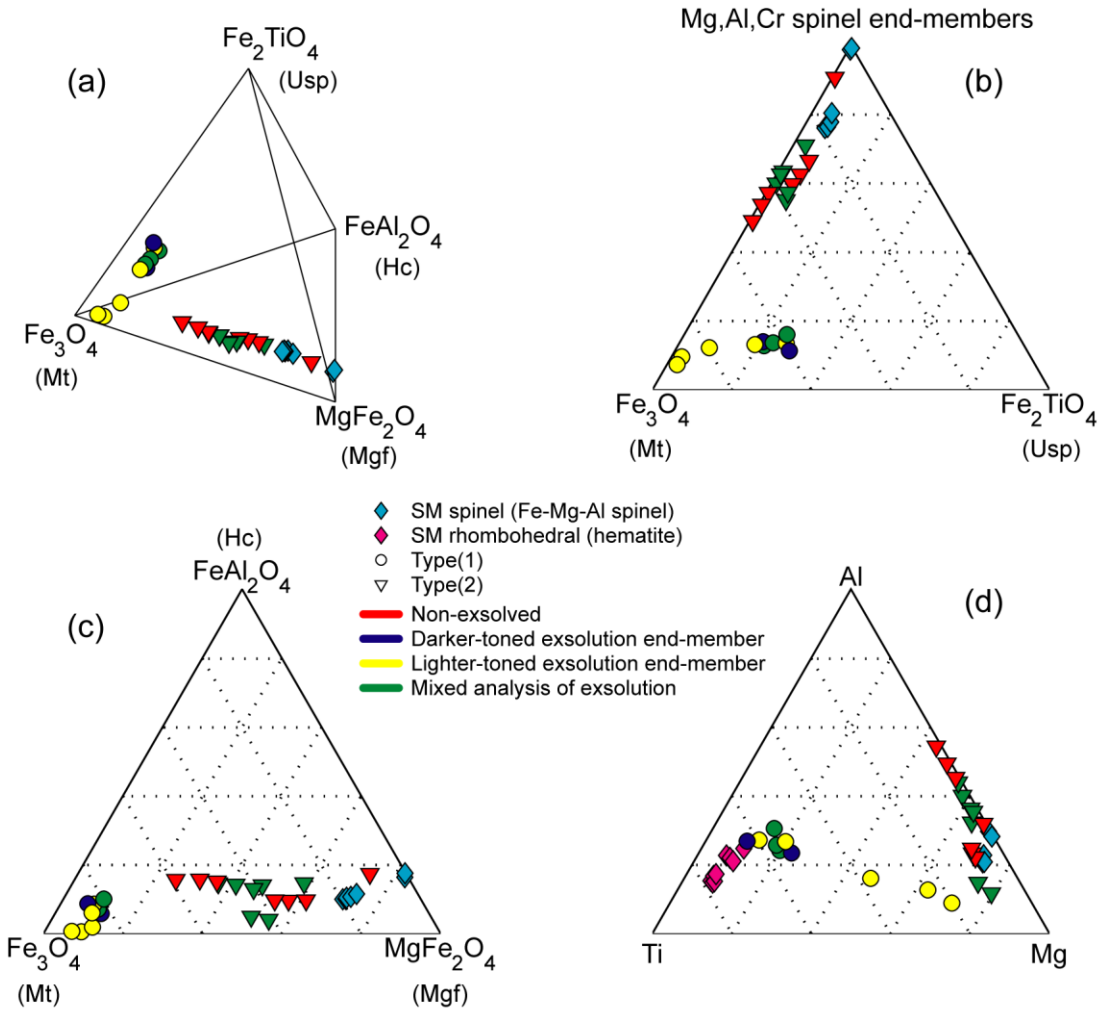

Figure 3.3. Quaternary and ternary diagrams displaying compositions of the oxide grains obtained by electron microprobe spot analyses on the Group 1 M-type starting material (MAm-36) and annealed sample (MAm-E-03). Note that they show abundance of some components relative to the others within the selected components, and not the absolute abundance. (a-c) are for spinel oxides. They show compositionally distinct two groups of oxides. (c) is a base ternary system in (a), or projection through ulvöspinel in (a). (d) shows rhombohedral phase as well, which implies rhombohedral phase in the starting material is parental to Type (1) exsolution and Mg-Al-rich ferrite in the starting material is parental to Type (2) exsolution. (Type (1): magnetite (light) – Al-bearing titanomagnetite (dark), Type (2): Fe-Mg spinel oxide (light) – Fe-Mg-Al spinel oxide (dark))

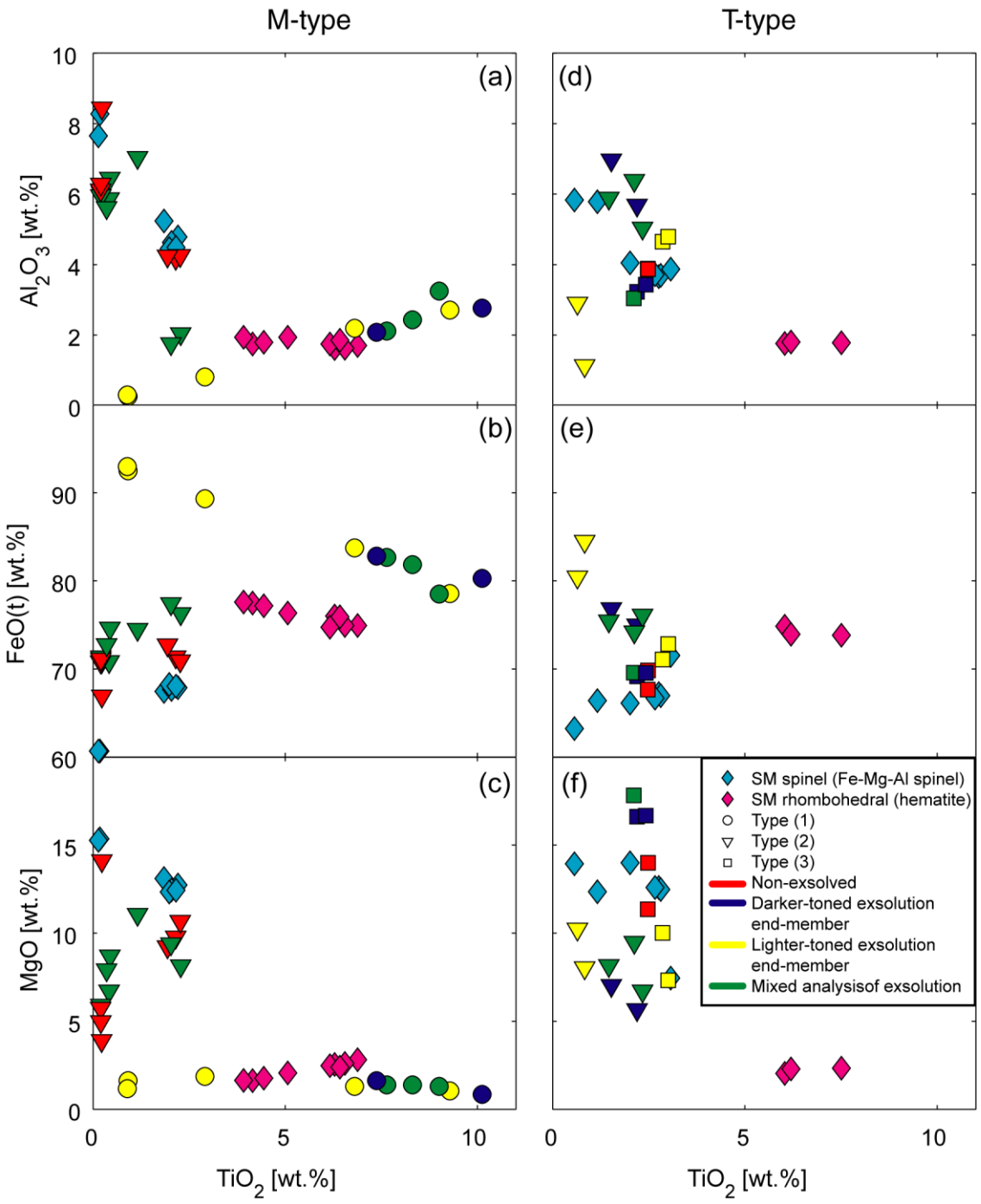

Figure 3.4. Variation plots of selected oxides against TiO_2 [wt.%] for the Group 1 M- and T-type starting materials and annealed samples (MAm-36, MB2-31, MAm/MB2 -E-03). (a-c): M-type. (d-f): T-type. Co-variation pattern is clearer in these binary systems. See text for detailed descriptions. (Type (1): magnetite (light) – Al-bearing titanomagnetite (dark), Type (2): Fe-Mg spinel oxide (light) – Fe-Mg-Al spinel oxide (dark), Type (3): Fe-Mg-Al spinel oxide (light) – Al-bearing magnesioferrite (dark))

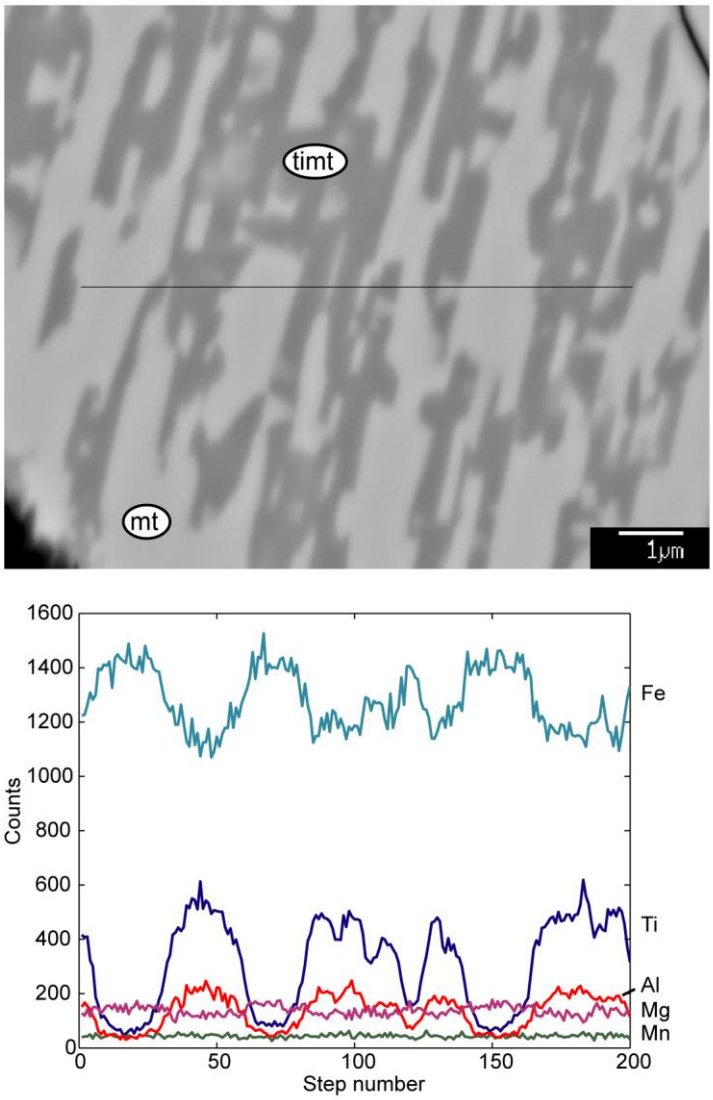

Figure 3.5. An element line scan of Type (1) exsolution (magnetite – Al-bearing titanomagnetite) in the Group 1 M-type annealed sample (MAm-E-03). The line scan was taken at the horizontal line shown in the back-scattered electron image with 5 pixels x 200 steps. The co-variations of elements are clear in this datum. See text for detailed descriptions. Abbreviations: mt=magnetite, timt= titanomagnetite.

small size (~1-5 μm) is dominant (Figures 3.1d and e), there are some ~1-70-μm-diameter grains (Figure 3.1f). Some small (Figure 3.1d) and large grains (Figure 3.1f) are faceted. Similarly to the M-type starting material, the two oxide phases have distinct tones relative to each other in BSE images reflecting their compositional difference; hematite is lighter-toned and Fe-Mg-Al spinel oxide is darker. Some oxide grains have both phases within the grains with a sharp phase boundary based on this tone difference, which was also the case for the M-type sample (Figure 3.1f).

The annealed run from this starting material (MB2-E-03) has the same phase assemblage as its starting material (MB2-31), except only for the onset of the exsolution in oxide phases (Table 2.2). The textural changes are also associated with these new phases. The exsolution of the oxide phases recognized visually in the BSE images took place for many grains but not all. There are three texturally distinct exsolved oxide phases in the sample. One is Type (2) exsolution with the end-members Fe-Mg spinel oxide ($Mt_{45}Mgf_{47}Z_8$) and Fe-Mg-Al spinel oxide ($Mt_{44}Mgf_{34}Hc_{13}Z_9$) (Figure 3.6). Another exsolution, Type (3) has Al-bearing magnesioferrite ($Mgf_{84}Hc_6Z_{10}$) and Fe-Mg-Al spinel oxide ($Mt_{34}Mgf_{47}Usp_8Hc_{10}Chr_1$) as end-members (Figure 3.7a and b). The remainder texturally resembles Type (1) titanomagnetite exsolution identified in the M-type annealed run product (Figure 3.6a). However, there is no quantitative compositional data with SiO_2 < 0.5 wt.% for those grains due to their high porosity. One type of non-exsolved phase texturally and compositionally confirmed was Fe-Mg-Al spinel oxide ($Mt_{17}Mgf_{66}Hc_8Z_9$) that has similar pore texture as Type (3) exsolution, which is described below (Figure 3.7d). For the textural description of Type (2) exsolution, see section 3.1.2.1. A difference of texture compared to the one in the M-type sample is that the

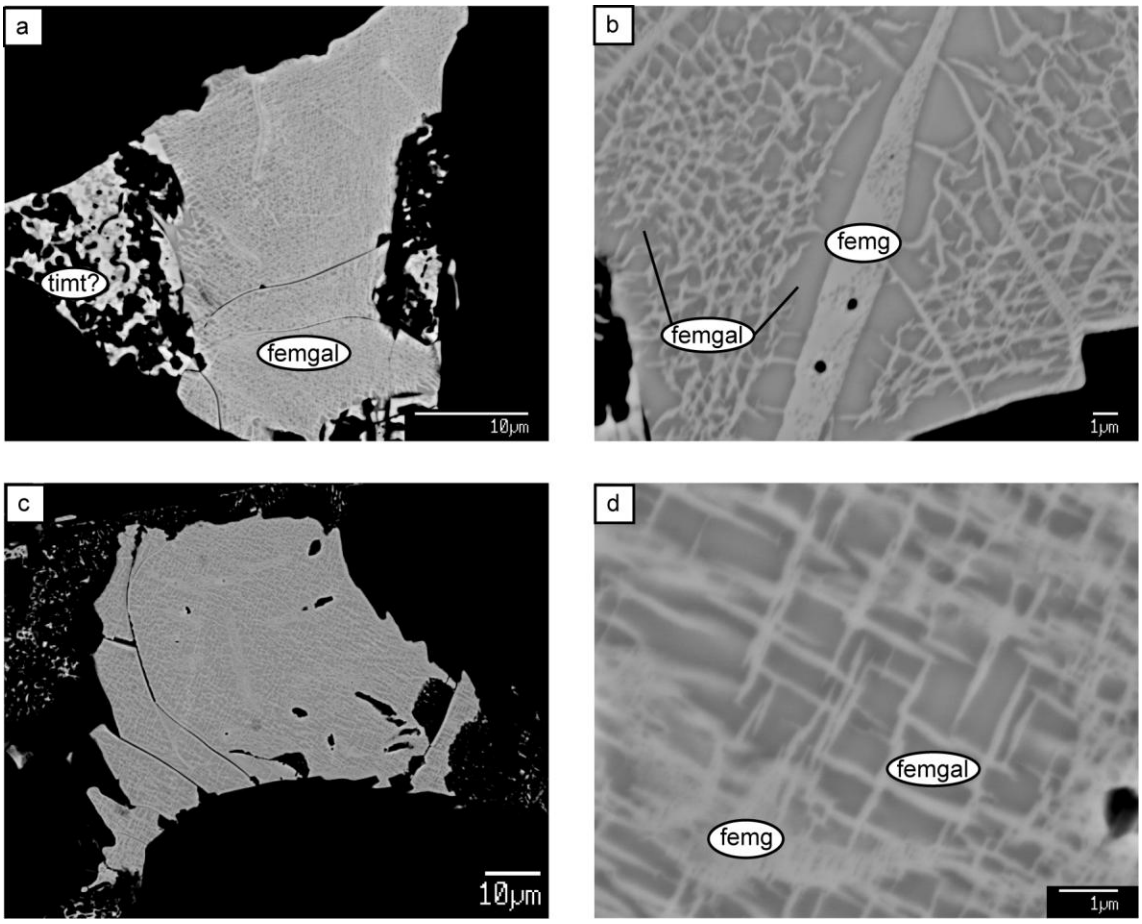

Figure 3.6. Back-scattered electron images of the Group 1 T-type annealed sample at 710 °C for 54 days (MB2-E-03). (a-d): Type (2) exsolution, Fe-Mg spinel oxide (light) – Fe-Mg-Al spinel oxide (dark). (a) also shows relatively rare highly porous and compositionally heterogeneous oxide phase, whose texture resembles that of exsolved titanomagnetite in M-type annealed sample (MAm-E-03) in Figure 3.2a. See text for detailed textural descriptions. Abbreviations: timt=titanomagnetite, femgal=Fe-Mg-Al spinel oxide, femg=Fe-Mg spinel oxide.

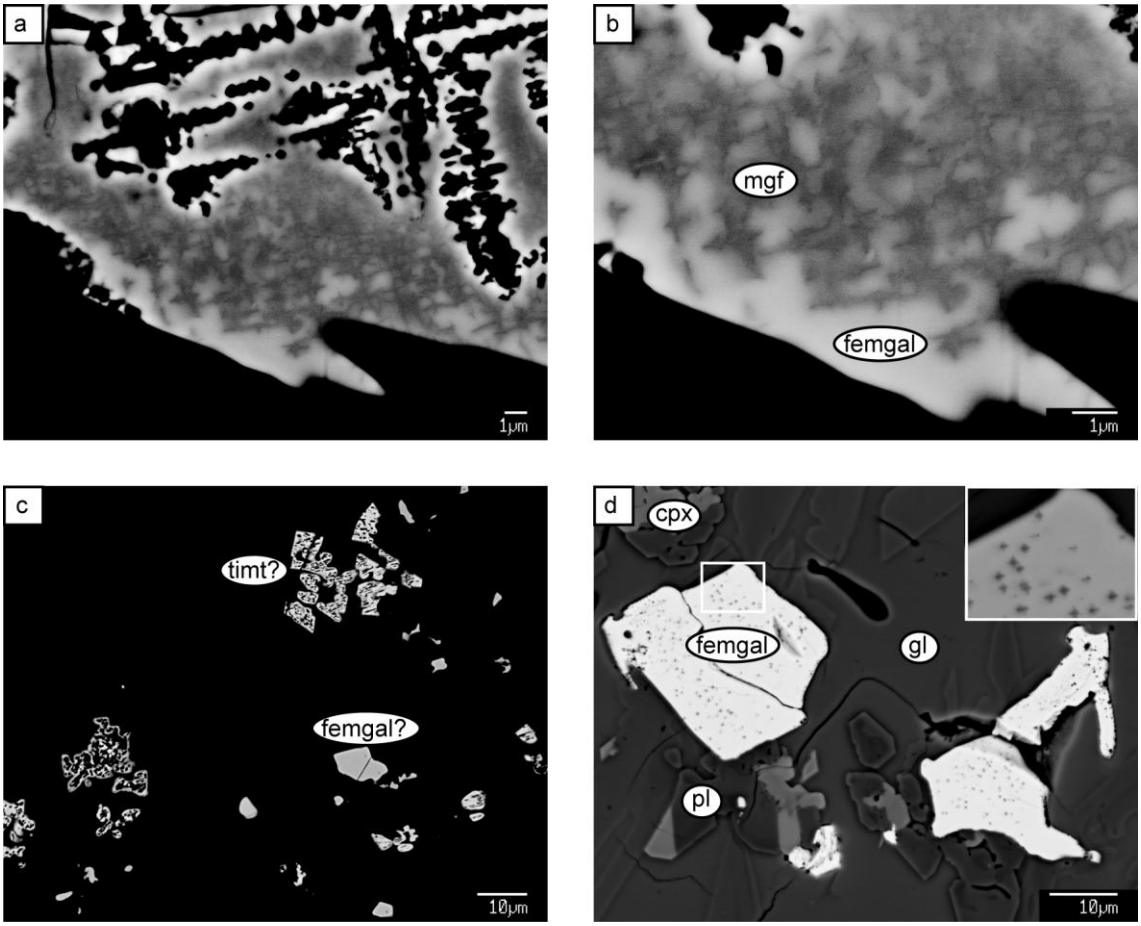

Figure 3.7. Back-scattered electron images of the Group 1 T-type annealed sample at 710 °C for 54 days (MB2-E-03) (Continued). (a-b): Type (3) exsolution, Fe-Mg-Al spinel oxide (light) – Al-bearing magnesioferrite (dark). (c) Porous grains that resembles titanomagnetite exsolution in M-type sample (MAm-E-03) in Figure 3.2a. (d) Non-exsolved oxide grains with pores texturally similar to that of grains with Type (3) exsolution. The inset in (d) is a magnified region in (d) to show pore morphology of these grains. See text for detailed textural descriptions. Abbreviations: femgal=Fe-Mg-Al spinel oxide, mgf=magnesioferrite, timt=titanomagnetite, gl=glass, pl=plagioclase, cpx=clinopyroxene.

grains with Type (2) exsolution in this sample exhibit coarser exsolution texture (Figure 3.6). The grains with the exsolution Type (3) consist of light-toned, blobby lamellae of Fe-Mg-Al spinel oxide and dark-toned Al-bearing magnesioferrite host (Figures 3.7a and b). The tone contrast between lamellae and host in BSE images is lower than Types (1) and (2), obscuring the boundaries between lamellae and host. The thickness of Fe-Mg-Al oxide lamellae is ~0.2-1 μm and that of Al-bearing magnesioferrite host is ~0.2-0.5 μm. The distribution of the lamellae and host is heterogeneous. This type of exsolution also accompanies pore formation along exsolution texture similarly to Type (1). Also, it shows a step-like or cubic structure of the pores. The oxide crystals that seem to have undergone Type (1) exsolution consist of dark-toned (submicron) and light-toned oxide phases (submicron-2 μm) with undefined shapes in a BSE image and are highly porous (Figure 3.6a). There are some grains that do not seem to have exsolution exhibit pores with cubic shapes aligning in the same orientation, which resembles pores in Type (3) grains as mentioned above (Figure 3.7d). Another group of oxide grains that do not have exsolution texture in BSE images is highly porous with a preferred orientation of pores with a possible reaction rim (Figure 3.7c), which resembles texture for some of Type (1) grains in M-type sample. Quantitative compositional analysis on this group was not possible due to high porosity.

The compositional characteristics of the oxide phases seen in those plots suggest that Fe-Mg-Al spinel oxide in starting material is parental to both Type (2) and (3) exsolution (Figures 3.4d - f and 3.8). For the starting material, volumetrically subordinate large grains were analyzed by EPMA because satisfactory results (SiO_2 < 0.5 wt.%) was not likely to be obtained for small grains. Regarding the cation partitioning pattern

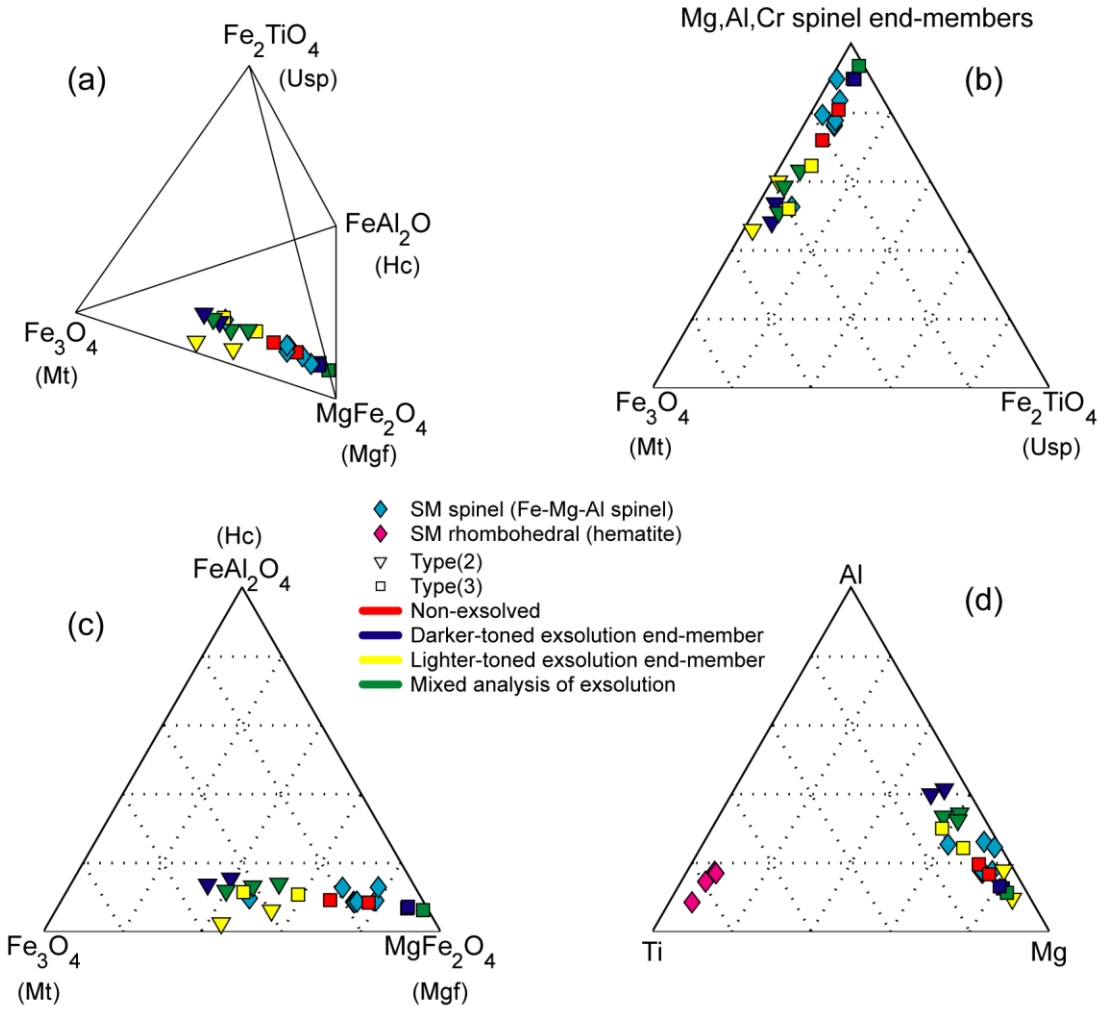

Figure 3.8. Quaternary and ternary diagrams displaying compositions of the oxide grains obtained by electron microprobe spot analyses on the Group 1 T-type starting material (MB2-31) and annealed sample (MB2-E-03). Note that they show abundance of some components relative to the others within the selected components, and not the absolute abundance. The type and end-members of the quaternary/ternary system are identical to those for M-type samples in Figure 3.3. (a-c) are for spinel oxides. (c) is a base ternary system in (a), or projection through ulvöspinel in (a). Although all the oxides are located in the similar positions, two types of exsolution, Types (2) and (3), are distinct. See text for detailed descriptions. (d) shows rhombohedral phase as well. (Type (2): Fe-Mg spinel oxide (light) – Fe-Mg-Al spinel oxide (dark), Type (3): Fe-Mg-Al spinel oxide (light) – Al-bearing magnesioferrite (dark))

between exsolved phases in Type (2) exsolution, there is a negative correlation between Mg and Al (Figures 3.4d and f, 3.8d, and 3.9). There are also positive correlations between Mg and Fe (Figures 3.4e and f) and between Al and Ti (Figures 3.4d and 3.9), where Ti is a minor element in this system. For Type (3) exsolution, the correlations are the same as in Type (2) (Figure 3.10), except for Mg and Fe being negatively correlated (Figures 3.4e and f). Also, Mg partitioning between exsolved phases is amplified at the expense of Al compared to Type (2) (Figures 3.4d and f, 3.8a and c, and 3.10). The oxide grains in annealed run product that do not texturally exhibit exsolution are compositionally similar to the Fe-Mg-Al spinel oxide phase from its starting material (Figures 3.4d - f and 3.8).

3.1.3 Experimental Group 2

3.1.3.1 Time-Series Experiments

3.1.3.1.1 Meteorite-Type

The phase assemblage in the starting material of this sample (MAm-51) is clinopyroxene, glass, plagioclase, and titanomagnetite ($Mt_{44}Usp_{38}Mgf_{11}Hc_7$), in the approximate order of decreasing volumetric abundance (Table 2.2 and Figure 3.11a). Clinopyroxene crystals in this sample are subhedral, elongated, and blocky with a slight but complex zoning. Plagioclase occurs as euhedral tabular crystals. Titanomagnetite crystals are euhedral, equant, and ~30-80 μm in diameter. There is a subordinate population of rounded and equant ~5-15-μm-diameter grains that occur as clusters. All of these phases tend to have melt inclusions, except the second type of titanomagnetite crystals. Thus, the phase assemblage as well as texture is distinct from Group 1 M-type

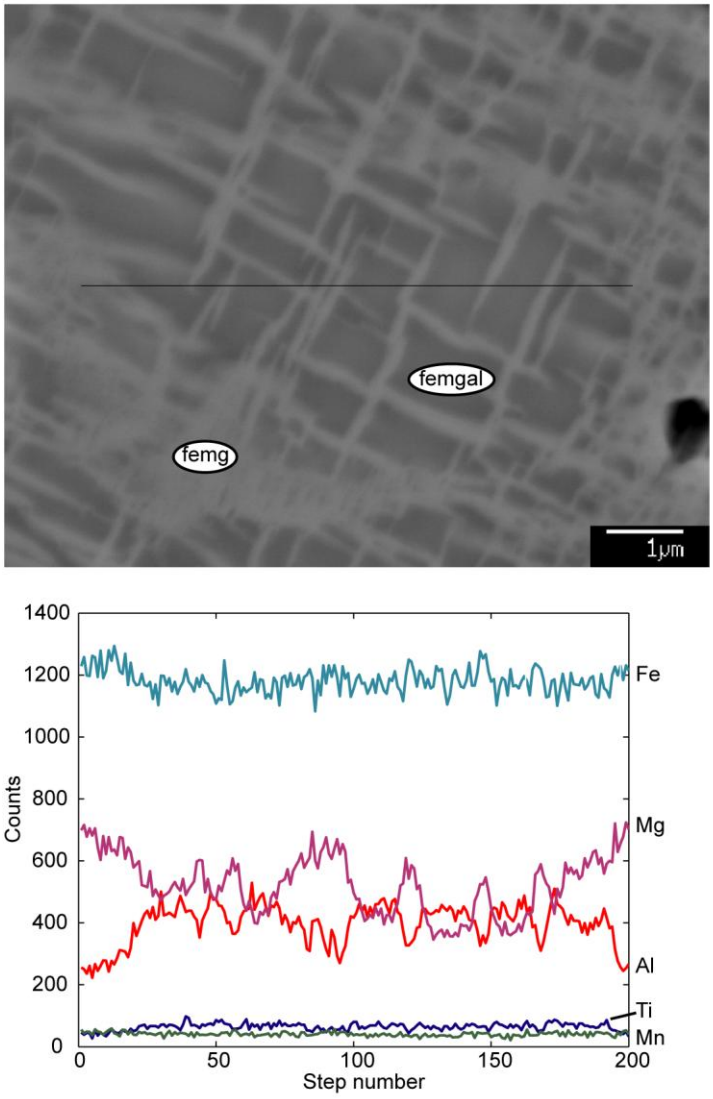

Figure 3.9. An element line scan of Type (2) exsolution (Fe-Mg spinel oxide – Fe-Mg-Al spinel oxide) in the Group 1 T-type annealed sample (MB2-E-03). The line scan was taken at the horizontal line shown in the back-scattered electron image with 5 pixels x 200 steps. The co-variations of elements are clear in this datum. See text for detailed descriptions. Abbreviations: femg= Fe-Mg spinel oxide (light), femgal=Fe-Mg-Al spinel oxide (dark).

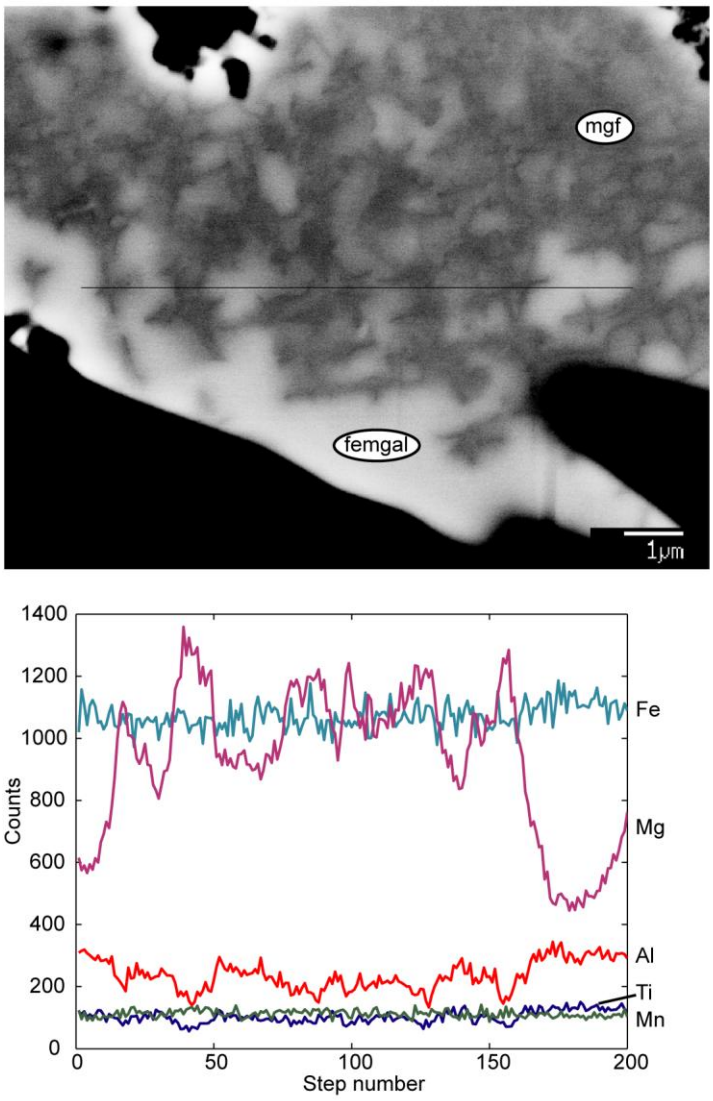

Figure 3.10. An element line scan of Type (3) exsolution (Fe-Mg-Al spinel oxide – Al-bearing magnesioferrite) in the Group 1 T-type annealed sample (MB2-E-03). The line scan was taken with 5 pixels x 200 steps at the center of the field of view. The co-variations of elements are clear in this data. See text for detailed descriptions. Abbreviations: femgal= Fe-Mg-Al spinel oxide (light), mgf=magnesioferrite (dark).

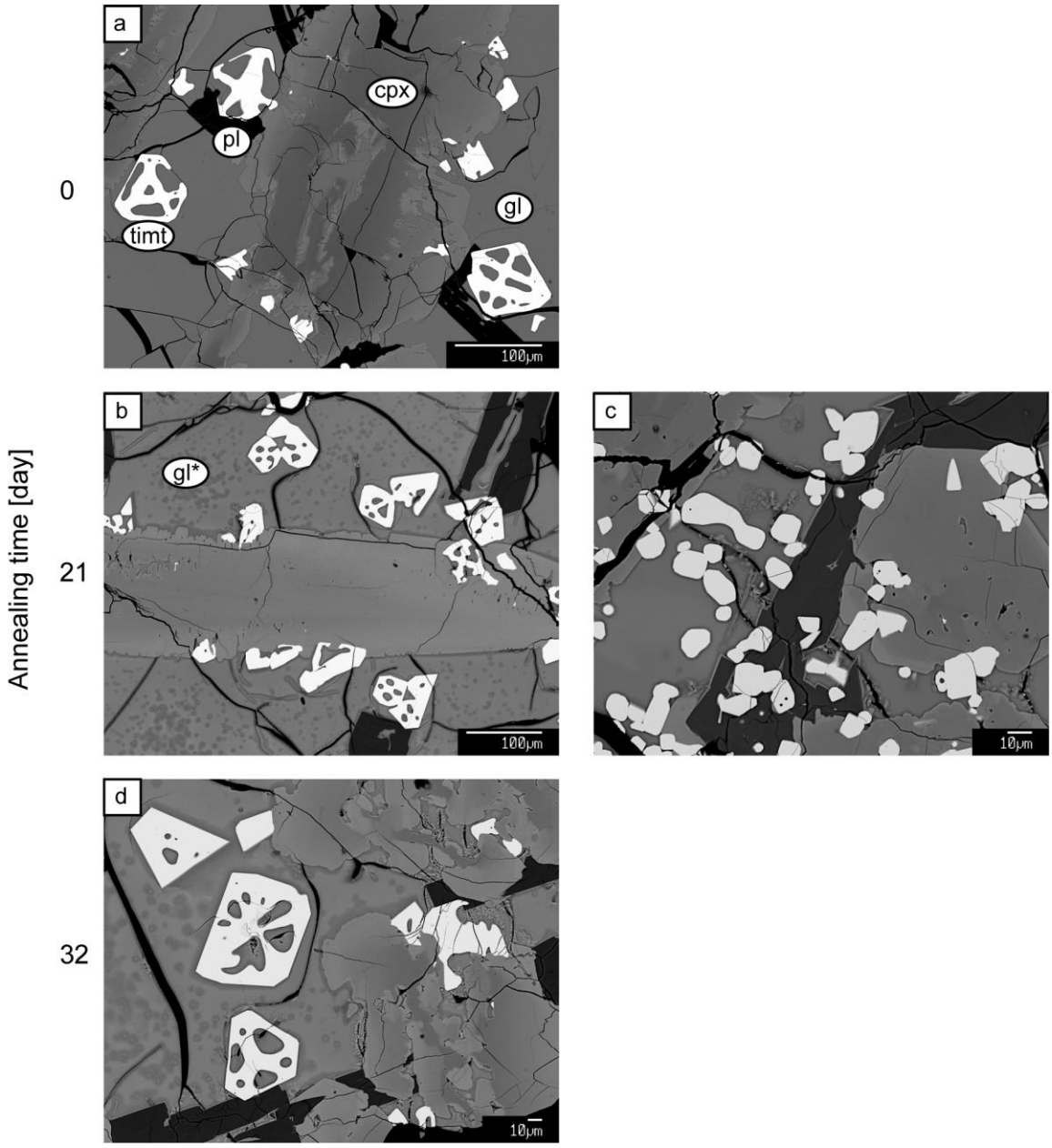

Figure 3.11. Back-scattered electron images of the Group 2 M-type starting material (MAm-51) and some of the time-series annealed samples at 650 °C (MAm-E-09 and E-10). The tone of the oxides may appear to be different in the images due to different brightness/contrast settings. As in (b-c), some samples have texturally distinct group of oxides. Re-crystallization of glass is visually recognizable after annealing. Abbreviations: cpx=clinopyroxene, pl=plagioclase, timt=titanomagnetite, gl=glass, gl*=devitrified glass.

starting material although the same reagent mixture was employed for the starting material syntheses.

The time-series annealed runs from this starting material (MAm-E-09 – E-13) have the same phase assemblage as its starting material, except for the devitrification (Table 2.2, Figures 3.11b - d and 3.12). The devitrified parts of glass appear in the BSE image as colloform aggregates of fibrous crystals, and the amount increases with time. Its identity is uncertain since no quantitative data was obtained. There is no other noteworthy textural change with time or visually recognizable exsolution in titanomagnetite grains. The median compositions of titanomagnetite in the time-series samples are $Mt_{49}Usp_{35}Mgf_{9}Hc_{7}$, $Mt_{50}Usp_{35}Mgf_{8}Hc_{7}$, $Mt_{51}Usp_{34}Mgf_{8}Hc_{7}$, $Mt_{49}Usp_{36}Mgf_{8}Hc_{7}$, and $Mt_{53}Usp_{32}Mgf_{8}Hc_{7}$, in the order of increasing annealing time.

There is no compositional change with time in titanomagnetite except for MgO and TiO_2 contents (Figures 3.13a, 3.14a, and 3.15). The concentrations of MgO and TiO_2 decrease with time, making the composition of titanomagnetite approach the end-member magnetite (Figures 3.13a, 3.14a, and 3.15d). Element maps obtained for starting material and some of the annealed runs show enrichment of Mg in glass adjacent to titanomagnetite grains compared to groundmass glass (Appendix M).

3.1.3.1.2 Terrestrial-Type

The phase assemblage in the starting material of this sample (MB2-48) is plagioclase, clinopyroxene, glass, olivine, titanomagnetite ($Mt_{17}Usp_{47}Mgf_{27}Hc_{7}Chr_{2}$), and ilmenite ($Hem_{15}Ilm_{64}Gk_{21}$) in the approximate order of decreasing volumetric abundance (Table 2.2 and Figure 3.16a). As for olivine, it is based on a similar but still distinct tone from pyroxene in BSE images and the fact that the CIPW norm for this starting material

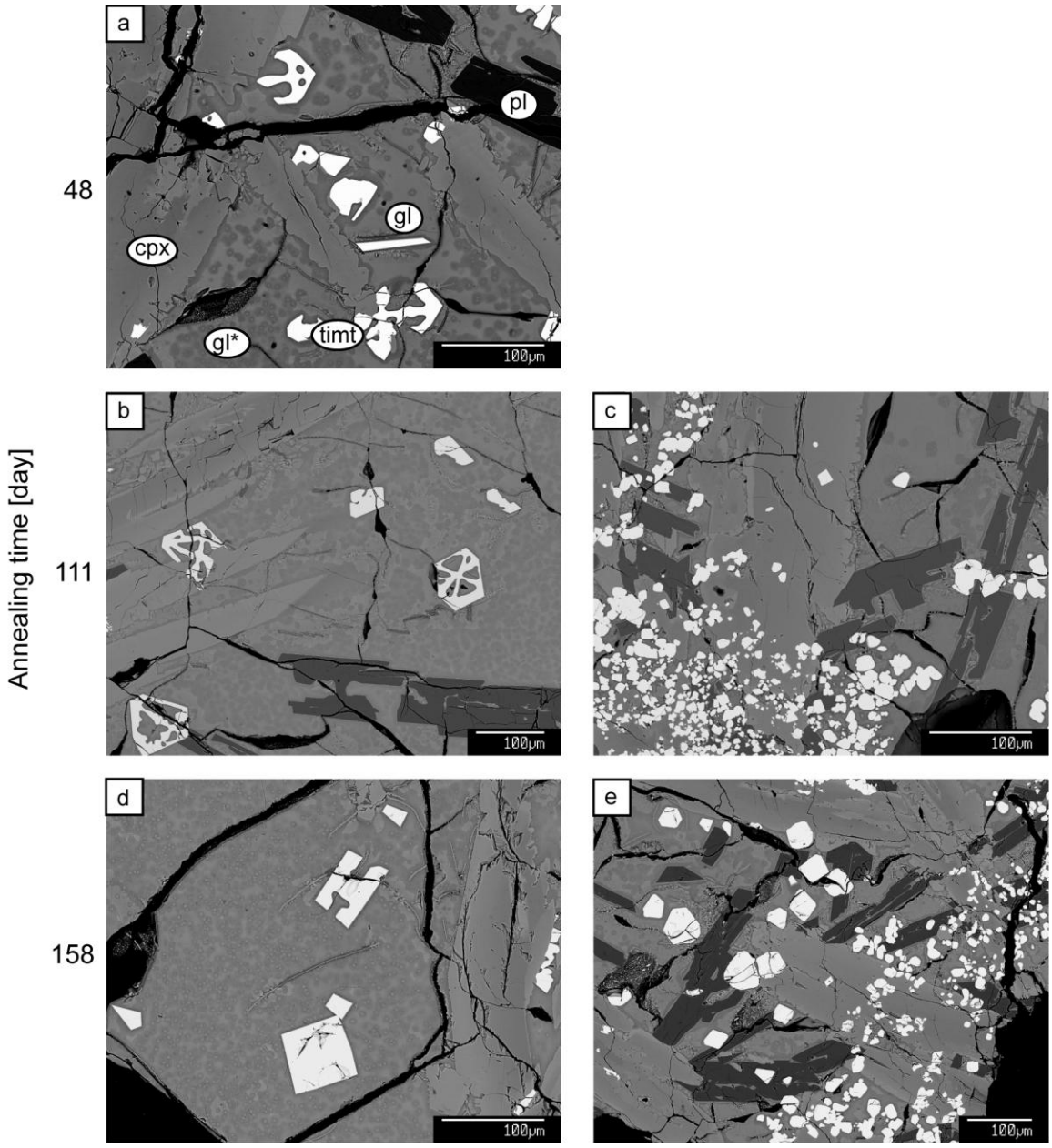

Figure 3.12. Back-scattered electron images of the Group 2 time-series M-type annealed samples at 650 °C (MAm-E-11 – E-13). The tone of the oxides may appear to be different in the images due to different brightness/contrast settings. As in (b-c) and (d-e), some samples have texturally distinct group of oxides. A progression of the glass re-crystallization is significant. Abbreviations: cpx=clinopyroxene, pl=plagioclase, timt=titanomagnetite, gl=glass, gl*=devitrified glass.

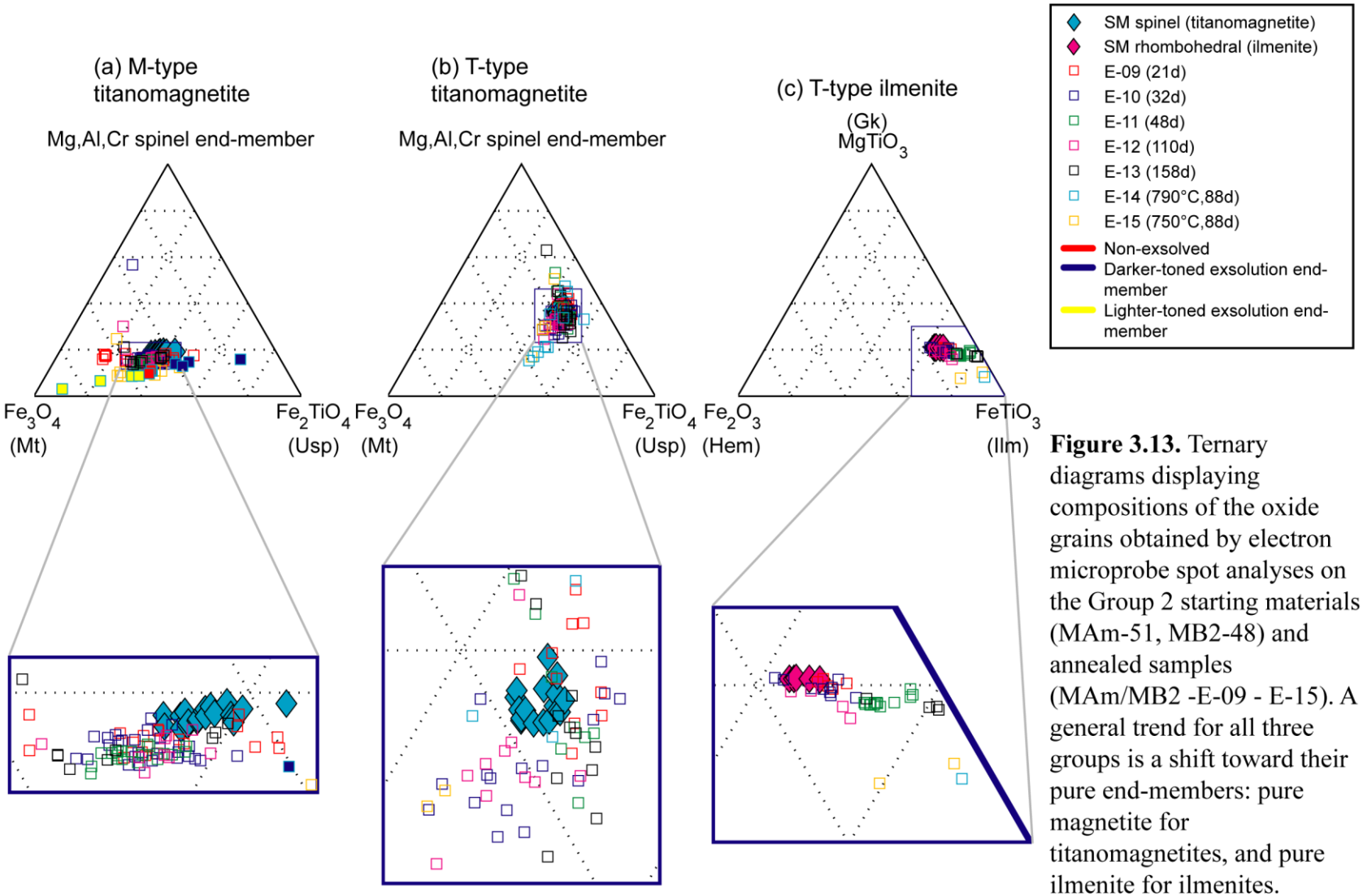

Figure 3.13. Ternary diagrams displaying compositions of the oxide grains obtained by electron microprobe spot analyses on the Group 2 starting materials (MAm-51, MB2-48) and annealed samples (MAm/MB2 -E-09 - E-15). A general trend for all three groups is a shift toward their pure end-members: pure magnetite for titanomagnetites, and pure ilmenite for ilmenites.

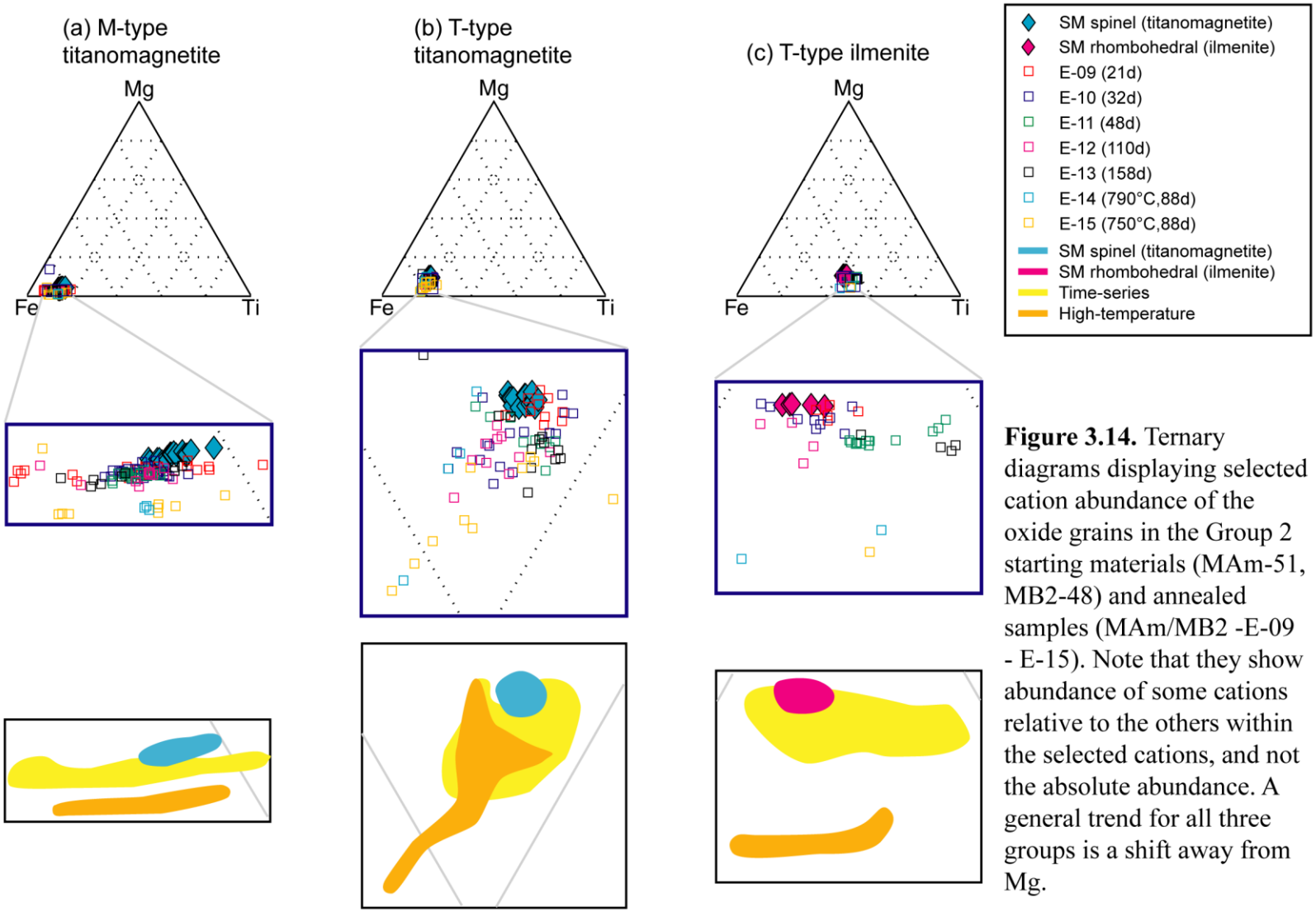

Figure 3.14. Ternary diagrams displaying selected cation abundance of the oxide grains in the Group 2 starting materials (MAm-51, MB2-48) and annealed samples (MAm/MB2 -E-09 - E-15). Note that they show abundance of some cations relative to the others within the selected cations, and not the absolute abundance. A general trend for all three groups is a shift away from Mg.

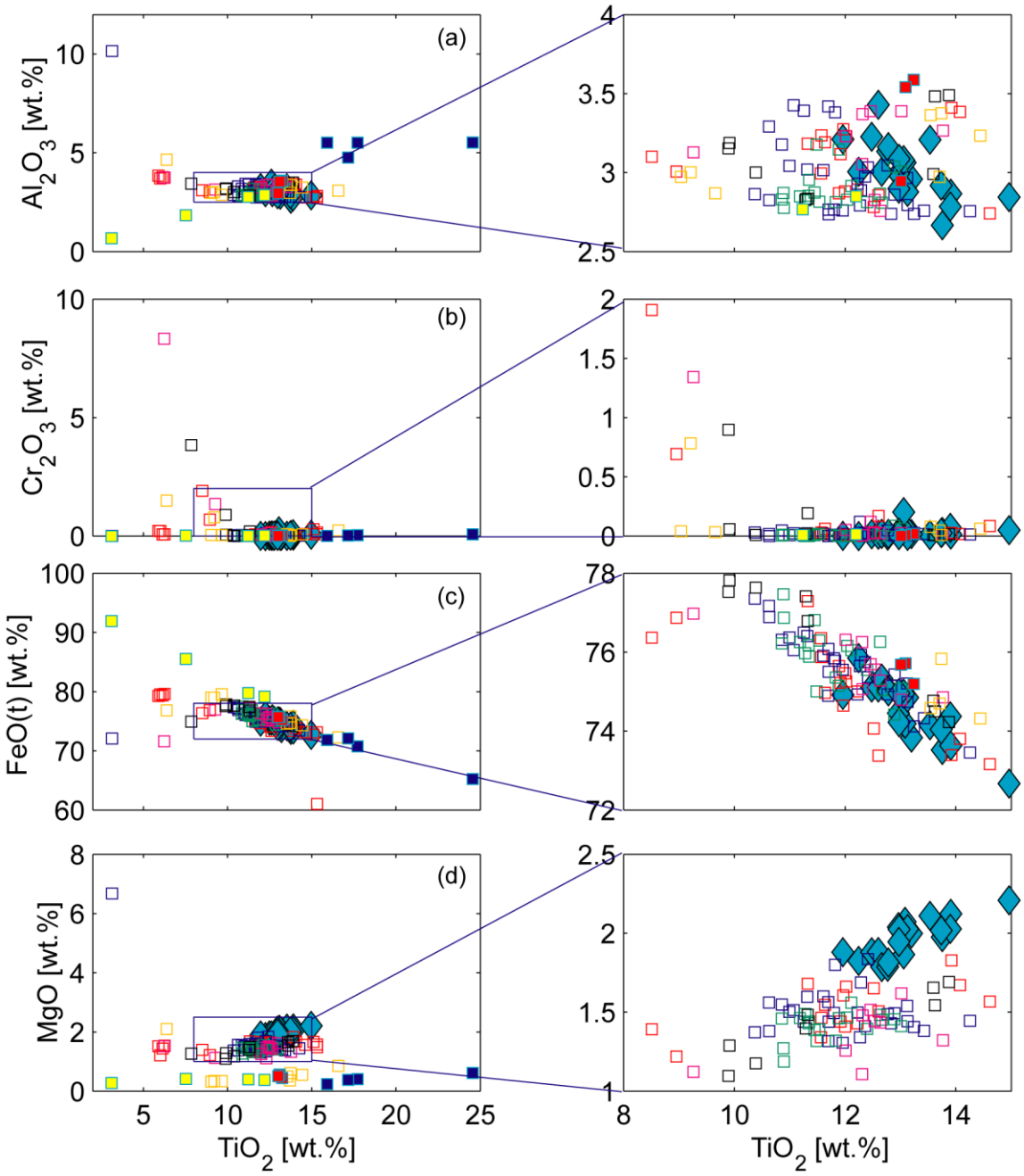

Figure 3.15. Variation plots of some oxides against TiO_2 [wt.%] for the Group 2 M-type starting material (MAm-51) and annealed samples (MAm-E-09 - E-15). The co-variation pattern is clearer in these binary systems: a slight decrease in TiO_2, a clear decrease in MgO, and an increase in FeO(t) are visible.

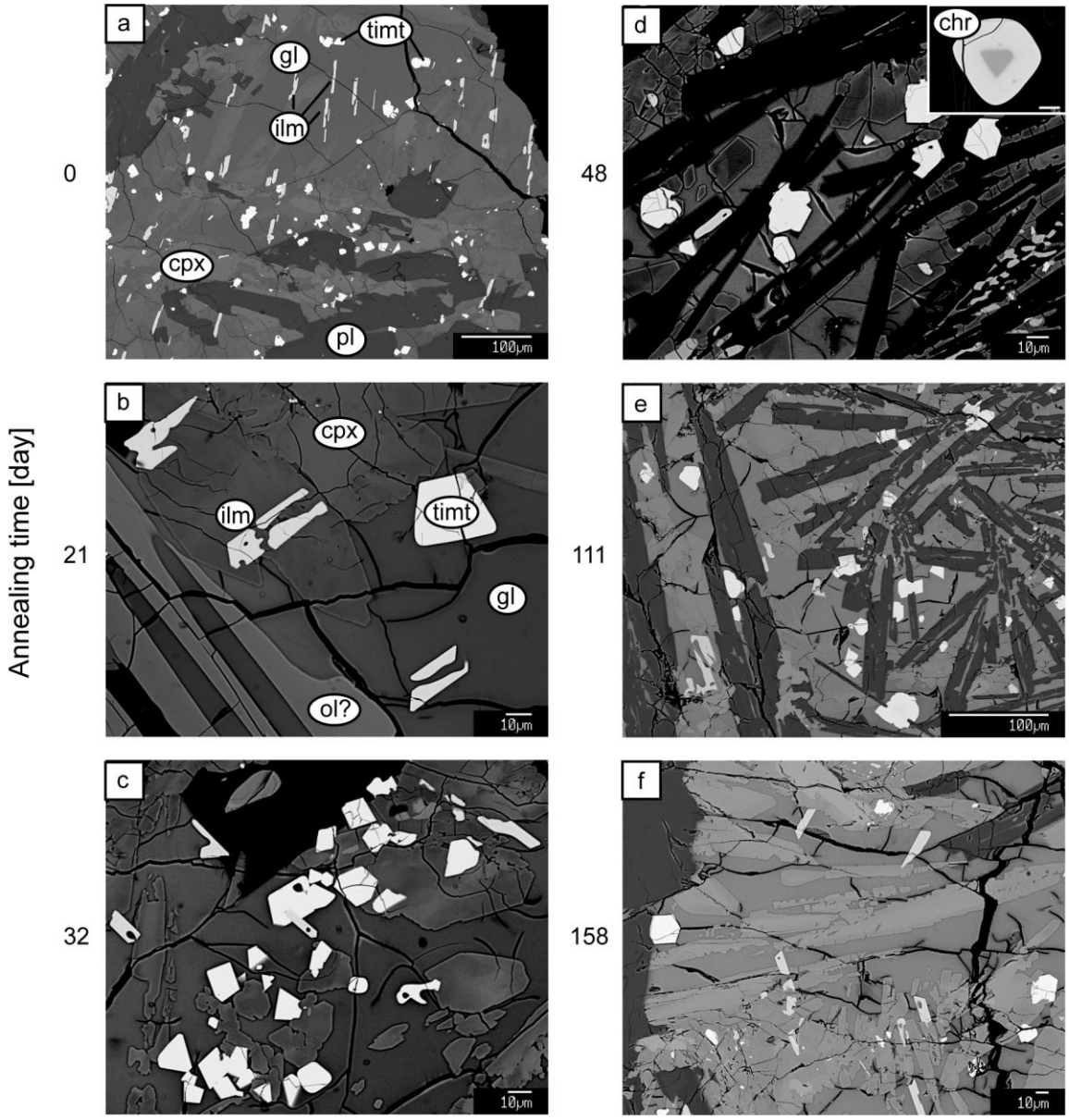

Figure 3.16. Back-scattered electron images of the Group 2 T-type starting material (MB2-48) and the time-series annealed samples at 650 °C (MB2-E-09 – E-13). The tone of the oxides may appear to be different in the images due to different brightness/contrast settings. Relative tone difference of titanomagnetite and ilmenite still holds within each image (titanomagnetite is lighter with respect to ilmenite). (d) shows a representative chromite grain seen in the sample in inset. There was no change in petrography with annealing time for this set of samples. Scale bars are 100 μm for (a) and (e). Those for (b)-(d) (including inset in (d)) and (f) are 10 μm. Abbreviations: cpx=clinopyroxene, pl=plagioclase, timt=titanomagnetite, ilm=ilmenite, gl=glass, ol=olivine, chr=chromite.

has some olivine. Compositional confirmation would eventually be ideal although it was not the essence of this study. Plagioclase occurs as faceted, highly elongated hopper crystals. Clinopyroxene crystals in this sample are euhedral feathery dendrites with a slight but complex zoning. Olivine crystals are anhedral. Titanomagnetite crystals are euhedral, equant, and ~5-10-μm in diameter. Ilmenite crystals are euhedral and elongated ~5x30 μm in length. There seems to be a preferred orientation in ilmenite grains although distance between grains in thin sections is usually more than ~30 μm. In BSE images, ilmenite appears to be slightly darker-toned compared to titanomagnetite. Similarly to the M-type sample, the starting material in Group 2 is distinct from the one in Group 1. In this case, it is not surprising considering difference in the reagent mixtures used to synthesize the T-type starting materials (see section 3.1.1).

In general, the time-series annealed runs from this starting material (MB2-E-09 – E-13) have the identical phase assemblage as its starting material, and there is no textural difference from its starting material (Table 2.2 and Figures 3.16b - f). The run annealed for 48 days (MB2-E-11) has some grains that have Cr-rich core surrounded by titanomagnetite rim (Figure 3.16d) as well as Cr-rich grains without zoning. Considering a possible heterogeneity in the starting material mentioned earlier, it is most likely a heritage from the starting material, and not something developed during annealing. Because such a species occurs only in this sample in the time-series runs and the five end-member calculation for compositional characterization of titanomagnetite does not apply to it (a deficiency of Fe occurs using the selected end-members), it is not included in the compositional descriptions or plots except non-zoned Cr-rich grains in variation plot (Figure 3.17). Their compositions are listed in Appendix H. The median

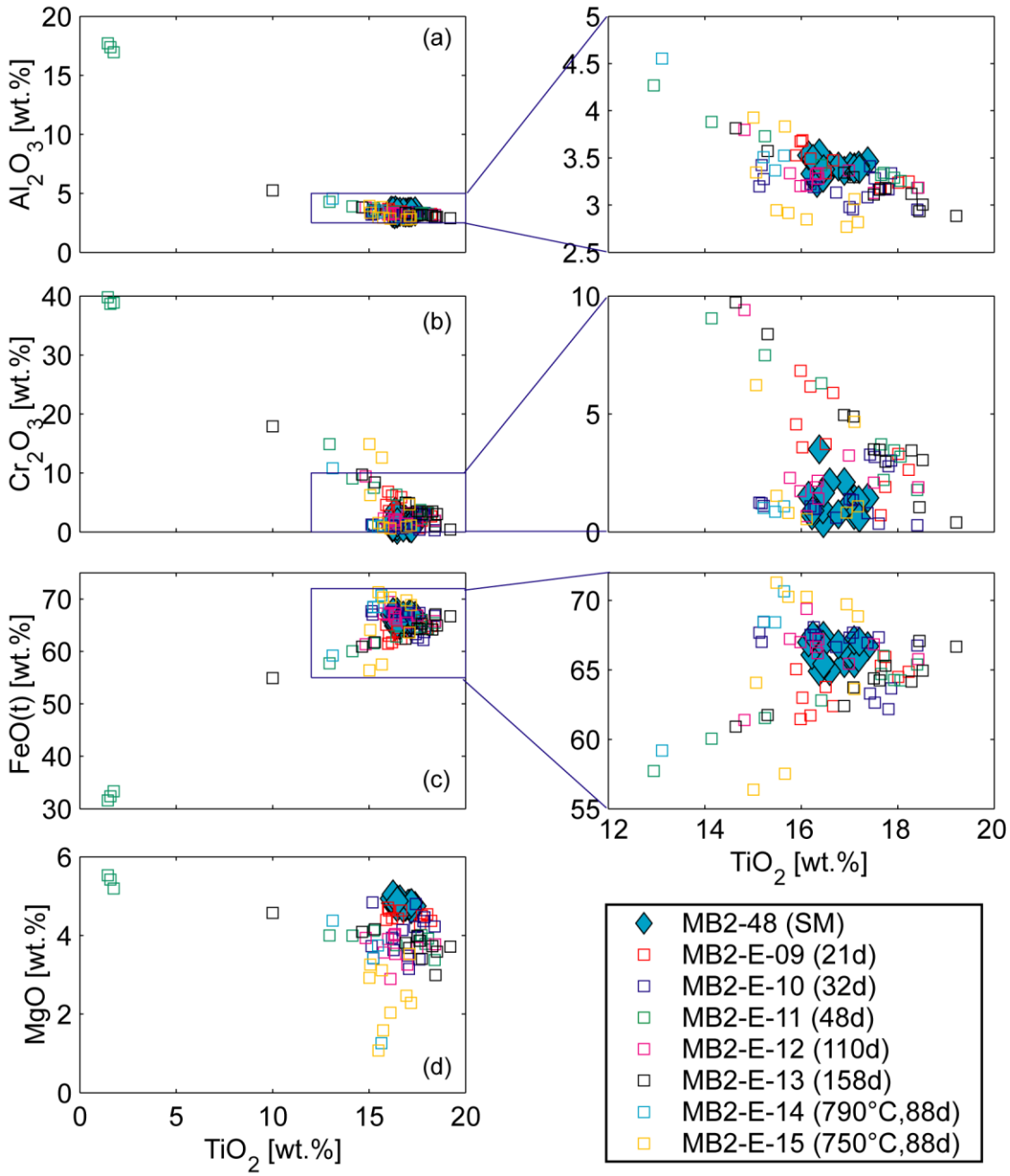

Figure 3.17. Variation plots of selected oxides against TiO_2 [wt.%] for the Group 2 T-type starting material (MB2-48) and annealed samples (MB2-E-09 – E-15). A clear decrease in MgO after annealing is visible in this set of samples. Some Cr-rich grains were present in this set of sample, and they are obscuring the trend with time due to their depletion in FeO(t) and enrichment in Al_2O_3.

compositions of titanomagnetite in the time-series samples are $Mt_{14}Usp_{47}Mgf_{25}Hc_8Chr_6$, $Mt_{21}Usp_{48}Mgf_{22}Hc_7Chr_2$, $Mt_{15}Usp_{50}Mgf_{22}Hc_7Chr_6$, $Mt_{21}Usp_{47}Mgf_{21}Hc_8Chr_3$, and $Mt_{16}Usp_{50}Mgf_{22}Hc_7Chr_5$, and those of ilmenite are $Hem_{12}Ilm_{68}Gk_{20}$, $Hem_{13}Ilm_{68}Gk_{19}$, $Hem_8Ilm_{74}Gk_{18}$, $Hem_{13}Ilm_{69}Gk_{18}$, and $Hem_2Ilm_{81}Gk_{17}$, in the order of increasing annealing time.

A difference in titanomagnetite composition compared to the M-type samples is that the T-type samples contain some chromite component (Figure 3.17c). This feature is distinct from Group 1 samples as well. Similarly to Group 2 M-type samlple, the compositions of titanomagnetite and ilmenite become depleted in MgO with time and approaches to end-member magnetite composition (Figures 3.13b - c, 3.14b - c, and 3.17d). The titanomagnetite composition approach toward magnetite is less obvious compared to M-type samples due to a presence of Cr-rich grains that are depleted in FeO(t).

3.1.3.2 High-Temperature Experiments

The starting materials for the high-temperature runs are the same as for time-series runs in the previous section (see section 3.1.3.1).

3.1.3.2.1 Meteorite-Type

The annealed run at 750 °C (MAm-E-15) has the same phase assemblage as its starting material, except for the devitrification and an extensive pore and olivine reaction rim formation in titanomagnetite grains ($Mt_{50}Usp_{40}Mgf_3Hc_7$) (Table 2.2 and Figure 3.18). The annealed run at 790 °C (MAm-E-14) showed exsolution texture in some titanomagnetite crystals in addition to the devitrification and pore and olivine reaction

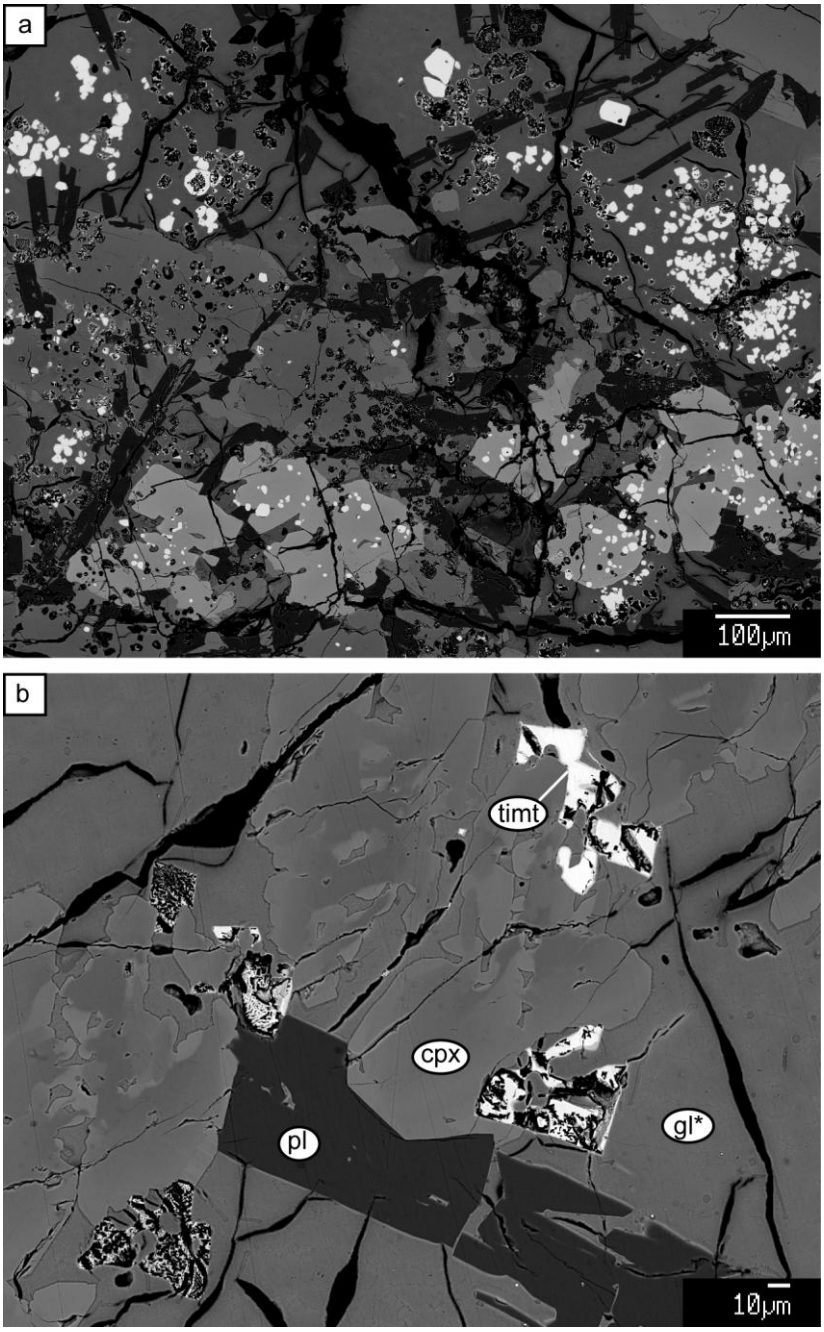

Figure 3.18. Back-scattered electron images of the Group 2 M-type high-temperature annealed sample at 750 °C (MAm-E-15). The tone of the oxides may appear to be different in the images due to different brightness/contrast settings. As it was described for the time-series samples in Figure 3.11 and 3.12, it is shown in (a-b) that there are two texturally distinct groups of titanomagnetites. However, they both show an extensive development of pores in oxide grains. Glass is now re-crystallized completely. In (b), some grains possess reaction rim, most likely olivine (see text). Abbreviations: cpx=clinopyroxene, gl*=devitrified glass, pl=plagioclase, timt=titanomagnetite.

rim formation in the oxides similarly to the run at 750 °C (Figure 3.19). The devitrification for both runs shows a similar texture as those observed in the time-series runs, colloform aggregates of fibrous crystals. In both samples, all the glass including melt inclusions in the oxides devitrified, making the whole rock hollocrystalline. Another textural characteristic common in these two runs, an extensive development of pores and reaction rim in titanomagnetite grains, was also observed in the grains that underwent non-pure titanomagnetite exsolution in the Group 1 M-type annealed run (see section 3.1.2.1).

The exsolved titanomagnetite grains in the run at 790 °C underwent magnetite ($Mt_{88}Usp_9Z_3$) – Al-bearing titanomagnetite ($Mt_{15}Usp_{69}Hc_{12}Z_4$) exsolution. Therefore, we classify this exsolution into Type (1). The exsolved grains consist of dark-toned host of Al-bearing titanomagnetite and light-toned, nearly equant, blobby lamellae of magnetite in BSE images (Figures 3.19a - e). The size of magnetite lamellae is submicron to slightly above 1 μm in diameter. A distribution of the lamellae is heterogeneous for a whole grain whereas it is homogeneous in a local scale. They seem to align in the same crystallographic orientation as the titanomagnetite host titanomagnetite: well-defined edges of some magnetite grains are approximately parallel to the edges of the host titanomagnetite (Figures 3.19b and c). The exsolved grains usually have pores that tend to have cubic structure aligned with the same orientation as magnetite phase (Figures 3.19a – d). It seems they tend not to occur near the surface of the host grain, which is in contact with the olivine reaction rim. To note, among the three rock chips in the thin section for 790 °C run, only one had titanomagnetite oxide grains, and 3 out of ~15 titanomagnetite grains (including those appeared as fragments in two-dimension) showed

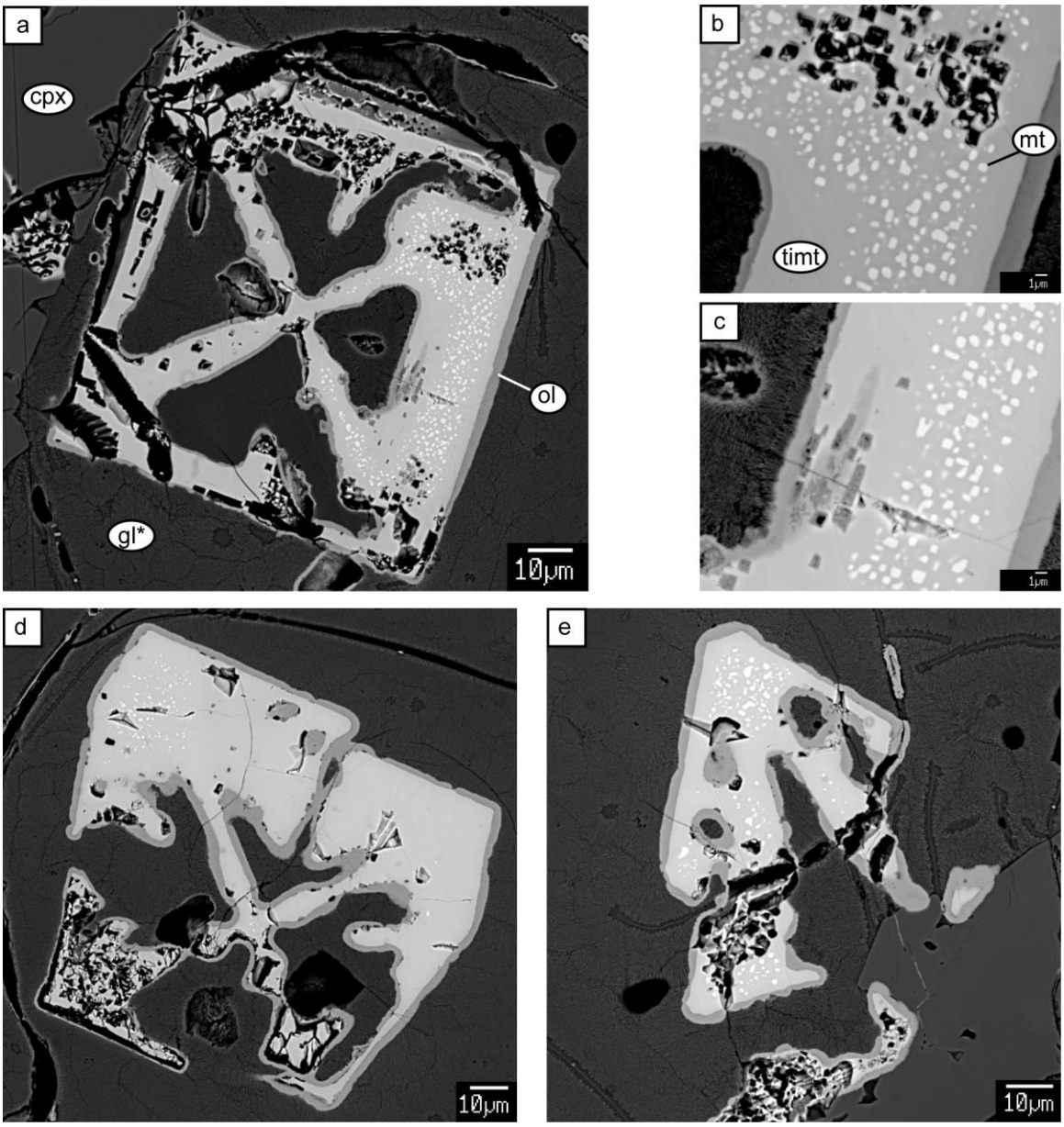

Figure 3.19. Back-scattered electron images of the exsolved titanomagnetites in the Group 2 M-type high-temperature annealed sample at 790 °C (MAm-E-14). The tone of the oxides may appear to be different in the images due to different brightness/contrast settings. (a-e): Type (1) exsolution, magnetite (light) – Al-bearing titanomagnetite (dark). (b-c) are regions in (a). An alignment of pores and exsolved magnetite phase is more obvious in the high-magnification images as in (b) and (c). All of the exsolved grains possess pores and olivine reaction rim. Abbreviations: cpx=clinopyroxene, ol=olivine, gl*=devitrified glass, mt=magnetite, timt=titanomagnetite.

optically observable exsolution texture by electron microprobe. The non-exsolved (at least in BSE images; Figure 3.20) titanomagnetite ($Mt_{51}Usp_{38}Mgf_3Hc_8$) was also accompanied by the olivine reaction rim.

Similarly to the time-series runs, there is depletion in MgO and TiO_2 for both high-temperature runs, and the compositions approach toward end-member magnetite (Figures 3.13a, 3.14a, and 3.15d). The partitioning of elements between two exsolved oxide phases in Type (1) exsolution in the 790 °C sample is the same as that of the Group 1 M-type annealed run: there is a clear positive correlation between Ti and Al that is negatively correlated with Fe between the exsolved phases (see section 3.1.2.1; Figures 3.15a and c, and 3.21). From the line scan, there seems to be a slight co-variation of Fe and Mg although Mg is a trace element in this system (Figure 3.21). The quantitative composition data of olivine rim in this sample was obtained by EPMA, although the calibration for oxides (as opposed to olivine) was used. However, it provides us with the approximate composition as fayalite-rich olivine (Appendix J).

3.1.3.2.2 Terrestrial-Type

Except for sub-micron equant devitrified parts of glass, the annealed runs at 750 and 790 °C (MB2-E-15 and E-14) have the same phase assemblage as its starting material, similarly to the case for the M-type samples (Table 2.2 and Figure 3.22). Another textural characteristic common in these two runs is a development of pores and reaction rim in some titanomagnetite and ilmenite grains, which are also similar to the M-type experiments (see section 3.1.3.2.1).

The median compositions of titanomagnetite are $Mt_{26}Usp_{47}Mgf_{15}Hc_7Chr_5$ for 750 °C and $Mt_{27}Usp_{43}Mgf_{20}Hc_8Chr_2$ for 790 °C run and those of ilmenite are

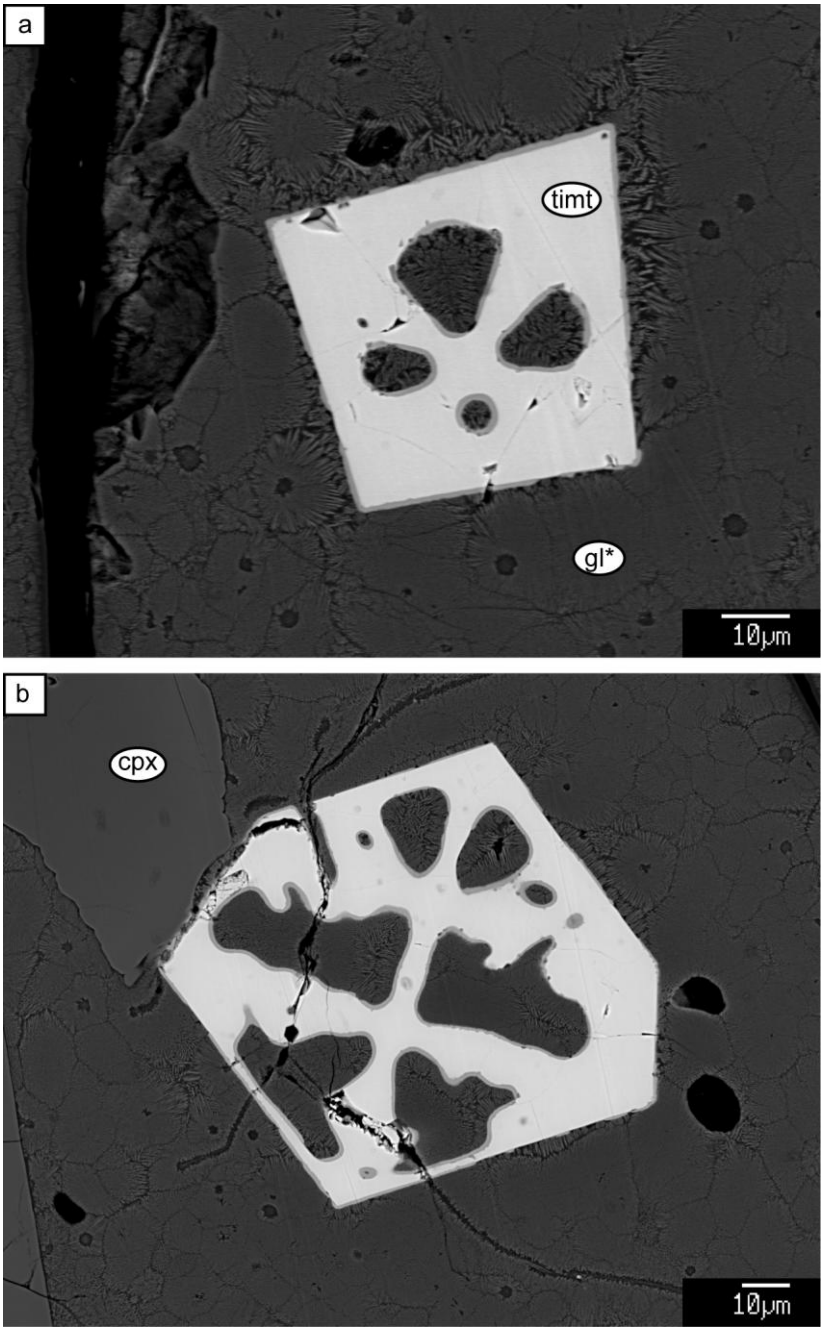

Figure 3.20. Back-scattered electron images of the non-exsolved titanomagnetites in the Group 2 M-type high-temperature annealed sample at 790 °C (MAm-E-14). The tone of the oxides may appear to be different in the images due to different brightness/contrast settings. The grains possess olivine reaction rim. Pore formation in oxide grains is more visible in the exsolved grains as in Figure 3.19. Abbreviations: gl*=devitrified glass, timt=titanomagnetite, cpx=clinopyroxene.

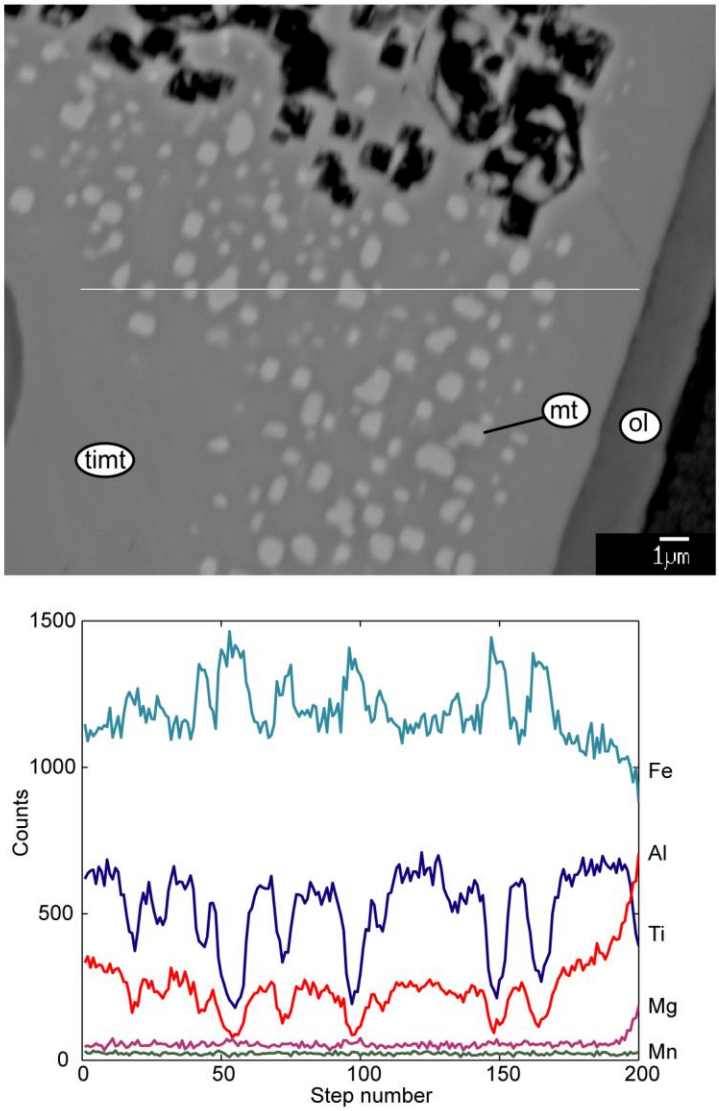

Figure 3.21. An element line scan of Type (1) exsolution (magnetite – Al-bearing titanomagnetite) in the Group 2 M-type high-temperature annealed sample at 790 °C (MAm-E-14). The line scan was taken at the horizontal line shown in the back-scattered electron image with 5 pixels x 200 steps. The co-variations of elements are clear in this datum. See text for detailed descriptions. Abbreviations: mt=magnetite, timt=titanomagnetite, ol=olivine.

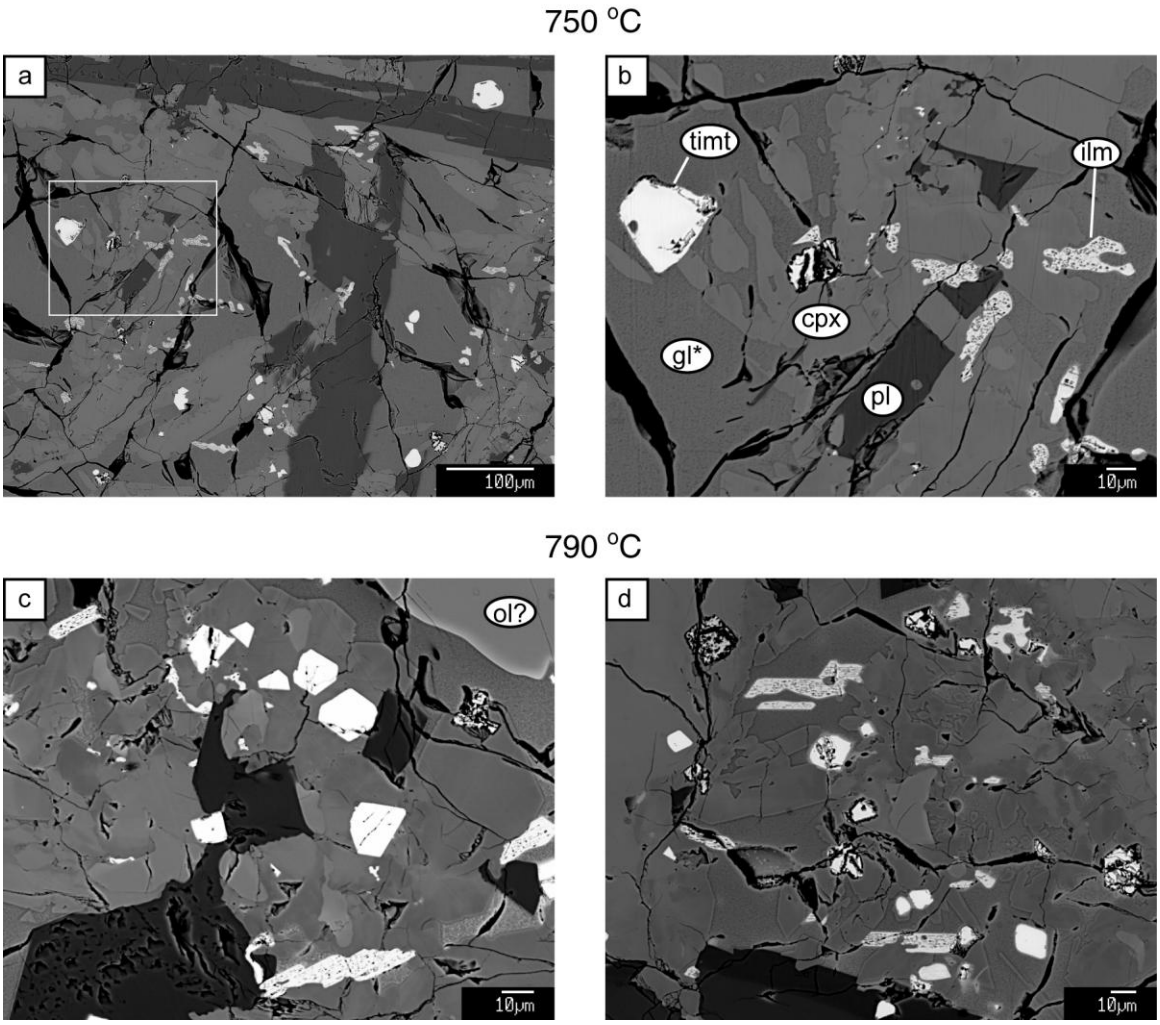

Figure 3.22. Back-scattered electron images of the Group 2 T-type high-temperature annealed samples at 750 and 790 °C (MB2-E-15 and E-14). The tone of the oxides may appear to be different in the images due to different brightness/contrast settings. Relative tone difference of titanomagnetite and ilmenite still holds within each image (titanomagnetite is lighter with respect to ilmenite). The changes for both samples are pore formation in both oxide phases and re-crystallization of glass. (b) is a region in (a) shown in a white box. In (c), pore formation in plagioclase is visible. In (d), reaction rim on some oxide grains are visible. They are most likely olivine rim. Abbreviations: cpx=clinopyroxene, pl=plagioclase, timt=titanomagnetite, ilm=ilmenite, gl*=devitrified glass, ol=olivine.

$Hem_4Ilm_{88}Gk_8$ and $Hem_8Ilm_{83}Gk_9$, respectively. These values are possibly biased because there were few analyzable grains in the samples, most likely due to extensive pore formation in the oxides. Similarly to the M-type high temperature runs, there is depletion in Mg and approach toward end-member magnetite and ilmenite that was also present in time-series runs (Figure 3.13b - c, 3.14b - c, and 3.17d).

3.2 Magnetic Properties

The magnetic properties of the Group 2 starting materials and the time-series samples were obtained by DM Cuomo and SA Brachfeld (see section 2.2.2), which will be the focus of discussion in Cuomo et al. (in prep.). Although some of their data will be mentioned here, the Group 1 and Group 2 high-temperature samples will be the focus of discussion in this thesis.

3.2.1 Curie Temperatures

The T_C values obtained from M_s-T curves (Table 3.1, Figure 3.23, Appendix N) were compared with the T_C values estimated for the oxides based on composition obtained by EPMA (Appendix O). The most reasonable and comparable T_C's were matched to decide corresponding magnetic phase to the T_C's obtained from M_s-T. Differences between T_C's from magnetic measurements and those calculated from compositions are relatively large in general. This is presumably because of uncertainties involved in both determinations. For the Group 1 M-type starting material, T_C of ~545 and 420 °C were detected and the corresponding minerals were interpreted as hematite and Fe-Mg-Al spinel oxide, respectively. The T_C values for the annealed sample were ~210, 470, and 580 °C, which were interpreted as Al-bearing titanomagnetite end-

Table 3.1. Sample bulk magnetic properties

Sample	T_f [ºC]	Duration [day]	M_s[a] [Am^2/kg]	M_{rs}[b] [Am^2/kg]	M_{rs}/M_s	B_c[c] [mT]	B_{cr}[d] [mT]	B_{cr}/B_c	T_C[e] [ºC]
Group 1									
MAm-36	1065	n.a.	1.70E+00	1.00E-01	0.06	2.90	22.44	7.74	420, 545
MAm-E-03	710	54	2.98E+00	6.64E-01	0.07	21.01	52.44	2.50	210, 470, 580
MB2-31	1070	n.a.	6.33E-01	4.72E-02	0.07	2.95	12.80	4.34	400
MB2-E-03	710	54	9.03E-01	2.92E-01	0.32	21.87	46.01	2.10	210, 400
Group 2									
MAm-51	1070	n.a.	4.30E+00	1.91E-01	0.04	2.57	9.35	3.63	n.d.
MAm-E-09	650	21	2.91E-01	1.27E-02	0.04	2.48	12.27	4.94	n.d.
MAm-E-10	650	32	2.66E+00	1.02E-01	0.04	2.09	9.40	4.50	n.d.
MAm-E-11	650	48	1.86E+00	8.80E-02	0.05	2.44	9.18	3.77	n.d.
MAm-E-12	650	111	5.00E+00	2.80E-01	0.06	3.06	9.53	3.11	n.d.
MAm-E-13	650	158	9.24E-01	4.00E-02	0.04	2.13	9.16	4.31	n.d.
MAm-E-14	790	88	5.33E-01	4.60E-02	0.09	3.85	9.94	2.58	314.3
MAm-E-15	750	88	7.76E-02	7.29E-03	0.09	3.83	12.00	3.13	297.1
MB2-48	1070	n.a.	9.52E-02	8.71E-03	0.09	2.56	8.77	3.42	n.d.
MB2-E-09	650	21	1.26E-01	1.35E-02	0.11	3.30	10.36	3.14	n.d.
MB2-E-10	650	32	3.64E-02	4.27E-03	0.12	3.86	12.11	3.14	n.d.
MB2-E-11	650	48	1.01E-01	7.37E-03	0.07	1.90	7.92	4.18	n.d.
MB2-E-12	650	111	1.80E-01	1.76E-02	0.10	3.04	8.50	2.80	n.d.
MB2-E-13	650	158	9.13E-02	8.23E-03	0.09	2.64	8.56	3.25	n.d.
MB2-E-14	790	88	2.05E-02	3.95E-03	0.19	5.26	14.96	2.84	none
MB2-E-15	750	88	3.47E-02	6.09E-03	0.18	5.75	13.81	2.40	none

[a] Saturation magnetization

[b] Saturation remanent magnetization

[c] Coercivity

[d] Coercivity of remanence

[e] Curie temperature

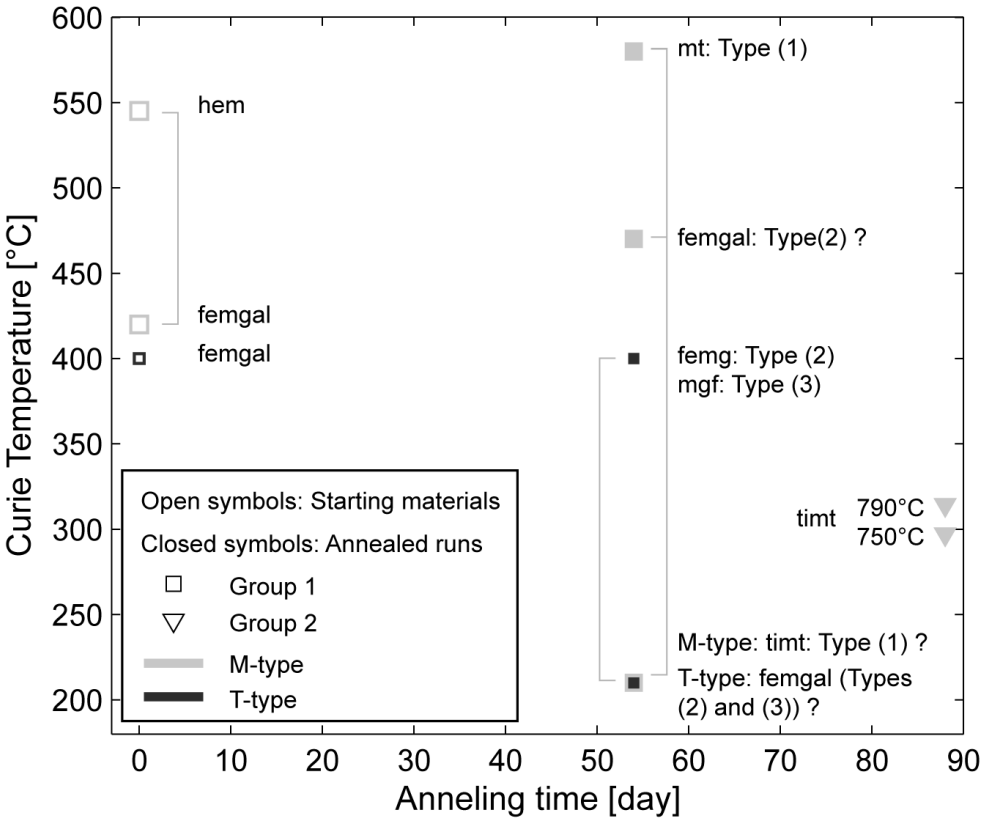

Figure 3.23. A plot of Curie temperature (T_C) vs. annealing time for the Group 1 samples (MAm-36, MB2-31, and MAm/MB2 -E-03) and Group 2 high-temperature M-type samples (MAm-E-14 and E-15). The annealing temperatures are labeled for the Group 2 samples. The T-type equivalents for Group 2 did not exhibit clear T_C, and therefore are not plotted here. See text for explanations. Phase abbreviations: hem=hematite, femgal=Fe-Mg-Al spinel oxide, mt=magnetite, femg=Fe-Mg spinel oxide, mgf=magnesioferrite, timt=titanomagnetite. (Type (1): magnetite – Al-bearing titanomagnetite, Type (2): Fe-Mg spinel oxide – Fe-Mg-Al spinel oxide, Type (3): Fe-Mg-Al spinel oxide – Al-bearing magnesioferrite)

member in Type (1) exsolution, exsolved and non-exsolved Fe-Mg-Al spinel oxide, and magnetite in Type (1) exsolution, respectively. Note that T_C at 210 °C is much lower than expected value for Type (1) titanomagnetite (316 °C) (Appendix O). As for the T-type samples, starting material had a T_C of ~400 °C which corresponds to Fe-Mg-Al spinel oxide. The annealed sample showed T_C of ~210 and 400 °C. The lower T_C could correspond to exsolved or non-exsolved Fe-Mg-Al spinel oxide whose expected T_C is the lowest among the petrologically characterized oxides in this sample (Appendix O). Although it is much lower than its expected T_C (>370 °C), if it is true, the same T_C detected for M-type sample was also contributed from Fe-Mg-Al spinel oxide, considering the absence of titanomagnetite in T-type sample. Another T_C for T-type anneal sample at 400 °C was interpreted as either Fe-Mg spinel oxide in Type (2) or Al-bearing magnesioferrite in Type (3) exsolution, or some combination of the two. For the Group 2 high temperature runs, only M-type samples had detectable T_C. The run annealed at 750 °C showed T_C at ~300 °C and the run annealed at 790 °C showed T_C at ~315°C, where both correspond to titanomagnetite. Note that the T_C's are higher than the expected for both samples (230-240 °C) (Appendix O). Although it is petrologically confirmed that the latter sample has titanomagnetite exsolution, that is, nearly pure magnetite phase, its corresponding T_C was not detected.

3.2.2 Magnetic Domain State

The Day plot (Day et al., 1977) was obtained using hysteresis parameters (Table 3.1) in order to infer a magnetic domain state of magnetic phases in the samples (Figure 3.24). A datum of a naturally exsolved titanomagnetite and that of homogenized sample from Evans et al. (2006) were plotted in the same graph as a comparison. For the Group 1

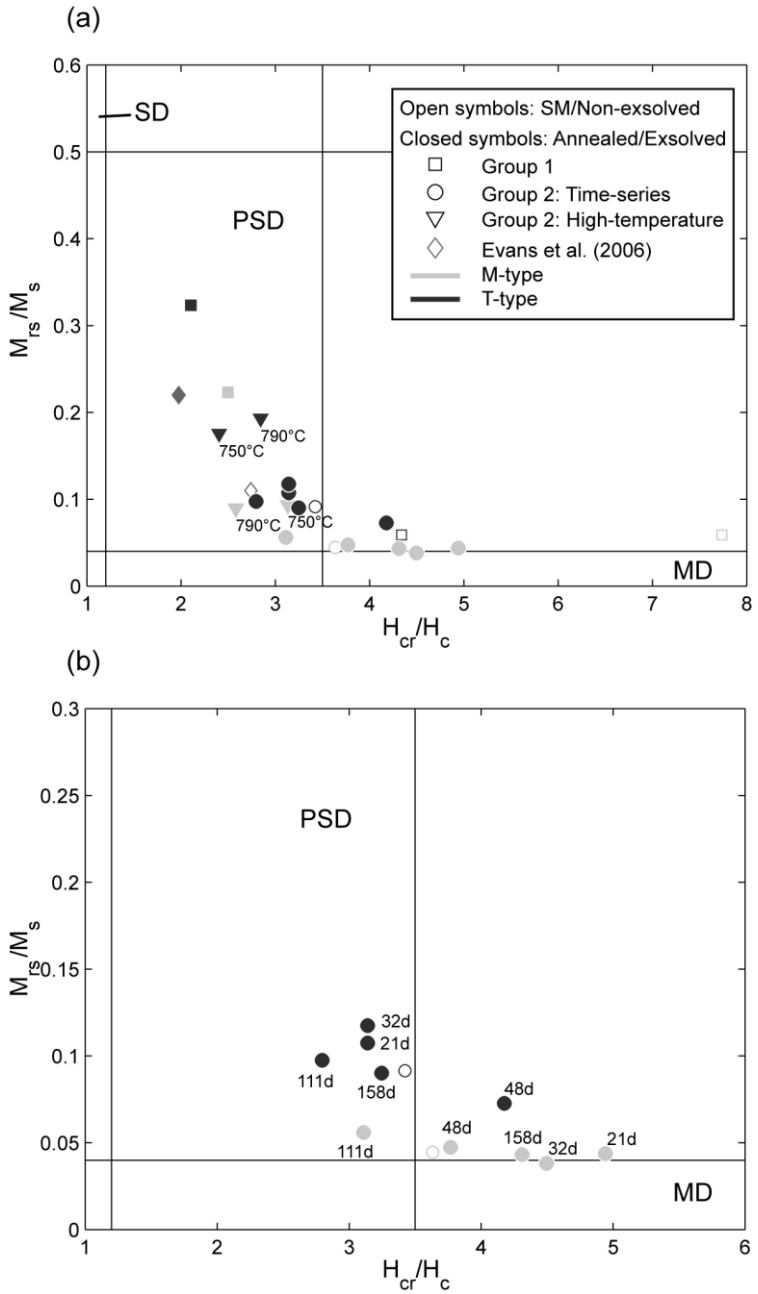

Figure 3.24. Day plots of the Group 1 samples (MAm-36, MB2-31, and MAm/MB2 -E-03) and Group 2 samples (MAm-51, MB2-48, MAm/MB2 -E-09 – E-15). (a): All the samples are shown. The natural sample with exsolved titanomagnetite and homogenized sample from Evans et al. (2006) are also shown for comparison. (b): The Group 2 time-series samples are shown with their anneal times labeled. Note that the starting material data points for the Group 2 high-temperature are the same as Group 2 time-series. The Group 1 samples and Group 2 high-temperature samples show a domain behavior shift toward single-domain field after annealing. See text for detailed descriptions. Abbreviations: M_{rs}=saturation remanence magnetization, M_s=saturation magnetization, H_{cr}=coercivity of remanence, H_c=coercivity, SD=single-domain, PSD=pseudo-SD, MD=multidomain.

samples, both M- and T-types showed an approach toward the SD field similar to that of natural example. As for the Group 2 high temperature samples, they also showed a similar behavior but to a less degree. Again, the M-type sample annealed at 790 °C did not show a significant difference in behavior here compared to the 750 °C run regardless of a presence of petrologically confirmed titanomagnetite exsolution. The time-series data did not exhibit any systematic change in domain state with respect to time, and all are further away from the SD field compared to the high-temperature annealed samples for each composition.

4. DISCUSSION

The discussion consists of three sections. In the first section, unintended experimental parameters are discussed. They are responsible for the observed difference in the modal abundance of minerals and oxide phase assemblages in the crystalline starting materials between Groups 1 and 2. In the second section, three topics of non-pure titanomagnetite exsolution are interpreted. The topics are 1) exsolution process, 2) cation partitioning pattern between the exsolution end-members, and 3) their magnetic properties. The third section describes the effect of isothermal annealing on oxide compositions seeking for a geological relevance.

4.1 Implication of the Distinct Run Products from the Two Experimental Groups

The experimental variables, pressure, temperature treatment, and fO_2, were aimed to be the same for synthesis of Groups 1 and 2 starting materials, intending to reproduce the identical starting materials as Group 1 for Group 2. Distinct crystalline starting materials obtained for T-type sample is attributed to different reagent mixture compositions (Table 2.1). However, there was also a petrologic difference in M-type starting materials although the same reagent mixture was employed. Among the experimental variables listed above, pressure and temperature treatment were almost identical for both groups (Table 2.2). Thus, distinct fO_2 in the two groups was suspected to be a cause of different outcomes and investigated. As a matter fact, the method of controlling and monitoring fO_2 was different for the two groups: QFM buffer was used for Group 1 whereas a flowing gas and a sensor were used for Group 2 (see section 2.1.1.4 and Table 2.2). Considering a presence of hematite in Group 1 starting materials

and a consistent starting material preparation method within each group, it is most likely that oxidation took place in Group 1 which is related to the fO_2 control method. Maghemitization of titanomagnetite was also reported in the experiments by Brachfeld and Hammer (2006) for the long duration QFM runs using a similar experimental settings. To test this possibility, QUILF calculation (Anderson et al., 1993) using software quilf95 was performed for M- and T-type samples for Group 1 and T-type sample for Group 2, in which there are spinel and rhombohedral oxide composition data available for the calculations (Table 4.1). The input parameters used for the quilf95 are: pressure, temperature, spinel oxide composition in terms of Ti, Mg, and Mn in the number of atoms per unit formula, and rhombohedral oxide composition in terms of molar fractions of hematite and geikielite, where the output parameter is fO_2. For the oxide compositions, median values rather than average values in each sample were employed due to heterogeneity observed in Group 2 sample (see section 3.1.1). The obtained fO_2 values for Group 1 M- and T-types are QFM + 7.284 (± 0.805) and QFM + 6.387 (± 1.204) in log unit, respectively. That of Group 2 T-type is QFM + 0.263 (± 0.333). These results clearly show an oxidized state to near hematite-magnetite (HM) buffer curve of the Group 1 starting materials as opposed to Group 2 T-type that is nearly at the aimed fO_2. Although Group 1 M-type starting material fO_2 was not examined due to a lack of rhombohedral oxide or any other mineral compositions that can be used for QUILF calculation, it is likely to be equilibrated near QFM as well considering the identical fO_2 treatments to the T-type material for the same group. Therefore, it is most likely that the distinct oxide phase assemblages in the starting materials were derived from different fO_2 in the final step of preparing crystalline starting material. Considering a confirmed

Table 4.1. QUILF calculations for the starting materials

Sample	T [°C]	P [bar]	fO_2 [log unit]	fO_2 Uncertainty [log unit]	ΔFMQ [log unit]	Spinel Oxide[a]			Rhombohedral Oxide[b]		
						NTi	NMg	NMn	Xil	XHem	XGk
MAm-36	1065	1	***-2.740***	***0.805***	***7.284***	0.04	0.69	0.07	0.03	0.88	0.09
MB2-31	1070	1	***-3.568***	***1.204***	***6.387***	0.09	0.57	0.06	0.05	0.84	0.11
MB2-48	1070	1	***-9.691***	***0.333***	***0.263***	0.46	0.26	0.04	0.64	0.15	0.21

Inputs are in regular font and outputs are in bold italic font.

[a] In terms of number of cations

[b] In terms of mol fraction of the endmember

presence of all three phases in QFM buffer in the starting material synthesis run, it raises question to the reliability of fO_2 control method. These contrasting results of Group 1 and 2 indicate that it is preferred to use gas mixture for fO_2 control if possible.

4.2 Non-Pure Titanomagnetite Exsolution

Three types of spinel oxide exsolution were observed in the course of experiments (Figure 4.1).

Type (1), magnetite – Al-bearing titanomagnetite exsolution was present in Group 1 M-type sample annealed at 710 °C for 54 days and Group 2 high temperature M-type sample annealed at 790 °C for 88 days (see sections 3.1.2.1 and 3.1.3.1.1). These samples have a common reagent mixture, but different crystalline starting material production procedures; Group 1 at ~HM and Group 2 at QFM. The precursor oxides were also different: hematite for Group 1 and titanomagnetite for Group 2. The cation partitioning pattern is Mg-Fe and Ti-Al positive correlations and a negative correlation between these pairs, where the Fe and Ti present major partitioning. The exsolved grains in the Group 1 sample are characterized by lower Ti/Fe and Al/Fe ratios and higher Mg/Fe ratio relative to the Group 2 sample.

Type (2), Fe-Mg spinel oxide – Fe-Mg-Al spinel oxide exsolution was present in Group 1 M- and T-type samples annealed at 710 °C for 54 days (see sections 3.1.2.1 and 3.1.2.2). The crystalline starting materials for these samples were prepared at ~HM. The precursor oxide phase is Fe-Mg-Al spiel oxide. The partitioning pattern is Fe-Mg and Al-Ti positive correlations and a negative correlation between these pairs, where Mg and Al present major partitioning.

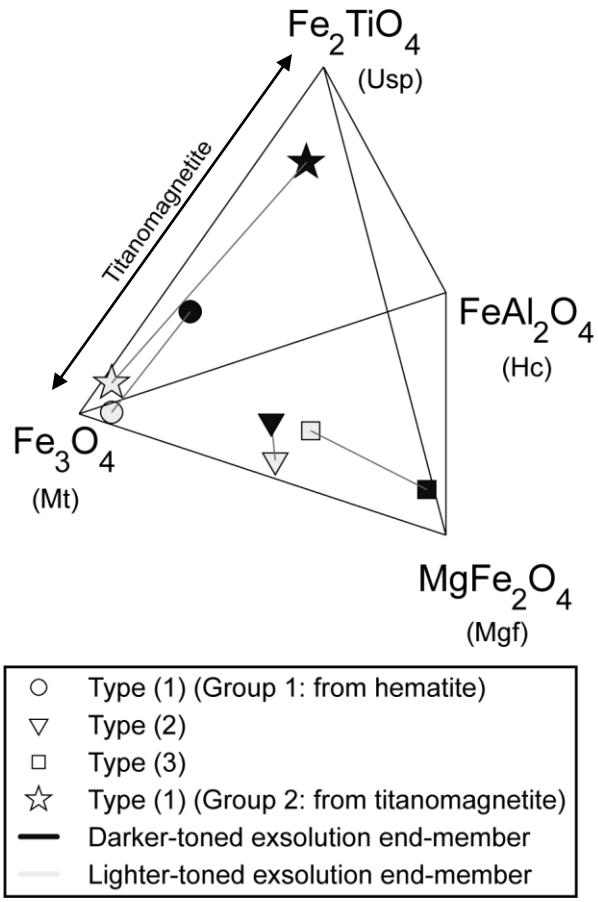

Figure 4.1. A quaternary diagram summarizing the exsolution types obtained in the Group 1 annealed samples (MAm/MB2 -E-03) and Group 2 M-type high-temperature sample annealed at 790 °C (MAm-E-14). The furthest compositions obtained are taken as end-member compositions in this diagram. The back plane (Mt-Usp-Hc ternary system) is base of prism of Figure 4.2. (Type (1): magnetite (light) – Al-bearing titanomagnetite (dark), Type (2): Fe-Mg spinel oxide (light) – Fe-Mg-Al spinel oxide (dark), Type (3): Fe-Mg-Al spinel oxide (light) – Al-bearing magnesioferrite (dark))

Type (3), Al-bearing magnesioferrite – Fe-Mg-Al spinel oxide exsolution was present in Group 1 T-type sample annealed at 710 °C for 54 days that was mentioned in Type (2) exsolution above (see section 3.1.2.2). The precursor oxide phase is Fe-Mg-Al spiel oxide as well. The partitioning pattern is an Al-Ti-Fe positive correlation and a negative correlation between these elements and Mg, where Mg and Al present major partitioning.

Amongst these, only Type (1) could be called titanomagnetite exsolution, considering the host oxide composition to be near titanomagnetite solid solution series regardless of impurity (mainly Al) and major element partitioning is involving Fe and Ti. This type of exsolution will be discussed below.

4.2.1 Implications for Exsolution Mechanisms

Exsolution mechanisms are best inferred from textural observation by means of TEM (see section 1). In our study, TEM was not planned to be used, as it was anticipated to detect magnetically the onset of exsolution and determine the exsolution mechanisms particularly by tracking change of T_C in the time-series experiment. Nucleation and spinodal composition have both been suggested as the exsolution mechanism of titanomagnetite (Harrison and Putnis, 1999). The nucleation produces discrete precipitates (in this case, magnetite) whereas the spinodal decomposition produces compositional modulation large in extent but small in degree (Gibbs, 1961). Therefore, if the titanomagnetite exsolution had taken place in our time-series experiment, and if nucleation had been the exsolution mechanism, we could have expected the appearance of magnetite Curie temperature and its presence for the rest of the runs with progressing exsolution. This would be similar to but opposite of the Ms vs. temperature curve

behavior observed by Vincent et al. (1957). They homogenized naturally exsolved titanomagnetite grains by annealing, where magnetite gradually dissolved into ulvöspinel-rich component, thus, magnetite Curie temperature was detected until magnetite lamella were dissolved up to their cores. On the other hand, if spinodal decomposition takes place, gradual segregation of Curie temperature from the initial titanomagnetite would be observed because of the small compositional difference between two newly developing phases. Unfortunately, in our time-series experiment at 650 °C, no exsolution was observed even for the longest duration run (158 days) neither compositionally nor magnetically (see section 3.1.3.1). Also, there was a possibility that the concentration of oxide phase was too low to precisely detect Curie temperature particularly for subtle extent of exsolution texture. As a matter of fact, the previous experiments on titanomagnetite exsolution were performed on extracted titanomagnetite grains (see section 1).

Fortunately, we are able to examine two cases of titanomagnetite exsolution: one in Group 1 M-type run and another in Group 2 high temperature run at 790 °C (see sections 3.1.2.1 and 3.1.3.2.1). For both cases, the exsolution texture had progressed beyond incipient stage, which prevents us from examining the exsolution mechanism (Yund and McCallister, 1970; Price, 1980). However, as the group 2 sample has its titanomagnetite texture aligned along certain crystallographic orientation, it seems to have obtained conventional titanomagnetite exsolution seen in naturally exsolved titanomagnetite (Evans and Wayman, 1974; Vincent et al., 1957; Price, 1981; Feinberg, 2006). This feature indicates the mechanism is likely to be either homogeneous nucleation or spinodal decomposition but not heterogeneous nucleation (see section

3.1.3.2.1.1). As for the Group 1 sample, the lamellar growth of two unmixed phases could be interpreted as an extensive growth of the exsolution texture preferred by minimization of strain energy (Price, 1980). However, we observed that the pores in the exsolved titanomagnetite grains in Group 1 sample have the same preferred orientation as the exsolution lamella; this fact indicates that the exsolution texture was controlled by crystal structure of the host titanomagnetite since the onset. In fact, the titanomagnetite exsolution in the Group 1 sample was not the conventional type: it was derived from hematite (see section 3.1.2.1). Considering the consistent crystallographic relationship between parental hematite and magnetite derived by phase transformation under reducing condition (Bernal et al., 1957), the preferred sheet-like planes are probably relic from the parent hematite grains in Group 1. It is also known that transformation of hematite to magnetite progresses in a lamellar fashion in slightly reducing gas (e.g., at 700 °C, -logPO_2 = ~11-17) (Swann and Tighe, 1977; Hayes and Grieveson, 1981; Et-Tabirou et al., 1988). Furthermore, if the path from parental hematite to exsolved titanomagnetite would be the oxide structural transformation followed by titanomagnetite exsolution, it might have had defect interfaces between those lamellae, which might have facilitated heterogeneous nucleation and therefore the exsolution rate would have been faster. Another possible process in which titanohematite (hematite-ilmenite solid solution) exsolution occurred then followed by reduction of the unmixed phases is denied by a low consolute solvus of titanohematite solid solution (<<500 °C according to Burton (1991) and >500 °C according to Harrison (2006) for titanohematite with low ilmenite fraction) and by opposite minor element (Al and Mg) partitioning pattern in titanohematite exsolution to our sample (see section 4.2.3) (McEnroe et al., 2007).

4.2.2 Inferences from Minor Element Partitioning Pattern and Three-Component Solvus

Regardless of a possible fundamental difference in Type (1) exsolution in the two samples mentioned above, they exhibit the same impurity partitioning behavior between exsolved phases. Al partitions into titanomagnetite phase and Mg goes into magnetite (see sections 3.1.2.1.2 and 3.1.3.1.1.2). Also, the partitioning of Al appears to be prominent compared to Mg in both cases.

The observed cation partitioning pattern indicates that magnetite formed due to titanomagnetite exsolution can be potentially a good magnetic remanence recorder. Magnetite and magnesioferrite are the only ferrimagnetic (more simply, magnetic) spinel oxides amongst the five spinel oxides (magnetite, ulvöspinel, magnesioferrite, hercynite, and chromite) employed to represent the compositions of titanomagnetite in the samples (Deer et al., 1962). The M_s of magnetite is 90-92 Am^2/kg, the magnesioferrite M_s is 21 Am^2/kg, and 0 Am^2/kg for ulvöspinel and hercynite (Hunt et al., 1995). Thus, partitioning of Mg rather than Al into magnetite-rich end-member minimizes a suppression of saturation magnetization.

The presence of Type (1) exsolution in samples annealed at 710 and 790 °C supports our hypothesis of a rise of consolute temperature of titanomagnetite solid solution as a result of Al inclusion. Considering a minor amount of Mg in Type (1) exsolution system (≤0.1 Mg in atoms per formula unit), we can construct tie-lines of a solvus of non-pure titanomagnetite in terms of three end-member spinel oxides, namely magnetite, ulvöspinel, and hercynite, with respect to temperature (Figure 4.2). The end-member phase compositions ($Mt_{88}Usp_9Z_3$ and $Mt_{15}Usp_{69}Hc_{12}Z_4$) are close to the pure

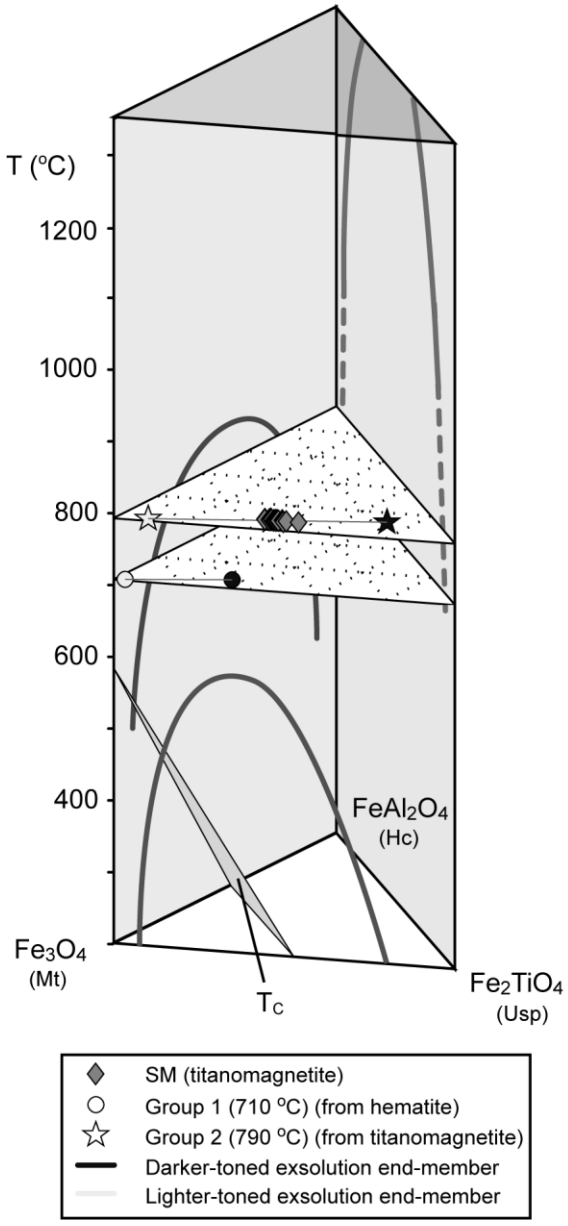

Figure 4.2. A phase diagram showing Type (1) exsolution (magnetite – Al-bearing titanomagnetite) in the Group 1 M-type annealed sample at 710 °C (MAm-E-03) and Group 2 M-type high-temperature sample at 790 °C (MAm-E-14). In this ternary system, magnesioferrite ($MgFe_2O_4$) component is ignored. The solvi of three binary solid solutions from literature drawn in the diagram are magnetite-ulvöspinel (Lindsley, 1981), magnetite-hercynite (Turnock and Eugster, 1962), and ulvöspinel-hercynite (Muan et al., 1972). For hercynite-ulvöspinel solid solution, the solvus was extrapolated (dashed line) for lower temperature. Curie temperature (T_C) is also shown.

end-member magnetite and ulvöspinel compositions for the tie-line from the Group 2 sample annealed at 790 °C. The disparity in these end-member compositions could be even larger because of possible mixed microprobe analyses of the end-member phases. This implies that the consolute temperature of the solvus for a solid solution with these end-member compositions could be much higher than 790 °C, assuming the solvus has a simple hoop shape similarly to other binary spinel oxide solid solutions. Therefore, the consolute temperature for this solid solution is much higher than the pure titanomagnetite solid solution whose consolute temperature is below 600 °C. It indicates that inclusion of Al raises the consolute temperature because Al is the major element other than Fe and Ti in this solid solution. A narrower disparity between two end-member compositions ($Mt_{90}Mgf_7Z_3$ and $Mt_{60}Usp_{29}Hc_6Z_5$) for Group 1 can be attributed to an incomplete exsolution. Similarly to Group 1, mixed electron microprobe analyses of the end-member phases could also contribute to this feature.

Al partitioning into ulvöspinel-rich titanomagnetite phase could seem to be contradicting with a presence of a solid solution between ulvöspinel and hercynite (Muan et al., 1972) (Figure 4.2). In the case of this sample, the ratio of ulvöspinel to hercynite is very high. The solvus of ulvöspinel-hercynite system is nearly symmetrical with a very high consolute temperature (Muan et al., 1972). Therefore, the degree of supersaturation was most likely small. As a result, the rate of exsolution could have been too slow. It is also possible that the composition was slightly above the solvus because the low temperature regime of the solvus is not well-constrained.

Another question arises from the series of exsolution experiments is an absence of exsolved titanomagnetite in the Group 2 M-type sample annealed at 750 °C. This anneal

temperature is between 710 and 790 °C at which the exsolution experiments achieved Type (1) exsolution in Groups 1 and 2, respectively. It could be because the onset of exsolution is not the same for all the grains in the sample. In the Group 2 sample at 790 °C, only 3 out of ~15 grains (including those appear to be fragments in two-dimension) present in a thin section showed optically observable growth of exsolution. An inferred compositional heterogeneity of titanomagnetites within sample could have an effect on the onset of the exsolution (see section 3.1.1). It is also possible that the different mechanism of Type (1) exsolution in Group 1 M-type sample was a faster process than of Group 2. If the lamellar growth of titanomagnetite as a result of reduction of hematite allowed heterogeneous nucleation, it may explain the faster Type (1) exsolution rate in Group 1. An absence of the titanomagnetite exsolution in M-type time-series experiments is most likely due to slower kinetics at lower temperature (650 °C). This is plausible considering the absence of Type (1) exsolution in the Group 2 sample annealed at 750 °C.

4.2.3 Implications of the Bulk Magnetic Properties

The Curie temperature is shown in the three-component T-X diagram in Figure 4.2 (Merrill and McElhinny, 1983; Golla-Schindler et al., 2005). Exsolved magnetite-rich end-member is capable of acquiring TRM, the major Natural Remanent Magnetization (NRM) for igneous rocks. However, as far as we can infer from the available bulk magnetic data, magnetite derived from titanomagnetite exsolution does not seem to play a major role in magnetic mineralogy of samples with exsolved titanomagnetite. The bulk magnetic data of Group 1 sample with titanomagnetite exsolution shows a presence of magnetite in M_s-T curve, providing T_C of ~560 °C (Figure 3.23 and Appendix N).

However, this carries a small fraction of the saturation magnetization compared to other phases present from other exsolved grains of Type (2) Mg-Al-rich exsolution (see section 3.1.2.1). In the Group 2 sample with titanomagnetite exsolution, only one T_C of ~314 °C that corresponds to non-exsolved titanomagnetite was detected (Figure 3.23). This could be because of a minor amount of exsolved titanomagnetite grains (3 out of ~15 titanomagnetite grains). The scarcity of petrographically perceivable Type (1) exsolution in this sample is contrasting with the Group 1 sample in which almost all the titanomagnetite grains (>15 grains) in a thin section were exsolved.

An approach toward SD regime was observed for both Groups 1 and 2 samples with exsolved spinel oxides. Its degree was large for Group 1 compared to Group 2 (Figure 3.24). This change in magnetic domain size could be interpreted as a result of spinel oxide exsolution in Group 1. The trend is comparable to the difference between naturally exsolved titanomagnetite sample and homogenized titanomagnetite in Evans et al. (2006) (Figure 3.24). In the Group 2 sample, a decrease in volume and a structural change of the oxides caused by the pore formation may be contributing to a change in domain behavior. This is also true for the oxide grains that have or would have had Type (1) and (3) exsolutions in Group 1 annealed samples. This porous texture of oxide grains was observed for all high-temperature series samples including T-type (see section 3.1.3.2). The shift in the bulk magnetic domain size toward SD field was also present in all the samples. However, such a texture does not seem to have been reported in natural or experimental samples and an effect on magnetic properties should be fully investigated to prove this hypothesis. The observed change in the bulk magnetic domain state could also be due to combined contributions from an exsolved magnetite phase that is closer to

SD-PSD field and non-exsolved MD titanomagnetite grains in Group 2 (Dunlop, 2002). However, T_C for magnetite was not detected in M_s vs. temperature measurement in the M-type 790 °C. Also, similar behavior was observed for other high temperature samples including T-type without exsolved titanomagnetite. Therefore, it is likely that a contribution of titanomagnetite in Group 2 sample to the bulk magnetic property is minimal.

4.3 Nature of the Subsolidus Re-Equilibration and its Implications

The experimental Group 2 consists of five isothermal time-series experiments and high-temperature experiments at two different temperatures for two compositions, M- and T-types. General effects of time and temperature on oxide phases deduced from the Group 2 experimental results are briefly noted in this section.

A major change of the oxide compositions in Group 2 annealed samples was MgO depletion for M- and T-types (Figures 3.14, 3.15, and 3.17). A slight depletion in TiO_2 was also observed in M-type samples (Figures 3.14 and 3.15). Considering the pore formation and a consequent volume decrease, the oxide phases must be losing ions under annealing, especially Mg. This makes MgO wt.% in post-anneal oxides less than the initial values. These changes are most likely due to compositional re-equilibration of oxides in contact with other phases. Equilibrium phase assemblage including co-existing oxide phases is sensitive to temperature and oxygen fugacity (Frost et al., 1988). Therefore, it is not very surprising that our crystalline starting materials equilibrated and quenched at high temperature (1070 °C) would undergo phase and/or compositional re-equilibration upon annealing at lower temperatures (650-790 °C). Depletion of Mg in

oxide phases and their approach toward pure end-member oxide composition in our annealed samples (Figures 3.13, 3.14, 3.15, and 3.17) are supported by geological analogues. Intrusive rocks are known to have oxides with little impurity due to continuous re-equilibration under cooling, where the oxide phases tend to lose Mg. This is true except the intrusive body is ore (Frost and Lindsley, 1991). Similarly, oxide phases in metamorphosed rocks hardly have any impurities (Frost, 1991).

Along with the morphology change of oxides due to pore formation, this kind of effect on intrusive rocks under prolonged annealing or slow cooling might be worth to be taken into consideration for future experimental works.

5. SUMMARY

Isothermal annealing experiments aimed to attain titanomagnetite exsolution were conducted previously by Bowles and Hammer using two purported Martian crustal compositions: M-type and T-type (Group 1 pilot experiments). Their preliminary report identified oxide exsolution in the samples, but did not include quantitative analysis of phase compositions. The samples were further analyzed herein to study titanomagnetite exsolution in detail. The pilot samples are compared with follow-up samples from subsequent time-series and high-temperature exsolution experiments (Group 2 experiments). The goals of the study were (a) to infer the mechanism of the titanomagnetite exsolution from time-series experiments, and (b) determine the temperature-controlled kinetics of the exsolution process

The Group 1 and 2 experiments produced differences in the oxide phase assemblages between starting and annealed materials. The oxide phases in the Group 1 starting materials were hematite and Fe-Mg-Al spinel oxides for both M- and T-types. Titanomagnetite was the only oxide phase in the Group 2 M-type starting material whereas T-type samples contained ilmenite in addition to titanomagnetite. The difference in the two groups likely resulted from the more oxidizing conditions (near HM buffer curve as opposed to QFM) imposed on the starting material production in Group 1, in addition to distinct reagent mixture compositions for the T-type samples.

The oxide compositional analyses showed that the two groups of annealing experiments gained three different types of exsolution in total: (1) magnetite – Al-bearing titanomagnetite, (2) Fe-Mg spinel oxide – Fe-Mg-Al spinel oxide, and (3) Fe-Mg-Al spinel oxide – Al-bearing magnesioferrite. The Type (1) exsolution was observed in the

Group 1 M-type sample (MAm-E-03) and Group 2 M-type high-temperature run at 790 °C (MAm-E-14). Type (2) was present in the Group 1 M- and T-type samples (MAm/MB2 -E-03). Type (3) was present in the Group 1 T-type sample (MB2-E-03). Changes in bulk magnetic properties were observed in the Group 1 annealed samples. A change in magnetic mineralogy was inferred from the T_C. Also, the approach toward SD behavior in the experimental samples is consistent with an exsolution process as shown by the progression *away* from SD behavior observed in natural, exsolved materials undergoing homogenization. In contrast, no change was detected for the Group 2 sample after the anneal treatment. It is impossible to distinguish between two possibilities: (1) exsolution did not occur in this sample, or (2) exsolution did occur but produced quantities of magnetite that were too small to detect magnetically and too sparse to observe with electron microscopy. Exsolution was not detected in any of the time-series samples and most of the high-temperature samples, although these materials exhibited pronounced Mg exchange with the surrounding glass matrix.

Differing exsolution, distinct exsolution textures between Groups 1 and 2 and different parental oxide phases (hematite in Group 1 and titanomagnetite in Group 2) suggest different reaction mechanisms for achieving Type (1) non-pure titanomagnetite exsolution. However, the two groups of samples share compositional characteristics: Al is partitioned with Ti into the titanomagnetite phase and Mg is partitioned into magnetite. An additional observation with important implications is that the consolute temperature rises dramatically with addition of Al to the titanomagnetite solid solution. Higher exsolution temperature implies that magnetite formed during exsolution of non-pure titanomagnetite is capable of attaining TRM in a wider range of temperatures than is pure

titanomagnetite. Considering that the starting material for the Group 2 M-type samples was identical, the absence of exsolution in the time-series samples suggests the exsolution rate was too slow at the temperature (650 °C). Absence of detectable exsolution within the sample run at 750 °C is tentatively attributed to the small volume of exsolved magnetite rather than its total absence; exsolved magnetite is minimally detectable in the

did not have sign of titanomagnetite exsolution. However, considering its temperature with respect to other runs that showed exsolution (710 and 790 °C), it could also have attained the exsolution as well. It is possible that the exsolution actually took place but was not observed in the thin section or bulk magnetic measurements because of its scarcity inferred from the Group 2 M-type sample annealed at 790 °C.

The samples from Group 2 exhibited a subsolidus re-equilibration mainly characterized by a decrease in Mg in oxide phases, and secondarily a slight decrease in Ti for M-type samples. As a result, the titanomagnetite and ilmenite approached end-member magnetite and ilmenite compositions, respectively. A similar trend is observed in natural rocks undergoing slow-cooling or reheating (metamorphism).

Despite methodological shortfalls, the study produced observations worthy of continued study, including (a) Fe-Ti-Al-Mg oxide exsolution occuring on laboratory time scales, (b) new tie-lines defining the Al-bearing titanomagnetite solvus, and (c) cation exchange between oxides and other phases.

6. FOR FUTURE WORK

Unintended differences in the phase assemblages and oxide compositions of the starting materials used in successively run experiments caused profound differences in the mineralogies and magnetic characteristics of run products. Furthermore, non-isolated experimental variables compromise unique interpretation of some observations. Based also on our observations and interpretations summarized above, we suggest the following for future experiments on titanomagnetite exsolution:

(1) The reagent mixtures (using fused beads) and the crystalline starting materials must be proven identical for different experimental groups by quantitative compositional analysis, such as EPMA, prior to annealing treatment.

(2) The time-series experiments should be reproduced for M-type composition at the QFM buffer curve and higher temperatures, 790 °C for example, as we showed that 88 days of annealing under these conditions produces titanomagnetite exsolution observable by electron microprobe.

(3) Simpler experiment should be designed to isolate and analyze the uncertain effects of the subsolidus re-equilibration. For instance, we could consider an annealing experiment on a synthetic single crystal of titanomagnetite with a composition that is known to attain exsolution based on the experiment introduced here. This could avoid a cation exchange from oxide phase to other phases.

(4) A technique such as X-ray diffraction can be employed to more precisely characterize the titanomagnetite exsolution with time.

PART II

RAMAN SPECTROSCOPY OF THE TITANOMAGNETITES

Lisa Tatsumi-Petrochilos[1], Pavel Zinin[2], Lydie Bonal[2], Julia Hammer[1],
Stuart Gilder[3], and Mike Fuller[2]

[1] Department of Geology and Geophysics, University of Hawai‘i, 1680 East West Road, Honolulu, Hawai‘i 96822, USA
[2] Hawai‘i Institute of Geophysics and Planetology, 1680 East West Road, Honolulu, Hawai‘i 96822, USA
[3] Department of Earth and Environmental Sciences - Geophysics, Munich University, Theresienstr. 41/IV, Munich 80333, Germany

Abstract

A systematic study of the Raman spectra of the titanomagnetite solid solution series ($Fe_{3-x}Ti_xO_4$) for x = ~ 0.0, 0.2, 0.4, and 0.6 has been conducted. The samples showed combinations of five previously predicted Raman peaks at ~190, 310, 460, 540, and 670 cm^{-1}, which correspond to vibrational modes with following symmetry assignments: $T_{2g}(1)$, E_g, $T_{2g}(3)$, $T_{2g}(2)$, and A_{1g}, respectively. Magnetite is missing the $T_{2g}(3)$ mode, consistent with previous studies. The shape of the Raman spectrum changes as Ti concentration increases. The characterization of the shape change was conducted by comparing measured intensities of the peaks relative to that of the A_{1g} peak. The most prominent feature is an appearance and an increase in relative intensity of a $T_{2g}(3)$ peak above x = ~0.2. On the contrary, the Raman peak for the $T_{2g}(2)$ mode gradually diminishes as Ti increases and nearly disappears at x = ~0.6.

Introduction

The minerals within the titanomagnetite solid solution series serve as important carriers of the paleomagnetic record. Curie points are commonly used to determine the composition of these magnetic phases (Akimoto, 1962). However, Curie points generally reflect bulk rock properties and do not provide insight for individual grains or intra-grain compositional variation in a sample. Moreover, Curie point measurements carried out at elevated temperatures may alter the original material and obliterate the information one seeks. Determination of the composition of individual Fe-Ti oxide grains can also be made with electron microprobe techniques, but Raman spectroscopy may prove a useful additional technique as it yields chemical as well as structural information.

Raman spectroscopy can also contribute to resolving various questions in the field of planetary research (e.g., Popp and Schmitt, 2004). It can be used, for example, to analyze the mineral composition of planetary surfaces in order to understand the evolution of a planet (Sharma, 2007). Titanomagnetites occur as minor phases within meteorites and Raman spectroscopy has been used to identify them (Wang et al., 2004a; Wang et al., 2004b).

Raman spectra are available for the end-members of the titanomagnetite solid solution, magnetite (Degiorgi et al., 1987; Gasparov et al., 2000; Shebanova and Lazor, 2003a; Verble, 1974) and ulvöspinel, and for some intermediate Ti compositions (Wang et al., 2004b). However, a systematic study of the changes of the line positions and their relative intensities as Ti is substituted into magnetite does not appear to have been reported.

We present results for the composition parameter x, defined by ($Fe_{3-x}Ti_xO_4$), with x = ~ 0.0, 0.2, 0.4, and 0.6, namely, TM0, TM20, TM40, and TM60. The results from our systematic study were used to quantify the Ti content variations within and between titanomagnetite grains in a melatroctolite sample from Cumberland, Rhode Island.

Samples and Methods

Natural magnetite from the Mt. Givens pluton (California) was used for TM0. The unit-cell constant determined by X-ray powder diffraction has the value a = 8.3945(11) Å, which is in a good agreement with published data for natural Fe_3O_4 (a = 8.3941(7) Å). Other samples, TM20, TM40, and TM60, were prepared using the floating zone technique (Wanamaker and Moskowitz, 1994). The Ti concentrations were verified by

thermomagnetic analysis (Gilder and Le Goff, 2008) as well as electron probe microanalysis (EPMA). The chemical compositions obtained from EPMA are presented in Table 1, except for the natural magnetite whose size was too small to prepare a grain mount for EPMA.

A grain less than 20 mg was selected for each of the four TM samples with different Ti concentrations to obtain the Raman spectra. The samples were mounted on a carbon tape attached to a glass slide. Raman spectra were collected for each sample using a WiTec Alpha300R confocal Raman microscope with a Nd-YAG green (532 nm) laser (Coherent Compass, Dieburg, Germany). The power of the laser beam at the sample surface was kept below 0.7 mW to avoid sample damage (de Faria et al., 1997). Spectra were recorded at ~4 cm^{-1} step intervals. The calibration of the spectrometer was verified by acquiring the Raman spectra of a standard silicon wafer. Twelve to sixteen spectra per sample were analyzed with integration time of 30 s (3x10 s). An average spectrum of 12-16 spectra was obtained for each sample. We subtracted the interfering signal and corrected for background aberrations using the Grams software package (Thermo Fisher Scientific Inc.). Sixth order polynomials were used for background correction. Peaks were fitted using Mixed Gaussian and Lorentzian peak function.

Results

Raman spectra of TM0, TM20, TM40, and TM60 after background corrections are illustrated in Figure 1. Table 2 lists the major peak positions of these samples and for magnetite and ulvöspinel from published works (Shebanova and Lazor, 2003b; Wang et al., 2004b). The five previously reported Raman peaks for spinel structure at ~190, 310,

Table 1. Average compositions of TM samples as determined by electron probe microanalysis.

	TM20	TM40	TM60
TiO_2	6.16	14.02	22.53
Fe_2O_3	56.84	41.57	25.84
FeO	35.83	43.02	51.32
Total	98.83	98.61	99.69
Number of cations on the bases of 4 oxygen atoms			
Ti	0.18	0.41	0.64
Fe^{3+}	1.66	1.21	0.74
Fe^{2+}	1.16	1.39	1.62

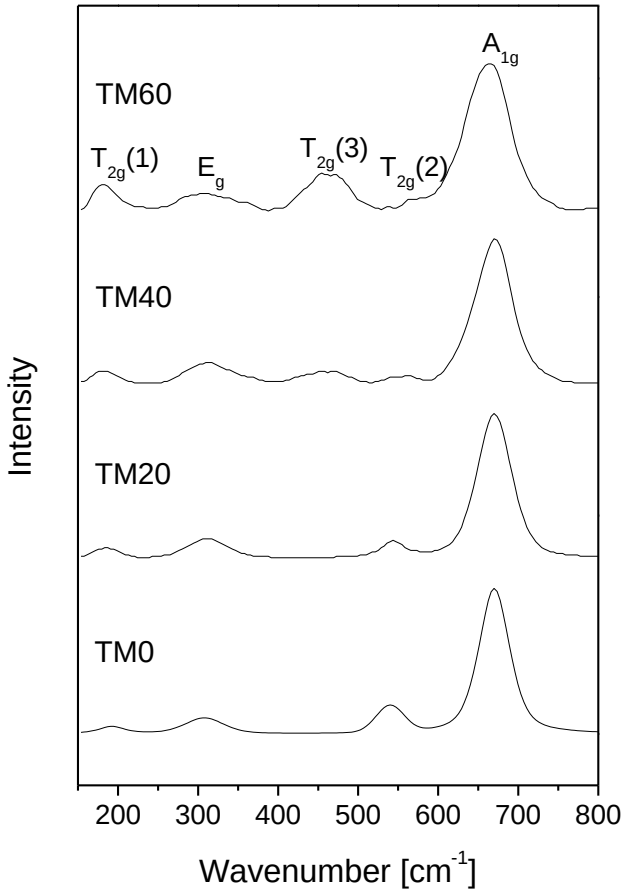

Figure 1. The average Raman spectra for each TM sample after background correction.

Table 2. Raman mode frequencies [cm^{-1}] of TM samples in this study and other studies, and titanomagnetite in melatroctolite sample (the position names A-D correspond to Figure 3).

sample	$T_{2g}(1)$	E_g	$T_{2g}(3)$	$T_{2g}(2)$	A_{1g}
TM100[a]			495	561	679
TM60	184	311	461	569	662
TM40	183	314	457	554	669
TM20	185	312		544	670
TM0[b]	192	308		540	670
TM0[c]	193	306		538	668
A	184	292	476		669
B	182	323	469		666
C	183	320	462		667
D	182	324	452		673

[a] Wang et al. (2004b)

[b] this study

[c] Shebanova and Lazor (2003a)

460, 540, and 670 cm^{-1} were observed for TM40, and discernible for TM60. These Raman shifts correspond to symmetry assignments $T_{2g}(1)$, E_g, $T_{2g}(3)$, $T_{2g}(2)$, and A_{1g}, respectively (Shebanova and Lazor, 2003b). The absence of a $T_{2g}(3)$ mode at ~460 cm^{-1} in TM0 is consistent with previous studies. A slight (~2%) shift toward higher frequency was discernible for $T_{2g}(2)$ (540-552 cm^{-1}) with increasing Ti concentration. However, the change lies within experimental uncertainty, where for instance, de Faria et al. (1997) reported 533.6 cm^{-1} for $T_{2g}(2)$ whereas Graves et al. (1988) reported 570 cm^{-1}. Therefore, it remains unclear whether this position shift is characteristic of Ti concentration.

On the other hand, it is evident from Figure 1 that the relative intensities of the Raman peaks are a good indicator of the Ti concentration. After background correction, areas under the various Raman peaks were normalized by that of A_{1g} at ~670 cm^{-1}. The A_{1g} peak was chosen as the normalization factor because it was consistently the strongest peak for all samples and there was no discernible shift with Ti concentration change. Figure 2 illustrates the behavior of the relative intensities as a function of Ti concentration. The error bars are the average standard deviations of the normalized intensity within the range of full width at half maximum of each Raman peak for the obtained spectra. The most remarkable feature was the appearance of the $T_{2g}(3)$ peak centered at 457 cm^{-1} for TM40, which was absent for TM0 and TM20. The relative intensity of this peak increases sharply from TM40 to TM60. The $T_{2g}(2)$ peak centered at ~550 cm^{-1} in TM0, TM20, and TM40 gradually decreases as Ti concentration increases, and appears to vanish at TM60. A less prominent gradual increase in relative intensity was observed in the $T_{2g}(1)$ mode at ~190 cm^{-1}. There was no noteworthy systematic dependence in intensity or peak position shift for the E_g peak at ~310 cm^{-1}.

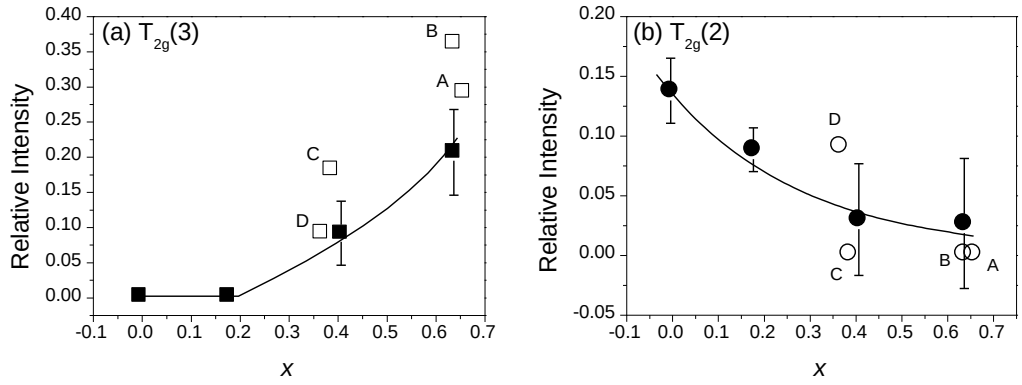

Figure 2. Plots of relative intensities vs. parameter *x* (obtained by electron probe microanalysis) for TM and the melatroctolite sample. (a) $T_{2g}(3)$, (b) $T_{2g}(2)$. Closed (Open) symbols are TM (melatroctolite). The curves are equation (1) and (2) for (a) and (b), respectively.

Discussion

A symmetry analysis and an assignment of magnetite phonon modes based on the spinel structure was made by Degiorgi et al. (1987), Gasparov et al. (2000), and Verble (1974). The theoretical analysis based on the factor-group approach predicts five Raman-active bands: A_{1g}, E_g, and three T_{2g} (White and DeAngelis, 1967). At ambient conditions, the non-polarized spectrum of magnetite shows four out of the five theoretically predicted phonon bands at 193, 306, 538, and 668 cm^{-1} (Shebanova and Lazor, 2003b). The Raman spectrum of our TM0 also contains the predicted A_{1g}, E_g, $T_{2g}(1)$, and $T_{2g}(2)$ modes at 670 cm^{-1}, 308 cm^{-1}, 192 cm^{-1}, and 540 cm^{-1}. The mode $T_{2g}(1)$ at 192 cm^{-1} is weak and was only reported in the works of Gasparov et al. (2000) and Shebanova and Lazor (2003b).

The titanomagnetite series has a general formula $A[B_2]O_4$, where A and B sites represent tetrahedral and octahedral sites, respectively. The Raman bands for the spinel structure were associated with the normal mode motions of 4 oxygen anions in each A site tetrahedron by Verble (1974), while Wang et al. (2004b) suggested that the main contribution arises from octahedral B sites. For the case of magnetite, the Fe^{3+} ion occupies A sites, while Fe^{2+} and Fe^{3+} ions occupy B sites (Stacey and Banerjee, 1974). As Ti substitution in magnetite proceeds, Ti^{4+} ions enter B sites (Blasse, 1964). Several models have been proposed for cation distribution in the titanomagnetite solid solution series, particularly regarding Fe^{2+} and Fe^{3+} ions. One model suggests that Fe^{2+} ions first enter B sites with increasing Ti content and start to enter A sites at x = ~0.2 (Kakol et al., 1991). The electron hopping between Fe^{2+} and Fe^{3+} ions in B sites in magnetite causes a polaron conduction at room temperature (Verwey et al., 1947). It decreases as Ti substitution increases, where the Jahn-Teller distortion occurs as a result of Fe^{2+}

occupancy in A sites above x = ~0.2 (Kakol et al., 1991). These changes in cation occupancy with increasing Ti concentration affects magnetic and electrical properties of titanomagnetite (O'Reilly, 1984), which are probably responsible for the observed changes in the Raman spectra. Thus, it is possible that the $T_{2g}(2)$ modes are linked to the incorporation of Fe^{2+} in tetrahedral sites, as this occurs only at compositions of $x \geq 0.2$ (Kakol et al., 1991).

Because the relative intensity exhibits prominent changes with Ti concentration in titanomagnetite, it allows one to quickly determine Ti concentrations via a logarithmic relationship with the relative intensity of the $T_{2g}(2)$ peak, where

$$x = -1 - 0.3 \ln(T_{2g}(3)/A_{1g}) \qquad \text{Eq. (1)}$$

If the $T_{2g}(2)$ mode is not discernable, one could use a polynomial fit of the relative intensity of the $T_{2g}(3)/A_{1g}$ peak that varies as

$$x = 0.2 + 3(T_{2g}(2)/A_{1g}) - 4.5(T_{2g}(2)/A_{1g})^2 \qquad \text{Eq. (2)}$$

These are also shown in Figure 2. They can be used to roughly estimate Ti concentration in titanomagnetites.

Raman Spectroscopy of Titanomagnetite in a Natural Rock Sample

To check the effect of the Ti on Raman spectra of natural samples, we studied a magnetite-rich melatrocolite sample from Cumberland (Rhode Island), which was kindly supplied by Dr. M.J. Rutherford. It consists of olivine and titanomagnetite (to 32 v.%) with smaller amounts of plagioclase, Al-rich spinel, and ilmenite. The titanomagnetite grains contain pleonaste exsolution lamellae as well as ilmenite-rich lamellae formed by oxyexsolution. Petrology and petrography are described in detail by Rutherford and

Hermes (1984).

Titanomagnetite grains in a polished thin section of the sample (~15 mm x 6 mm) supplied by Dr. Rutherford were analyzed by EPMA and Raman microscopy. The analysis was focused on the ubiquitous Fe-Ti compositional gradation within the exsolved titanomagnetite grain host. Compositional variations are observed in reflected light photomicrographs as a transition in color from darker regions surrounding ilmenite lamellae to interstitial lighter regions (Figure 3a). We measured the Raman spectra as described but with t = 1x30 s at four spots on a single titanomagnetite grain.

The compositions of the four positions (A-D) shown in Figure 3a obtained by EPMA are listed in Table 3. Raman spectra taken at approximately the same position as EPMA are shown in Figure 2, 3b, and Table 2. Qualitatively, the changes in spectra with increasing Ti compare well to that of our TM samples described above especially if we consider the higher variations in intensity with increasing Ti (Figure 2) and slight offsets of the spots analyzed by EPMA and Raman microscope (Figure 3a). Using the equations obtained from the TM samples in the previous section, we find *x* values for the analyzed spots (Table 3). These values tell us that the Raman spectra of titanomagnetite provides us with Ti values with differences ranging from 4.1-16.6 % with respect to the values obtained by EPMA in the case of Eq. (2). However, minor elements that exist in this natural titanomagnetite such as Al and Mg could cause non-negligible effect on Raman spectra. Although the effect is suspected to be similar as Ti substitution because of their preference to enter octahedral sites over tetrahedral sites (Richards et al., 1973), it still remains to be a subject of further investigation for a full understanding of titanomagnetite

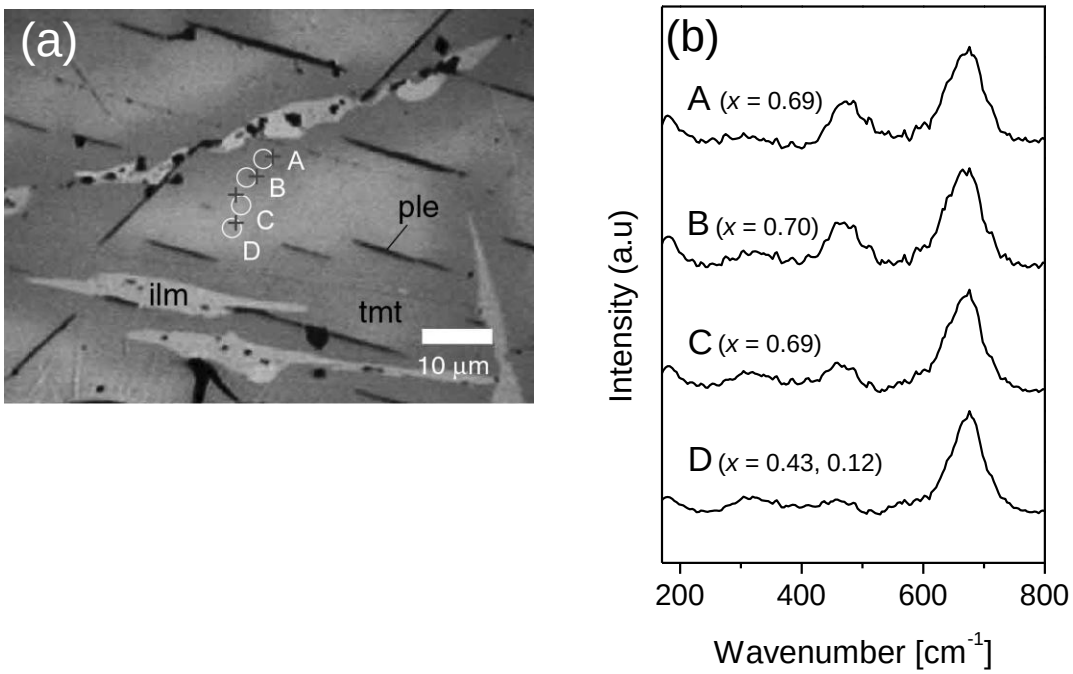

Figure 3. (a) A reflected light image of the region within titanomagnetite grain in melatroctolite sample analyzed by electron probe microanalyzer (EPMA) and Raman spectroscopy. Circles are spots analyzed by EPMA and crosses are by Raman. (b) Raman spectra of the four different spots shown in (a). The x values were found using equations (1) and (2). For A-C, equation (2) was not applicable since the peak $T_{2g}(2)$ was not discernible.

Table 3. Compositions of titanomagnetite in the melatroctolite sample as determined by electron probe microanalysis (EPMA). Cr was measured but is not listed because it was under detection level. The spot names A-D correspond to those in Figure 3. The number of cations for Ti are from EPMA and Raman spectroscopy. For EPMA, the values in parantheses are for the case in which other minor elements are disregarded in a pure titanomagnetite system. For Raman spectroscopy, the values were obtained by using the equation (1) for A-C. The first value for D is from the equation (1), and the second is from (2).

	A	B	C	D
TiO_2	23.68	23.08	13.42	12.84
Al_2O_3	3.93	3.63	2.98	2.30
V_2O_3	0.36	0.43	0.73	0.75
Fe_2O_3	17.49	19.20	36.96	39.44
FeO	49.88	49.49	41.00	40.71
MnO	0.39	0.41	0.26	0.23
MgO	1.78	1.72	1.14	1.08
Total	97.55	98.00	96.59	97.40
Number of cations on the bases of 4 oxygen atoms				
Ti (EPMA)	0.66 (0.74)	0.64 (0.71)	0.39 (0.42)	0.37 (0.39)
Ti (Raman)	0.69	0.70	0.69	0.43, 0.12
Al	0.17	0.16	0.13	0.10
V^{3+}	0.01	0.01	0.02	0.02
Fe^{3+}	0.49	0.54	1.07	1.13
Fe^{2+}	1.55	1.54	1.31	1.30
Mn^{2+}	0.01	0.01	0.01	0.01
Mg	0.10	0.10	0.07	0.06

Raman spectra of natural sample that can have non-negligible amount of minor elements.

Summary

Raman spectroscopy provides a convenient method of estimating the Ti content of titanomagnetite grains. Calibration of Raman spectra for titanomagnetite with known values of Ti concentration reveals a strong dependence of the relative intensity for the $T_{2g}(2)$ mode on the Ti concentration, particularly in the higher ranges of Ti content. The relative intensity of the $T_{2g}(3)$ mode shows the opposite trend and is more sensitive to changes in Ti concentrations for lower Ti-bearing titanomagnetite. Combining the two relative intensities potentially provides a sensitive indicator of Ti content.

Appendix A. Heating Treatment of Reagents for the Starting Materials

Order of Heating treatment[a]	Reagent	Temperature (°C)	Heating Time (h)	Storage
5	MgO	1000	48	oven @ 100 °C
	SiO2	1000	48	
	Al2O3	1000	48	
4	Cr2O3	800	6	oven @ 100 °C
	TiO2	800	4	
	Fe2O3	800	1	
3	CaCO3	400	6	desiccator
2	NaCO3	300	0.5	desiccator
1	K2CO3	110	0.5	desiccator
	MnCO3	110	2	
	CaHPO4	110	2	

[a] The order of weighing is a reverse of the heating treatment.

Appendix B. Weights of the Reagents and the Derivative Oxide wt.% for the Group 2 T-type Starting Material (MB2-50)

Reagent	Weight (g)	Oxide	Oxide (wt.%)
SiO2	5.3192	SiO2	50.75
TiO2	0.16623	TiO2	1.59
Al2O3	1.7665	Al2O3	16.86
Fe2O3	0.98161	FeO	8.43
MgO	0.7314	MgO	6.98
CaCO3	1.87399	CaO	10.41
CaHPO4	0.0996	Na2O	2.26
Na2CO3	0.40572	K2O	0.76
K2CO3	0.11741	P2O5	0.50
MnCO3	0.08975	MnO	0.53
Cr2O3	0.01085	Cr2O3	0.93
Total	11.5623	Total	100

Appendix C. Settings and Procedures of Sample Conditioning Using the Deltech Furnace

A schematic diagram of the furnace settings is illustrated in Appendix D. The bottom of the alumina furnace chamber was equipped with a glass container ~1/3 filled with water for a drop quench. A few sheets of alumina papers were laid on the bottom of the container as a physical and thermal cushion when the hot sample hits the bottom upon quench. If the furnace was used to generate a gas mixture to insert to the tube furnace as in section 2.1.1.3, an aluminum lid replaced this. One type of the brass top lid of the furnace chamber accommodated an alumina sample holder rod. The sample holder had two holes where a pair of Pt sample holder wires was passed through. The gaps between wires and holes at the top of the sample holder were sealed with household goop to avoid a gas leakage. The bottom of the wires was manually deformed to a hook-shape to accommodate a "zap" Pt wire for a drop quench. Another type of the top lid is very similar to the one described above, but it also accommodated a fO_2 sensor ($SIRO_2$ C700+ solid zirconia electrolyte oxygen sensor, Ceramic Oxide Fabricators) paired with a Pt-Rh thermocouple. For both cases, the sample holder and sensor positions were set so that the sample and sensor junctions would be at the empirically known "hot spot" of the Deltech furnace. The sample holder setting was to conduct a drop quench of the sample while the gas was flowing. It was done by applying an electric current (115 V) through the Pt wires to melt the zap wire where the sample was placed.

For the case of glass bead fusion as in section 2.1.1.2, the sample (powder) was mixed with poly vinyl alcohol for shaping, attached to the zap wire, and dried. For the case of the sample in Pt crucible, the crucible handle made of Pt wire was hung from the zap wire. After the sample was hung from the sample holder, the completion of a Pt circuit was confirmed by measuring a resistance across a pair of Pt sample holder wires using a voltmeter prior to insertion to the furnace. If the sensor was not used, the sample was inserted to the furnace set at the target temperature. If the sensor was in use, the furnace was set at 800 °C to insert the sample to avoid damage to the sensor and the furnace chamber. The furnace target temperatures were estimated to achieve the sample target temperatures based on obtained relationship between furnace set point and the actual sample temperature reported by the sensor through experimental records. Sample insertion was operated slowly. Particularly with the sensor, the rate of insertion was ~1 cm every 10 sec. Once the top lid was sealed, if the sample insertion was conducted at 800 °C, the temperature controller (Eurotherm) was programmed to ramp up to the target temperature at the rate of 150 $^{o}C\ h^{-1}$ at maximum. All necessary programming of temperature treatment of the sample was done at this moment.

In order to ascertain an absence of a gas leakage that could be hazardous and affect the stability of oxygen condition in the furnace, each of H_2 and CO_2 were first opened separately and junctions in the line were checked with a Mini Gas Leak Detector (Gow-Mac Instrument). It was also confirmed by checking the bubbler at the gas output. The bubbler consisted of two connected flasks where the terminal one contained water. When there was no gas leakage, gas would reach the bubbler and form bubbles in the water of the flask to inform the absence of the gas leakage. Another empty flask worked as a trap to collect water drawn from the terminal one instead of letting the water flowing into the furnace, which happened when the temperature was lowered in the furnace. Once

the absence of the leakage was confirmed, the gas lines for H_2 and CO_2 were opened in the order of gas cylinders, regulators (5 psi), and flowmeters (model 03227-00, Cole-Parmer) valves and knobs (>0 for H_2 and 150 for CO_2). The same operation was done for reference air for the oxygen sensor, where the flow reading was 5. It was empirically found that fO_2 was more reproducible by the number of turns of the knobs of the flowmeters rather than the readings in the flowmeters. It was probably because the ideal amounts of the gas flow for QFM were near the limitation of the both flowmeters (e.g., flow readings of >0 for H_2 and 150 for CO_2 were minimum and maximum readings, respectively). Used numbers of turns for the course of experiments were ~3 1/4 and ~7 1/2, respectively. Thus, for the glass bead fusion in which the sensor was not employed, the settings of the regulator and flowmeter knobs kept from the previous usage of the furnace with sensor at QFM. The oxygen level usually reached QFM condition approximately <1 h after input of the gases no matter whether the temperature was already at the target value as in glass fusion or it was at 950 °C ramping toward the target value.

The status of the temperature and fO_2 was checked everyday for a long term experiment. Gradual shift in fO_2 (e.g., 70 mV of increase in fO_2 over 41 h) was usually observed for long-term experiments using a sensor probably because of the observed slight decrease in regulator gas pressure. Therefore, the pressure of the regulator was raised back to 5 psi to restore the original oxygen level in the furnace.

Samples were quenched by applying an electric current through the Pt zap wire as mentioned earlier. The quench was confirmed by a presence of the sample in the water. The gas lines were closed in the order of cylinders, regulators, controller panel, and the T-junction of the flow line that allowed gas flow paths to two different furnaces, Deltech and tube furnaces. Approximately 1 min later, the furnace bottom seal was cracked by loosening the screws. Once the drop in fO_2 to near 0 mV was observed, the bottom water container was removed and replaced with Al bottom lid to retrieve the sample in the glass container.

Appendix D. A Schematic Cross-Sectional Diagram of the Deltech Furnace

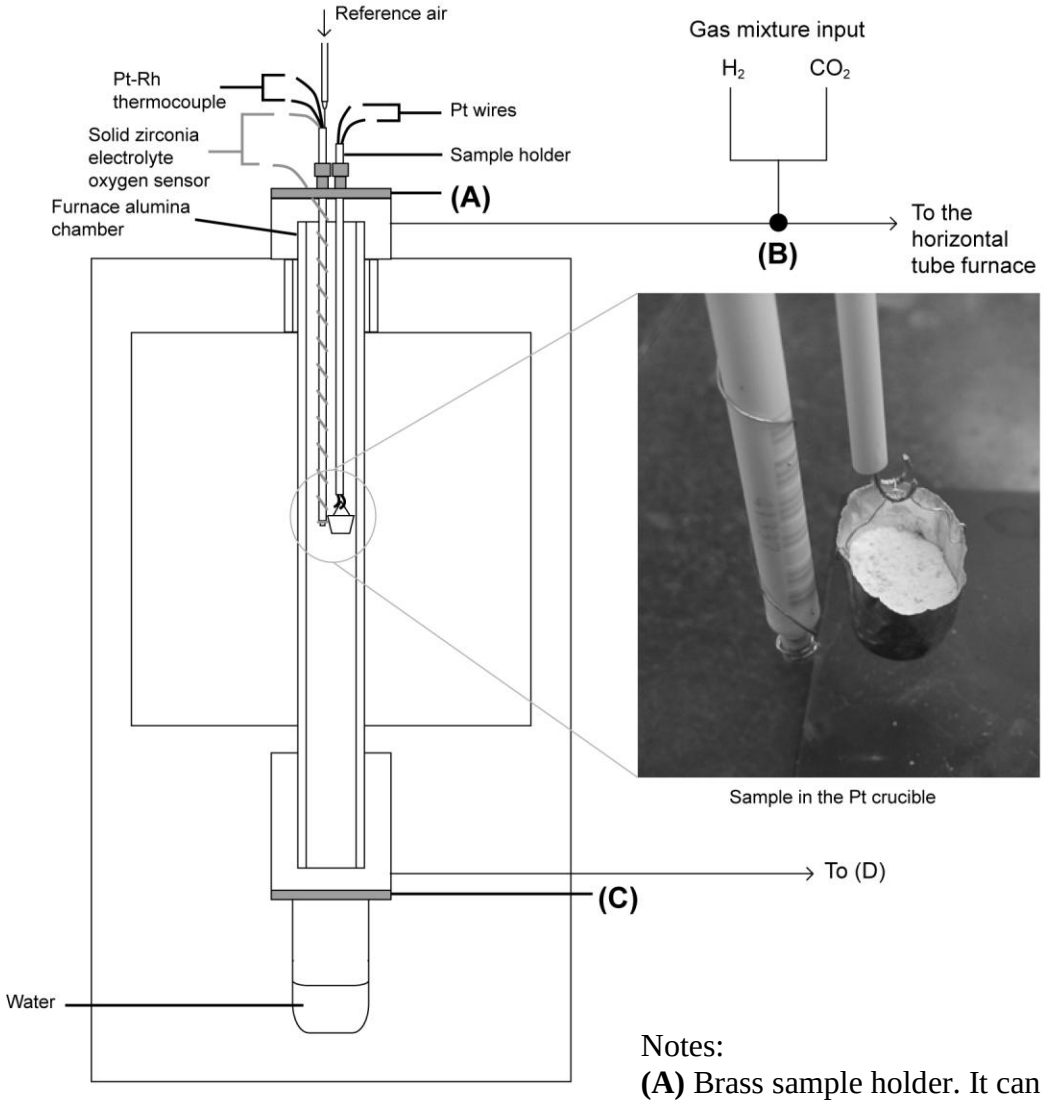

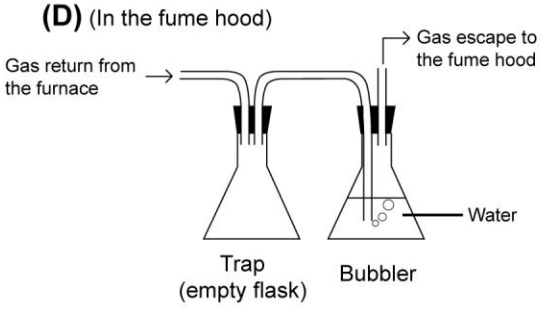

Notes:
(A) Brass sample holder. It can be switched to another holder that only accommodates only a sample holder rod.
(B) A junction at which gas flow can be directed either to the Deltech furnace or horizontal tube furnace.
(C) The glass container attached to aluminum plate for sample drop quench. It can be switched to a simple aluminum lid.
(D) Bubbler for confirmation of gas flow and absence of leakage.

Appendix E. A Schematic Cross-Sectional Diagram of the Tube Furnace Settings

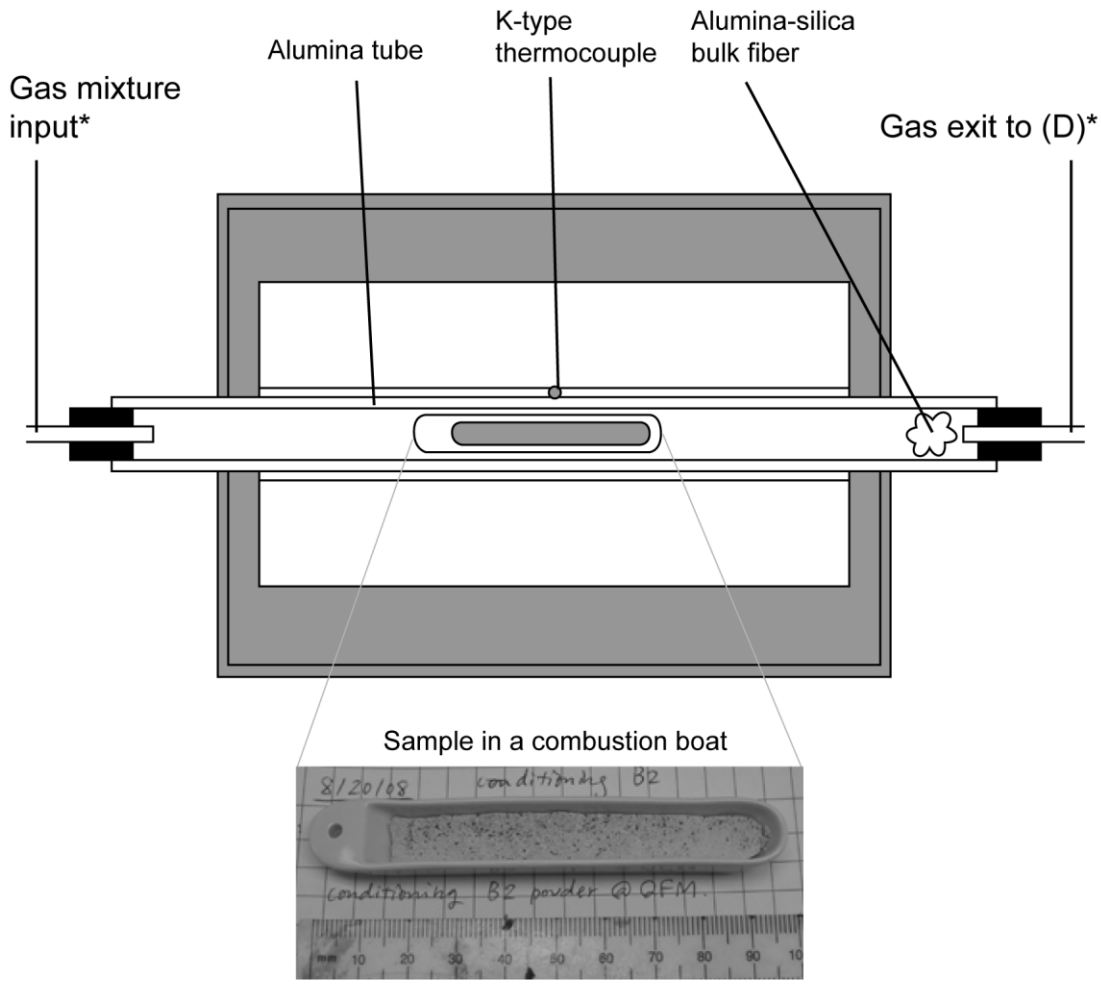

* See Appendix D.

Appendix F. A List of Additional Measurements Performed on the Samples

Sample	Expt group#	Duration [day]	Raman[a]	X[b]	ARM demag[c]	Low T[d]	FORC[e]	EBSD[f]	AFM, MFM[g]	Oxide Phases[h]	Exsolution types[i]
Meteorite-type:											
MAm-36 (starting material)	1	n.a.	LP	JB		JB				hem, femgal	n.a.
MAm-51 (starting material)	2	n.a.			DC	LP				timt	n.a.
MAm-E-03	1	54	LP	JB		JB			LP	mt, timt, femgal, femg	1, 2
MAm-E-09	2	21		DC	DC					timt	none
MAm-E-10	2	32		DC	DC					timt	none
MAm-E-11	2	48		DC	DC					timt	none
MAm-E-12	2	111	LP	DC	DC					timt	none
MAm-E-13	2	158	LP	DC	DC					timt	none
MAm-E-14	2	88	LP		LP	LP				timt, mt	1
MAm-E-15	2	88	LP		LP	LP				timt	none

Appendix F (Continued). A List of Additional Measurements Performed on the Samples

Sample	Expt group#	Duration [day]	Raman[a]	X[b]	ARM demag[c]	Low T[d]	FORC[e]	EBSD[f]	AFM, MFM[g]	Oxide Phases[h]	Exsolution types[i]
Terrestrial-type:											
MB2-31 (starting material)	1	100 h	LP	JB		JB	JB	JH	LP	hem, femgal	n.a.
MB2-48 (starting material)	2	100 h	LP		DC	LP				timt, ilm	n.a.
MB2-E-03	1	54	LP	JB		JB	JB	JH	LP	femgal, femg, mgf (tr.), timt? (tr.), mt? (tr.)	2, 3, 1?
MB2-E-09	2	21		DC	DC					timt, ilm	none
MB2-E-10	2	32		DC	DC					timt, ilm	none
MB2-E-11	2	48		DC	DC					timt, ilm, chr (tr.)	none
MB2-E-12	2	111	LP	DC	DC					timt, ilm	none
MB2-E-13	2	158	LP	DC	DC					timt, ilm	none
MB2-E-14	2	88	LP		LP	LP				timt, ilm	none
MB2-E-15	2	88			LP	LP				timt, ilm	none

Gray colums are for measurements, and the rest is sample information. Measured items are denoted with the name of the person who conducted the measurements. LP=Lisa Petrochilos, DC=David Cuomo, JB=Jluie Bowles, JH=Julia Hammer. For magnetic measurements, LP was under instruction of JB, both conducted at Institute for Rock Magnetism, University of Minnesota, and DC was under instruction of Stefanie Brachfeld.

The measurements that were performed to all the samples are unlisted here. Those include Natural Remanent Magnetization (NRM) demagnetization and Anhysteretic Remanent Magnetization (ARM) acquisition.

[a] Raman Spectroscopy at University of Hawai'i at Mānoa. See Part II of this thesis for methods.

[b] Room temperature magnetic susceptibility [m^3/kg]. Applied AC field=300 A/m, f=920 Hz (for JB) on Kappabridge. DC=Montclair State University.

[c] Alternating field (AF)=100 mT and DC bias field={100, 98} μT for {LP, DC} on 2G. DC=Lehigh University.

[d] Low temperature magnetic measurements including M_S-T (2.5 T), field cooled - zero field cooled (FC-ZFC) remanent magnetization (M_r) measurements (10-300 K, 2.5 T at 20 K for ZFC, 2.5 T on cooling for FC), room temperature saturation isothermal remanent magnetization (SIRM) at 2.5 T on cooling and warming, temperature-frequency-dependent susceptibility (10-300 K, f={1, 3, 10, 32, 100} Hz, AC field=239 A/m), on a Quantum Design Magnetic Properties Measurements System.

[e] First Order Reversal Curves.

[f] Electron Backscatter Diffraction on JEOL J5900 scanning electron microscope.

[g] Atomic/Magnetic Force Microscopy.

[h] Phases are listed in order of approximate decreasing volumetric abundance. hem=hematite, femgal=Fe-Mg-Al spinel oxide, timt=titanomagnetite, mt=magnetite, femg=Fe-Mg spinel oxide, mgf=magnesioferrite, ilm=ilmenite, (tr.)=trace phase.

[i] Exsolution types are listed in approximate decreasing volumetric abundance. Exsolution types: (1) magnetite - Al-bearing titanomagnetite, (2) Fe-Mg-Al spinel oxide - Fe-Mg spinel oxide, (3) Fe-Mg-Al spinel oxide - Al-bearing magnesioferrite.

Appendix G. EPMA Calibration Settings

Oxide	Std ID	Standard	Crystal	Spectrometer	Count Time (sec)
Glass [a]					
SiO_2	134	Glass, VG-2 USNM 104021	TAP	3	50
TiO_2	111	Sphene glass	PETJ	4	40
Al_2O_3	134	Glass, VG-2 USNM 104021	TAP	3	40
FeO	134	Glass, VG-2 USNM 104021	LiFH	2	30
MnO	102	Garnet, Verma (Mn)	LiFH	2	25
MgO	133*	Basalt Glass, A99 (USNM 113498/1)	TAP	1	60
CaO	134	Glass, VG-2 USNM 104021	PETH	5	40
Na_2O	115	Albite, Amelia	TAP	1	30
K_2O	119	Orthoclase (OR-1)	PETJ	4	50
P_2O_5	125	Fluor-apatite USNM 104021	PETH	5	40
Cr_2O_3	112	Chromite USNM 117075	LiFH	2	30
Oxides [b]					
SiO_2	102	Garnet, Verma (Mn)	TAP	3	20
TiO_2	111	Sphene glass	PETJ	1	60
Al_2O_3	102	Garnet, Verma (Mn)	TAP	3	30
Cr_2O_3	112	Chromite USNM 117075	LiFH	2	60
FeO	104*	Magnetite (minas gerais) USNM 114887	LiF	4	20
MnO	102	Garnet, Verma (Mn)	LiF	4	30
MgO	112	Chromite USNM 117075	TAPH	5	60

* Bench standards

[a] Accelerating voltage = 15 keV, beam current = 10 nA, beam diameter 10 µm

[b] Accelerating voltage = 15 keV, beam current = 20-25 nA, beam diameter 10 µm

Sample/spot[a]	SiO_2	TiO_2	Al_2O_3	Cr_2O_3	FeO(t)	MnO	MgO	Total	Fe_2O_3[b]	FeO[b]	Corr. Total[b]	Si	Ti	Al	Cr	Fe	Mn	Mg	Fe^{3+} [b]	Fe^{2+} [b]	Phase[c]	Exsolution types[d]
MAm-36_14	0.44	0.18	8.28	3.25	60.68	2.92	15.35	91.09	60.95	5.83	97.19	0.01	0.00	0.33	0.09	1.71	0.08	0.77	1.55	0.16	femgal	
MAm-36_15*	0.48	1.85	5.24	0.14	67.44	2.20	13.10	90.45	62.81	10.92	96.74	0.02	0.05	0.22	0.00	1.97	0.07	0.68	1.65	0.32	femgal	
MAm-36_16*	0.47	2.21	4.79	0.08	67.88	2.28	12.74	90.44	62.52	11.62	96.70	0.02	0.06	0.20	0.00	1.99	0.07	0.67	1.65	0.34	femgal	
MAm-36_22*	0.48	0.14	7.65	3.21	60.66	2.79	15.27	90.20	61.04	5.73	96.31	0.02	0.00	0.31	0.09	1.73	0.08	0.78	1.57	0.16	femgal	
MAm-36_23	0.49	2.04	4.63	0.18	67.66	2.19	12.46	89.64	62.15	11.73	95.86	0.02	0.05	0.19	0.01	2.01	0.07	0.66	1.66	0.35	femgal	
MAm-36_24	0.49	1.98	4.45	0.14	68.23	2.05	12.34	89.68	62.51	11.99	95.94	0.02	0.05	0.19	0.00	2.03	0.06	0.65	1.67	0.36	femgal	
MAm-36_27	0.49	2.16	4.49	0.09	68.03	2.15	12.44	89.85	62.33	11.94	96.09	0.02	0.06	0.19	0.00	2.01	0.06	0.66	1.66	0.35	femgal	
MAm-E-03_001	0.30	0.91	0.25	0.03	92.51	0.66	1.62	96.30	69.28	30.17	103.24	0.01	0.03	0.01	0.00	2.84	0.02	0.09	1.92	0.93	mt*	1
MAm-E-03_002	0.40	7.64	2.11	0.20	82.66	0.73	1.38	95.13	51.56	36.27	100.29	0.01	0.21	0.09	0.01	2.57	0.02	0.08	1.44	1.13	mt+timt*	1
MAm-E-03_003	0.38	2.91	0.81	0.04	89.34	0.68	1.87	96.03	64.17	31.59	102.46	0.01	0.08	0.04	0.00	2.75	0.02	0.10	1.77	0.97	mt*	1
MAm-E-03_004	0.32	7.38	2.08	0.15	82.82	0.74	1.63	95.11	52.53	35.55	100.37	0.01	0.21	0.09	0.00	2.57	0.02	0.09	1.47	1.10	timt*	1
MAm-E-03_005	0.35	1.16	7.04	0.73	74.48	0.62	11.06	95.44	64.16	16.74	101.87	0.01	0.03	0.28	0.02	2.09	0.02	0.55	1.62	0.47	femgal+femg*	2
MAm-E-03_006	0.24	0.23	6.04	9.47	70.79	0.95	3.89	91.61	51.10	24.81	96.73	0.01	0.01	0.26	0.28	2.20	0.03	0.22	1.43	0.77	femgal	
MAm-E-03_007	0.30	0.42	5.87	7.99	70.81	1.15	6.72	93.25	55.25	21.09	98.78	0.01	0.01	0.25	0.23	2.11	0.03	0.36	1.48	0.63	femgal+femg*	2
MAm-E-03_008	0.33	2.28	2.04	5.87	76.24	1.39	8.14	96.29	61.54	20.87	102.46	0.01	0.06	0.08	0.16	2.22	0.04	0.42	1.61	0.61	femgal+femg*	2
MAm-E-03_009	0.35	8.31	2.44	0.32	81.85	0.55	1.38	95.20	49.79	37.04	100.18	0.01	0.23	0.11	0.01	2.54	0.02	0.08	1.39	1.15	mt+timt*	1
MAm-E-03_011	0.46	2.15	4.17	0.06	71.36	2.12	9.77	90.09	61.49	16.03	96.25	0.02	0.06	0.18	0.00	2.15	0.06	0.53	1.67	0.48	femgal	
MAm-E-03_012	0.39	2.27	4.25	0.06	70.90	2.16	10.67	90.70	62.28	14.86	96.94	0.01	0.06	0.18	0.00	2.11	0.07	0.57	1.67	0.44	femgal	
MAm-E-03_013	0.49	1.93	4.24	0.09	72.71	1.95	9.23	90.65	61.82	17.08	96.84	0.02	0.05	0.18	0.00	2.19	0.06	0.50	1.68	0.51	femgal	
MAm-E-03_014*	0.39	9.29	2.71	0.86	78.56	0.50	1.04	93.35	45.18	37.90	97.87	0.01	0.27	0.12	0.03	2.50	0.02	0.06	1.29	1.20	mt*	1
MAm-E-03_015	0.32	10.12	2.77	0.25	80.28	0.51	0.84	95.09	45.38	39.44	99.63	0.01	0.28	0.12	0.01	2.51	0.02	0.05	1.28	1.23	timt*	1
MAm-E-03_016	0.44	0.89	0.30	0.05	92.98	0.44	1.17	96.27	68.61	31.24	103.14	0.02	0.02	0.01	0.00	2.87	0.01	0.06	1.90	0.96	mt*	1
MAm-E-03_019	0.40	6.80	2.19	0.65	83.76	0.59	1.30	95.70	53.07	36.00	101.01	0.01	0.19	0.10	0.02	2.59	0.02	0.07	1.48	1.11	mt*	1
MAm-E-03_020a	0.42	9.00	3.25	0.87	78.51	0.63	1.29	93.98	45.61	37.47	98.55	0.02	0.25	0.14	0.03	2.47	0.02	0.07	1.29	1.18	femgal+femg*	2
MAm-E-03_022	0.34	0.44	6.45	4.01	74.61	1.03	8.69	95.58	61.57	19.21	101.75	0.01	0.01	0.26	0.11	2.14	0.03	0.44	1.59	0.55	femgal+femg*	2
MAm-E-03_023	0.34	0.21	5.95	8.99	71.34	1.14	5.90	93.87	54.37	22.41	99.32	0.01	0.01	0.25	0.25	2.13	0.03	0.31	1.46	0.67	femgal+femg*	2
MAm-E-03_024	0.48	0.23	8.44	3.04	66.91	1.60	14.11	94.82	62.78	10.42	101.11	0.02	0.01	0.33	0.08	1.84	0.04	0.69	1.55	0.29	femgal	
MAm-E-03_025	0.45	0.20	6.12	9.00	70.78	1.10	5.73	93.39	53.42	22.71	98.74	0.02	0.01	0.26	0.26	2.12	0.03	0.31	1.44	0.68	femgal	
MAm-E-03_026	0.38	0.20	6.28	8.97	71.10	1.01	4.96	92.90	52.63	23.73	98.17	0.01	0.01	0.27	0.26	2.16	0.03	0.27	1.44	0.72	femgal	
MAm-E-03_027	0.36	0.35	5.61	6.74	72.75	1.20	7.92	94.93	58.87	19.78	100.83	0.01	0.01	0.23	0.19	2.12	0.04	0.41	1.54	0.58	femgal+femg*	2
MAm-E-03_028	0.48	2.03	1.75	3.15	77.40	1.45	9.39	95.65	65.26	18.68	102.18	0.02	0.05	0.07	0.09	2.24	0.04	0.49	1.70	0.54	femgal+femg*	2
MB2-31_001*	0.48	2.76	3.74	0.50	67.43	2.35	12.91	90.17	62.11	11.53	96.39	0.02	0.07	0.16	0.01	1.99	0.07	0.68	1.65	0.34	femgal	
MB2-31_002*	0.49	2.77	3.58	0.53	66.96	2.40	12.27	89.00	61.02	12.06	95.11	0.02	0.07	0.15	0.01	2.01	0.07	0.66	1.65	0.36	femgal	
MB2-31_003*	0.38	2.81	3.69	0.67	66.96	2.37	12.49	89.38	61.29	11.81	95.51	0.01	0.08	0.16	0.02	2.00	0.07	0.66	1.65	0.35	femgal	
MB2-31_005a*	0.41	3.07	3.87	1.43	71.52	1.65	7.45	89.40	56.73	20.47	95.08	0.02	0.09	0.17	0.04	2.22	0.05	0.41	1.59	0.64	femgal	
MB2-31_008*	0.34	2.66	3.71	1.97	66.69	2.42	12.60	90.39	61.08	11.72	96.51	0.01	0.07	0.15	0.05	1.97	0.07	0.66	1.62	0.35	femgal	
MB2-31_009*	0.25	0.57	5.83	3.39	63.22	2.59	13.94	89.78	61.75	7.66	95.97	0.01	0.01	0.24	0.09	1.84	0.08	0.72	1.62	0.22	femgal	
MB2-31_013	0.35	1.17	5.78	1.03	66.40	2.64	12.35	89.73	61.92	10.68	95.93	0.01	0.03	0.24	0.03	1.96	0.08	0.65	1.64	0.32	femgal	
MB2-31_014*	0.44	2.01	4.05	0.75	66.06	2.77	14.17	90.26	63.90	8.57	96.66	0.02	0.05	0.17	0.02	1.93	0.08	0.74	1.68	0.25	femgal	
MB2-31_016*	0.48	2.01	4.04	0.76	66.16	2.74	13.82	90.01	63.41	9.10	96.36	0.02	0.05	0.17	0.02	1.94	0.08	0.72	1.67	0.27	femgal	

Appendix H (Continued). Spinel Oxide Composition Data

Sample/spot[a]	SiO_2	TiO_2	Al_2O_3	Cr_2O_3	FeO(t)	MnO	MgO	Total	Fe_2O_3[b]	FeO[b]	Corr. Total[b]	Si	Ti	Al	Cr	Fe	Mn	Mg	Fe^{3+} [b]	Fe^{2+} [b]	Phase[c]	Exsolution types[d]
MB2-E-03_01a*	0.49	2.86	4.65	0.95	71.07	2.40	10.01	92.44	60.25	16.86	98.47	0.02	0.08	0.19	0.03	2.09	0.07	0.53	1.59	0.50	femgal*	3
MB2-E-03_02a	0.44	2.19	3.22	0.80	69.15	2.71	16.62	95.14	69.55	6.56	102.11	0.01	0.05	0.12	0.02	1.90	0.08	0.81	1.72	0.18	mgf*	3
MB2-E-03_27	0.47	2.11	3.04	0.87	69.56	2.72	17.83	96.60	71.59	5.14	103.77	0.02	0.05	0.12	0.02	1.87	0.07	0.85	1.73	0.14	femgal+mgf*	3
MB2-E-03_06a*	0.43	2.47	3.88	1.41	67.65	2.61	11.36	89.81	60.50	13.21	95.87	0.02	0.07	0.16	0.04	2.03	0.08	0.61	1.63	0.40	femgal	
MB2-E-03_09a	0.50	2.48	3.87	1.47	69.83	2.48	14.00	94.63	65.37	11.02	101.18	0.02	0.06	0.15	0.04	1.96	0.07	0.70	1.65	0.31	femgal	
MB2-E-03_10a*	0.37	2.42	3.43	1.17	69.53	2.72	16.67	96.31	69.47	7.01	103.27	0.01	0.06	0.13	0.03	1.89	0.07	0.81	1.70	0.19	mgf*	3
MB2-E-03_11a*	0.40	3.01	4.79	1.07	72.82	2.11	7.33	91.52	57.62	20.97	97.29	0.01	0.08	0.20	0.03	2.21	0.06	0.40	1.57	0.64	femgal*	3
MB2-E-03_15a	0.36	2.12	6.38	1.32	74.18	1.97	9.47	95.80	61.70	18.66	101.98	0.01	0.05	0.26	0.04	2.11	0.06	0.48	1.58	0.53	femgal+femg*	2
MB2-E-03_19	0.46	1.53	6.97	1.72	76.83	0.80	7.03	95.33	59.72	23.10	101.31	0.02	0.04	0.28	0.05	2.23	0.02	0.36	1.56	0.67	femgal*	2
MB2-E-03_20	0.49	0.64	2.90	1.14	80.43	0.78	10.23	96.61	70.05	17.40	103.62	0.02	0.02	0.12	0.03	2.28	0.02	0.52	1.79	0.49	femg*	2
MB2-E-03_21*	0.24	1.46	5.88	2.74	75.43	0.78	8.16	94.71	60.83	20.69	100.80	0.01	0.04	0.24	0.08	2.19	0.02	0.42	1.59	0.60	femgal+femg*	2
MB2-E-03_22	0.34	0.83	1.13	1.38	84.48	1.19	8.03	97.38	71.29	20.32	104.52	0.01	0.02	0.05	0.04	2.44	0.03	0.41	1.85	0.59	femg*	2
MB2-E-03_23	0.33	2.20	5.68	3.83	74.99	1.07	5.64	93.74	55.99	24.61	99.34	0.01	0.06	0.24	0.11	2.25	0.03	0.30	1.51	0.74	femgal*	2
MB2-E-03_24	0.26	2.34	5.03	3.62	76.08	1.08	6.71	95.13	58.57	23.38	100.99	0.01	0.06	0.21	0.10	2.24	0.03	0.35	1.55	0.69	femgal+femg*	2
MAm-51_11-1	0.49	12.25	3.00	0.00	75.85	0.58	1.82	93.99	40.29	39.60	98.03	0.02	0.35	0.13	0.00	2.38	0.02	0.10	1.14	1.24	timt	
MAm-51_15-1	0.50	12.48	3.23	0.01	75.10	0.53	1.88	93.72	39.32	39.72	97.66	0.02	0.35	0.14	0.00	2.36	0.02	0.11	1.11	1.25	timt	
MAm-51_1	0.45	13.76	2.67	0.03	73.52	0.51	1.97	92.92	36.92	40.30	96.62	0.02	0.39	0.12	0.00	2.34	0.02	0.11	1.06	1.28	timt	
MAm-51_3-1	0.45	13.91	2.87	0.01	73.63	0.55	2.12	93.55	36.94	40.39	97.25	0.02	0.39	0.13	0.00	2.32	0.02	0.12	1.05	1.27	timt	
MAm-51_6-1	0.44	13.53	3.21	0.01	74.15	0.62	2.11	94.05	37.70	40.22	97.83	0.02	0.38	0.14	0.00	2.32	0.02	0.12	1.06	1.26	timt	
MAm-51_1-1	0.39	13.90	2.78	0.07	74.37	0.59	2.03	94.13	37.53	40.60	97.88	0.01	0.39	0.12	0.00	2.34	0.02	0.11	1.06	1.27	timt	
MAm-51_10-1	0.49	13.20	2.96	0.02	73.83	0.63	2.00	93.12	37.82	39.80	96.91	0.02	0.38	0.13	0.00	2.34	0.02	0.11	1.08	1.26	timt	
MAm-51_7-1	0.42	13.08	3.06	0.07	74.18	0.56	2.07	93.45	38.32	39.71	97.29	0.02	0.37	0.14	0.00	2.34	0.02	0.12	1.09	1.25	timt	
MAm-51_7-2	0.48	12.96	2.99	0.03	74.45	0.60	2.04	93.55	38.61	39.71	97.42	0.02	0.37	0.13	0.00	2.35	0.02	0.11	1.10	1.25	timt	
MAm-51_9-1	0.47	13.13	2.88	0.00	74.85	0.58	2.03	93.93	38.73	39.99	97.81	0.02	0.37	0.13	0.00	2.35	0.02	0.11	1.10	1.26	timt	
MAm-51_15-1	0.44	12.60	3.43	0.01	75.10	0.56	1.88	94.02	39.18	39.84	97.95	0.02	0.36	0.15	0.00	2.35	0.02	0.11	1.11	1.25	timt	
MAm-51_16-1	0.34	13.06	3.08	0.20	74.94	0.58	1.87	94.07	38.74	40.08	97.95	0.01	0.37	0.14	0.01	2.35	0.02	0.10	1.09	1.26	timt	
MAm-51_17-1	0.48	12.66	3.00	0.02	75.32	0.54	1.78	93.81	39.28	39.98	97.75	0.02	0.36	0.13	0.00	2.37	0.02	0.10	1.11	1.26	timt	
MAm-51_17-2	0.46	11.96	3.21	0.00	74.92	0.54	1.88	92.98	39.96	38.96	96.98	0.02	0.34	0.14	0.00	2.37	0.02	0.11	1.14	1.23	timt	
MAm-51_01	0.49	12.77	3.13	0.00	75.04	0.58	1.79	93.81	38.86	40.07	97.70	0.02	0.36	0.14	0.00	2.36	0.02	0.10	1.10	1.26	timt	
MAm-51_04	0.43	13.74	2.92	0.03	74.04	0.57	2.02	93.73	37.36	40.43	97.48	0.02	0.39	0.13	0.00	2.33	0.02	0.11	1.06	1.27	timt	
MAm-51_05	0.44	12.78	3.16	0.02	75.00	0.57	1.82	93.79	38.92	39.98	97.69	0.02	0.36	0.14	0.00	2.36	0.02	0.10	1.10	1.26	timt	
MAm-51_06	0.45	14.96	2.84	0.05	72.67	0.61	2.21	93.79	34.98	41.19	97.29	0.02	0.42	0.13	0.00	2.29	0.02	0.12	0.99	1.30	timt	
MAm-51_07	0.44	12.97	3.09	0.03	74.22	0.58	2.03	93.36	38.41	39.66	97.21	0.02	0.37	0.14	0.00	2.34	0.02	0.11	1.09	1.25	timt	
MAm-51_09	0.47	12.97	2.90	0.01	74.96	0.58	1.95	93.82	38.92	39.94	97.72	0.02	0.37	0.13	0.00	2.36	0.02	0.11	1.10	1.26	timt	

Appendix H (Continued). Spinel Oxide Composition Data

Sample/spot[a]	SiO_2	TiO_2	Al_2O_3	Cr_2O_3	FeO(t)	MnO	MgO	Total	Fe_2O_3[b]	FeO[b]	Corr. Total[b]	Si	Ti	Al	Cr	Fe	Mn	Mg	Fe^{3+} [b]	Fe^{2+} [b]	Phase[c]	Exsolution types[d]
MAm-E-09_5-2	0.39	11.33	3.18	0.01	77.29	0.52	1.68	94.40	42.43	39.11	98.65	0.01	0.32	0.14	0.00	2.42	0.02	0.09	1.19	1.22	timt	
MAm-E-09_5-4	0.50	12.23	2.89	0.00	75.00	0.60	1.43	92.65	39.22	39.71	96.57	0.02	0.35	0.13	0.00	2.40	0.02	0.08	1.13	1.27	timt	
MAm-E-09_5-5	0.49	12.52	2.78	0.03	74.06	0.64	1.65	92.17	38.52	39.40	96.03	0.02	0.36	0.13	0.00	2.38	0.02	0.09	1.11	1.26	timt	
MAm-E-09_5-6	0.48	11.97	3.27	0.01	74.65	0.52	1.61	92.51	39.30	39.28	96.45	0.02	0.34	0.15	0.00	2.38	0.02	0.09	1.13	1.25	timt	
MAm-E-09_5-10	0.48	11.92	3.12	0.00	75.22	0.52	1.44	92.70	39.66	39.54	96.67	0.02	0.34	0.14	0.00	2.40	0.02	0.08	1.14	1.26	timt	
MAm-E-09_6-3	0.49	11.57	3.24	0.03	75.87	0.52	1.46	93.18	40.56	39.38	97.24	0.02	0.33	0.14	0.00	2.41	0.02	0.08	1.16	1.25	timt	
MAm-E-09_7-1	0.39	12.94	2.99	0.42	68.88	0.51	1.60	87.73	33.89	38.38	91.13	0.02	0.39	0.14	0.01	2.32	0.02	0.10	1.03	1.29	timt	
MAm-E-09_7-2	0.48	12.46	2.77	0.03	75.20	0.53	1.49	92.96	39.18	39.95	96.88	0.02	0.36	0.12	0.00	2.40	0.02	0.08	1.12	1.27	timt	
MAm-E-09_7-3	0.32	12.40	2.81	0.06	76.05	0.51	1.42	93.57	40.02	40.03	97.57	0.01	0.35	0.13	0.00	2.41	0.02	0.08	1.14	1.27	timt	
MAm-E-09_4-3	0.42	11.89	2.87	0.00	75.65	0.48	1.46	92.77	40.25	39.43	96.80	0.02	0.34	0.13	0.00	2.41	0.02	0.08	1.16	1.26	timt	
MAm-E-09_3-1	0.42	11.65	3.03	0.01	76.23	0.44	1.23	92.99	40.59	39.71	97.06	0.02	0.33	0.14	0.00	2.43	0.01	0.07	1.16	1.27	timt	
MAm-E-09_3-2	0.45	11.48	2.96	0.02	76.47	0.49	1.45	93.33	41.30	39.32	97.47	0.02	0.33	0.13	0.00	2.42	0.02	0.08	1.18	1.25	timt	
MAm-E-09_2-1	0.36	12.12	2.91	0.02	75.71	0.47	1.43	93.01	40.03	39.69	97.02	0.01	0.35	0.13	0.00	2.41	0.02	0.08	1.15	1.26	timt	
MAm-E-09_2-3	0.41	11.92	2.89	0.01	75.30	0.54	1.41	92.49	39.92	39.37	96.49	0.02	0.34	0.13	0.00	2.41	0.02	0.08	1.15	1.26	timt	
MAm-E-09_2-4	0.49	11.97	2.84	0.01	75.36	0.50	1.39	92.56	39.74	39.60	96.54	0.02	0.34	0.13	0.00	2.41	0.02	0.08	1.14	1.27	timt	
MAm-E-09_8-2	0.41	6.26	3.75	0.07	79.61	0.51	1.53	92.15	50.34	34.31	97.19	0.02	0.18	0.17	0.00	2.53	0.02	0.09	1.44	1.09	timt	
MAm-E-09_8-7	0.48	5.90	3.85	0.22	79.23	0.44	1.52	91.63	50.23	34.03	96.66	0.02	0.17	0.17	0.01	2.53	0.01	0.09	1.44	1.09	timt	
MAm-E-09_11-1	0.50	8.96	3.01	0.69	76.87	0.50	1.22	91.73	44.31	37.00	96.17	0.02	0.26	0.14	0.02	2.48	0.02	0.07	1.28	1.19	timt	
MAm-E-09_11-3	0.50	8.51	3.10	1.91	76.36	0.47	1.39	92.24	44.26	36.54	96.68	0.02	0.24	0.14	0.06	2.44	0.02	0.08	1.27	1.17	timt	
MAm-E-09_12-1	0.48	14.04	3.38	0.03	73.96	0.55	1.61	94.05	36.00	41.57	97.66	0.02	0.40	0.15	0.00	2.33	0.02	0.09	1.02	1.31	timt	
MAm-E-09_12-2	0.36	14.11	3.39	0.01	73.64	0.47	1.73	93.71	36.00	41.25	97.31	0.01	0.40	0.15	0.00	2.32	0.01	0.10	1.02	1.30	timt	
MAm-E-09_13-1	0.40	13.92	3.41	0.03	73.40	0.55	1.83	93.53	36.16	40.86	97.15	0.02	0.40	0.15	0.00	2.32	0.02	0.10	1.03	1.29	timt	
MAm-E-09_15-1	0.45	15.11	2.77	0.28	72.74	0.54	1.66	93.55	34.02	42.13	96.96	0.02	0.43	0.12	0.01	2.31	0.02	0.09	0.97	1.34	timt	
MAm-E-09_15-2	0.44	15.32	2.81	0.15	61.03	0.47	1.49	81.70	24.82	38.69	84.19	0.02	0.50	0.14	0.01	2.22	0.02	0.10	0.81	1.41	timt	
MAm-E-09_17-1	0.48	14.62	2.74	0.08	73.16	0.51	1.57	93.16	34.88	41.77	96.65	0.02	0.42	0.12	0.00	2.33	0.02	0.09	1.00	1.33	timt	
MAm-E-09_5-8_2	0.50	12.02	3.23	0.01	75.26	0.55	1.66	93.23	39.78	39.46	97.22	0.02	0.34	0.14	0.00	2.38	0.02	0.09	1.13	1.25	timt	
MAm-E-09_6-1_2	0.51	11.64	3.19	0.06	74.97	0.52	1.55	92.43	39.89	39.08	96.43	0.02	0.33	0.14	0.00	2.40	0.02	0.09	1.15	1.25	timt	
MAm-E-09_8-1_2	0.42	6.14	3.76	0.06	79.34	0.45	1.44	91.62	50.11	34.25	96.64	0.02	0.18	0.17	0.00	2.54	0.01	0.08	1.44	1.10	timt	
MAm-E-09_8-4_2	0.45	6.01	3.70	0.21	79.53	0.43	1.21	91.53	50.03	34.51	96.54	0.02	0.17	0.17	0.01	2.55	0.01	0.07	1.44	1.11	timt	
MAm-E-09_16-1_2	0.50	15.30	2.71	0.08	73.10	0.51	1.58	93.77	33.92	42.58	97.17	0.02	0.44	0.12	0.00	2.32	0.02	0.09	0.97	1.35	timt	
MAm-E-10_3-2	0.40	10.37	2.86	0.03	77.36	0.46	1.37	92.86	43.44	38.27	97.21	0.02	0.30	0.13	0.00	2.47	0.01	0.08	1.25	1.22	timt	
MAm-E-10_3-4	0.40	10.63	2.83	0.00	76.88	0.44	1.38	92.57	42.77	38.40	96.85	0.02	0.31	0.13	0.00	2.46	0.01	0.08	1.23	1.23	timt	

Appendix H (Continued). Spinel Oxide Composition Data

Sample/spot[a]	SiO_2	TiO_2	Al_2O_3	Cr_2O_3	FeO(t)	MnO	MgO	Total	Fe_2O_3[b]	FeO[b]	Corr. Total[b]	Si	Ti	Al	Cr	Fe	Mn	Mg	Fe^{3+} [b]	Fe^{2+} [b]	Phase[c]	Exsolution types[d]
MAm-E-10_4-2	0.30	11.17	3.51	0.05	75.34	0.50	1.58	92.45	41.02	38.43	96.56	0.01	0.32	0.16	0.00	2.40	0.02	0.09	1.18	1.23	timt	
MAm-E-10_4-3	0.30	11.06	3.35	0.03	76.45	0.50	1.51	93.20	41.98	38.67	97.40	0.01	0.32	0.15	0.00	2.42	0.02	0.09	1.20	1.22	timt	
MAm-E-10_4-4	0.49	10.94	3.50	0.00	76.03	0.52	1.46	92.95	41.38	38.79	97.10	0.02	0.31	0.16	0.00	2.41	0.02	0.08	1.18	1.23	timt	
MAm-E-10_4-3_2	0.35	11.11	3.35	0.01	76.39	0.55	1.49	93.23	41.81	38.76	97.42	0.01	0.32	0.15	0.00	2.42	0.02	0.08	1.19	1.23	timt	
MAm-E-10_6-1	0.40	11.32	3.02	0.02	76.41	0.53	1.60	93.28	41.75	38.83	97.47	0.01	0.32	0.13	0.00	2.42	0.02	0.09	1.19	1.23	timt	
MAm-E-10_6-2	0.35	10.63	3.29	0.02	77.17	0.49	1.56	93.51	43.09	38.39	97.83	0.01	0.30	0.15	0.00	2.43	0.02	0.09	1.22	1.21	timt	
MAm-E-10_7-1	0.50	10.78	3.14	0.06	76.25	0.50	1.48	92.71	41.93	38.53	96.91	0.02	0.31	0.14	0.00	2.43	0.02	0.08	1.20	1.23	timt	
MAm-E-10_7-1_2	0.46	10.94	3.21	0.04	76.37	0.50	1.62	93.14	42.02	38.56	97.35	0.02	0.31	0.14	0.00	2.42	0.02	0.09	1.20	1.22	timt	
MAm-E-10_7-3	0.46	10.99	3.04	0.01	76.37	0.48	1.50	92.85	41.88	38.68	97.04	0.02	0.31	0.14	0.00	2.43	0.02	0.09	1.20	1.23	timt	
MAm-E-10_5-2	0.47	11.25	3.39	0.01	76.49	0.54	1.44	93.60	41.37	39.26	97.74	0.02	0.32	0.15	0.00	2.41	0.02	0.08	1.17	1.24	timt	
MAm-E-10_10-1	0.40	11.78	3.34	0.00	75.52	0.56	1.77	93.39	40.55	39.03	97.45	0.02	0.33	0.15	0.00	2.38	0.02	0.10	1.15	1.23	timt	
MAm-E-10_10-1_2	0.41	11.86	3.42	0.00	76.03	0.54	1.83	94.09	40.84	39.29	98.18	0.02	0.33	0.15	0.00	2.38	0.02	0.10	1.15	1.23	timt	
MAm-E-10_10-2	0.48	11.70	3.42	0.00	74.89	0.50	1.56	92.55	39.70	39.17	96.52	0.02	0.34	0.15	0.00	2.39	0.02	0.09	1.14	1.25	timt	
MAm-E-10_8-1	0.44	12.36	2.97	0.02	75.75	0.52	1.41	93.47	39.57	40.14	97.43	0.02	0.35	0.13	0.00	2.40	0.02	0.08	1.13	1.27	timt	
MAm-E-10_8-2	0.43	12.23	2.93	0.01	74.93	0.48	1.50	92.50	39.27	39.59	96.43	0.02	0.35	0.13	0.00	2.40	0.02	0.09	1.13	1.27	timt	
MAm-E-10_8-3	0.37	12.41	3.03	0.00	75.36	0.56	1.84	93.57	39.90	39.46	97.56	0.01	0.35	0.13	0.00	2.38	0.02	0.10	1.13	1.25	timt	
MAm-E-10_9-1	0.44	12.28	2.89	0.01	75.93	0.53	1.69	93.78	40.22	39.74	97.81	0.02	0.35	0.13	0.00	2.39	0.02	0.09	1.14	1.25	timt	
MAm-E-10_9-3	0.36	11.83	2.95	0.04	75.90	0.56	1.67	93.30	40.91	39.09	97.40	0.01	0.34	0.13	0.00	2.40	0.02	0.09	1.17	1.24	timt	
MAm-E-10_9-4	0.42	11.40	3.08	0.00	75.92	0.54	1.53	92.89	41.13	38.90	97.01	0.02	0.33	0.14	0.00	2.42	0.02	0.09	1.18	1.24	timt	
MAm-E-10_11-1	0.49	11.70	2.76	0.00	76.08	0.52	1.32	92.87	40.59	39.55	96.93	0.02	0.34	0.12	0.00	2.43	0.02	0.07	1.17	1.26	timt	
MAm-E-10_11-2	0.43	11.70	2.74	0.00	75.50	0.47	1.44	92.27	40.40	39.14	96.32	0.02	0.34	0.12	0.00	2.42	0.02	0.08	1.17	1.26	timt	
MAm-E-10_11-4	0.48	11.80	2.77	0.01	75.84	0.57	1.49	92.95	40.57	39.33	97.02	0.02	0.34	0.12	0.00	2.42	0.02	0.08	1.16	1.25	timt	
MAm-E-10_11-5	0.42	11.96	2.76	0.02	75.55	0.49	1.31	92.51	39.95	39.61	96.51	0.02	0.34	0.12	0.00	2.42	0.02	0.07	1.15	1.27	timt	
MAm-E-10_15-1	0.43	12.79	3.04	0.06	74.93	0.50	1.51	93.25	38.47	40.31	97.11	0.02	0.37	0.14	0.00	2.38	0.02	0.09	1.10	1.28	timt	
MAm-E-10_15-1_2	0.46	12.75	3.05	0.03	74.93	0.50	1.47	93.18	38.43	40.35	97.03	0.02	0.36	0.14	0.00	2.38	0.02	0.08	1.10	1.28	timt	
MAm-E-10_16-7	0.41	12.89	2.86	0.00	75.43	0.51	1.49	93.61	38.84	40.48	97.50	0.02	0.37	0.13	0.00	2.39	0.02	0.08	1.11	1.28	timt	
MAm-E-10_12-1	0.49	12.83	2.74	0.01	75.14	0.47	1.43	93.10	38.52	40.48	96.96	0.02	0.37	0.12	0.00	2.39	0.02	0.08	1.10	1.29	timt	
MAm-E-10_12-2	0.48	12.27	2.79	0.12	75.65	0.53	1.34	93.18	39.52	40.08	97.14	0.02	0.35	0.13	0.00	2.41	0.02	0.08	1.13	1.28	timt	
MAm-E-10_13-1	0.43	13.42	2.76	0.02	74.33	0.53	1.38	92.86	37.19	40.86	96.59	0.02	0.39	0.12	0.00	2.38	0.02	0.08	1.07	1.31	timt	
MAm-E-10_13-2	0.40	13.12	2.97	0.01	75.20	0.52	1.54	93.76	38.40	40.65	97.61	0.02	0.37	0.13	0.00	2.38	0.02	0.09	1.09	1.28	timt	
MAm-E-10_13-3	0.37	13.13	2.79	0.00	74.74	0.47	1.44	92.94	38.03	40.52	96.75	0.01	0.38	0.13	0.00	2.39	0.02	0.08	1.09	1.29	timt	
MAm-E-10_13-5	0.35	13.24	2.74	0.03	74.11	0.51	1.41	92.39	37.43	40.43	96.14	0.01	0.38	0.12	0.00	2.38	0.02	0.08	1.08	1.30	timt	
MAm-E-10_14-1	0.47	14.25	2.76	0.01	73.45	0.54	1.44	92.93	35.48	41.53	96.48	0.02	0.41	0.12	0.00	2.35	0.02	0.08	1.02	1.33	timt	
MAm-E-10_1-1_2	0.36	3.14	10.15	0.00	72.08	0.48	6.67	92.88	52.45	24.88	98.14	0.01	0.08	0.42	0.00	2.12	0.01	0.35	1.39	0.73	timt	
MAm-E-11_1-3	0.48	11.88	3.14	0.00	75.15	0.50	1.46	92.61	39.66	39.46	96.59	0.02	0.34	0.14	0.00	2.40	0.02	0.08	1.14	1.26	timt	
MAm-E-11_1-7	0.49	11.48	3.18	0.02	75.00	0.45	1.32	91.94	39.81	39.18	95.92	0.02	0.33	0.14	0.00	2.41	0.01	0.08	1.15	1.26	timt	
MAm-E-11_2-1	0.45	11.35	2.95	0.00	75.88	0.50	1.44	92.58	41.04	38.96	96.69	0.02	0.33	0.13	0.00	2.43	0.02	0.08	1.18	1.25	timt	

Appendix H (Continued). Spinel Oxide Composition Data

Sample/spot[a]	SiO_2	TiO_2	Al_2O_3	Cr_2O_3	FeO(t)	MnO	MgO	Total	Fe_2O_3[b]	FeO[b]	Corr. Total[b]	Si	Ti	Al	Cr	Fe	Mn	Mg	Fe^{3+} [b]	Fe^{2+} [b]	Phase[c]	Exsolution types[d]
MAm-E-11_2-2	0.40	11.57	2.92	0.01	76.91	0.50	1.47	93.77	41.65	39.43	97.94	0.01	0.33	0.13	0.00	2.43	0.02	0.08	1.18	1.24	timt	
MAm-E-11_2-3	0.46	11.33	2.81	0.00	76.53	0.52	1.35	93.00	41.50	39.18	97.16	0.02	0.32	0.13	0.00	2.44	0.02	0.08	1.19	1.25	timt	
MAm-E-11_2-4	0.36	11.44	2.89	0.01	76.99	0.54	1.34	93.57	41.82	39.36	97.76	0.01	0.33	0.13	0.00	2.44	0.02	0.08	1.19	1.25	timt	
MAm-E-11_3-2	0.39	11.60	2.83	0.02	76.46	0.53	1.33	93.15	41.16	39.42	97.27	0.01	0.33	0.13	0.00	2.43	0.02	0.08	1.18	1.25	timt	
MAm-E-11_3-3	0.29	11.46	2.80	0.02	76.13	0.47	1.46	92.64	41.42	38.86	96.78	0.01	0.33	0.13	0.00	2.43	0.02	0.08	1.19	1.24	timt	
MAm-E-11_4-1	0.41	12.11	2.91	0.00	76.05	0.54	1.56	93.59	40.42	39.68	97.63	0.02	0.34	0.13	0.00	2.40	0.02	0.09	1.15	1.25	timt	
MAm-E-11_4-2	0.37	12.04	2.83	0.00	76.15	0.52	1.47	93.38	40.58	39.64	97.44	0.01	0.34	0.13	0.00	2.42	0.02	0.08	1.16	1.26	timt	
MAm-E-11_4-3	0.44	11.83	2.81	0.01	75.36	0.47	1.32	92.24	39.91	39.45	96.24	0.02	0.34	0.13	0.00	2.42	0.02	0.08	1.15	1.27	timt	
MAm-E-11_11-1	0.49	10.88	2.87	0.01	76.68	0.51	1.32	92.76	42.08	38.82	96.97	0.02	0.31	0.13	0.00	2.45	0.02	0.07	1.21	1.24	timt	
MAm-E-11_11-2	0.48	10.86	2.86	0.01	77.75	0.47	1.25	93.68	42.78	39.25	97.97	0.02	0.31	0.13	0.00	2.46	0.01	0.07	1.22	1.24	timt	
MAm-E-11_11-2_2	0.46	10.93	2.87	0.01	77.96	0.49	1.24	93.96	42.89	39.36	98.26	0.02	0.31	0.13	0.00	2.46	0.02	0.07	1.22	1.24	timt	
MAm-E-11_11-3	0.39	10.90	2.78	0.01	76.87	0.46	1.19	92.59	42.20	38.90	96.82	0.02	0.31	0.13	0.00	2.46	0.02	0.07	1.22	1.25	timt	
MAm-E-11_5-1	0.34	10.87	2.81	0.00	76.10	0.54	1.51	92.18	42.22	38.11	96.41	0.01	0.31	0.13	0.00	2.44	0.02	0.09	1.22	1.22	timt	
MAm-E-11_5-2	0.42	10.84	2.85	0.01	76.34	0.54	1.41	92.42	42.14	38.42	96.64	0.02	0.31	0.13	0.00	2.44	0.02	0.08	1.21	1.23	timt	
MAm-E-11_6-1	0.35	11.19	2.85	0.01	76.25	0.55	1.46	92.66	41.82	38.62	96.85	0.01	0.32	0.13	0.00	2.44	0.02	0.08	1.20	1.23	timt	
MAm-E-11_7-1	0.43	12.63	2.87	0.00	76.26	0.51	1.48	94.18	39.75	40.49	98.17	0.02	0.36	0.13	0.00	2.40	0.02	0.08	1.13	1.27	timt	
MAm-E-11_7-3	0.45	12.66	2.81	0.00	75.03	0.52	1.45	92.93	38.76	40.15	96.81	0.02	0.36	0.13	0.00	2.39	0.02	0.08	1.11	1.28	timt	
MAm-E-11_7-4	0.41	12.40	2.81	0.00	75.55	0.51	1.39	93.08	39.47	40.03	97.03	0.02	0.36	0.13	0.00	2.41	0.02	0.08	1.13	1.28	timt	
MAm-E-11_8-1	0.48	13.00	2.97	0.05	74.64	0.51	1.39	93.06	37.76	40.66	96.84	0.02	0.37	0.13	0.00	2.38	0.02	0.08	1.08	1.30	timt	
MAm-E-11_8-1_2	0.50	13.02	3.04	0.07	75.50	0.49	1.43	94.05	38.36	40.99	97.89	0.02	0.37	0.14	0.00	2.38	0.02	0.08	1.09	1.29	timt	
MAm-E-11_8-2	0.49	12.89	3.04	0.09	74.42	0.53	1.46	92.90	37.79	40.41	96.68	0.02	0.37	0.14	0.00	2.37	0.02	0.08	1.08	1.29	timt	
MAm-E-11_9-1	0.35	11.34	2.85	0.00	76.18	0.56	1.43	92.72	41.53	38.81	96.87	0.01	0.33	0.13	0.00	2.43	0.02	0.08	1.19	1.24	timt	
MAm-E-11_10-1	0.35	11.28	2.82	0.00	75.97	0.53	1.49	92.44	41.52	38.61	96.60	0.01	0.32	0.13	0.00	2.43	0.02	0.08	1.20	1.24	timt	
MAm-E-12_001	0.37	12.98	3.35	0.01	74.65	0.54	1.66	93.55	38.20	40.27	97.37	0.01	0.37	0.15	0.00	2.36	0.02	0.09	1.09	1.27	timt	
MAm-E-12_002	0.33	13.06	3.43	0.04	74.94	0.51	1.58	93.89	38.20	40.57	97.71	0.01	0.37	0.15	0.00	2.36	0.02	0.09	1.08	1.28	timt	
MAm-E-12_003	0.46	12.38	3.36	0.10	75.42	0.51	1.46	93.68	39.09	40.24	97.59	0.02	0.35	0.15	0.00	2.38	0.02	0.08	1.11	1.27	timt	
MAm-E-12_004	0.34	12.53	3.41	0.22	75.69	0.54	1.68	94.41	39.55	40.11	98.37	0.01	0.35	0.15	0.01	2.37	0.02	0.09	1.11	1.25	timt	
MAm-E-12_005	0.47	12.46	3.40	0.05	75.96	0.50	1.40	94.24	39.28	40.62	98.18	0.02	0.35	0.15	0.00	2.38	0.02	0.08	1.11	1.28	timt	
MAm-E-12_006	0.47	14.07	3.17	0.01	74.83	0.42	1.47	94.44	36.45	42.02	98.09	0.02	0.40	0.14	0.00	2.35	0.01	0.08	1.03	1.32	timt	
MAm-E-12_007	0.41	13.65	3.31	0.01	75.05	0.52	1.26	94.20	37.00	41.75	97.91	0.02	0.39	0.15	0.00	2.36	0.02	0.07	1.05	1.32	timt	
MAm-E-12_008	0.49	13.59	3.31	0.01	74.68	0.46	1.24	93.79	36.61	41.74	97.46	0.02	0.39	0.15	0.00	2.36	0.01	0.07	1.04	1.32	timt	

Appendix H (Continued). Spinel Oxide Composition Data

Sample/spot[a]	SiO_2	TiO_2	Al_2O_3	Cr_2O_3	FeO(t)	MnO	MgO	Total	Fe_2O_3[b]	FeO[b]	Corr. Total[b]	Si	Ti	Al	Cr	Fe	Mn	Mg	Fe^{3+}[b]	Fe^{2+}[b]	Phase[c]	Exsolution types[d]
MAm-E-12_009	0.43	12.31	3.37	0.01	75.06	0.43	1.48	93.09	38.96	40.00	96.99	0.02	0.35	0.15	0.00	2.38	0.01	0.08	1.11	1.27	timt	
MAm-E-12_012	0.41	12.53	2.83	0.02	74.91	0.51	1.45	92.67	38.88	39.93	96.56	0.02	0.36	0.13	0.00	2.40	0.02	0.08	1.12	1.28	timt	
MAm-E-12_013	0.47	12.57	2.81	0.02	76.32	0.52	1.41	94.12	39.74	40.56	98.10	0.02	0.36	0.12	0.00	2.40	0.02	0.08	1.13	1.28	timt	
MAm-E-12_014	0.48	12.50	2.84	0.02	75.45	0.49	1.48	93.25	39.22	40.16	97.18	0.02	0.36	0.13	0.00	2.40	0.02	0.08	1.12	1.28	timt	
MAm-E-12_017	0.43	12.64	2.76	0.02	75.28	0.46	1.43	93.02	38.97	40.21	96.92	0.02	0.36	0.12	0.00	2.40	0.01	0.08	1.12	1.28	timt	
MAm-E-12_019	0.46	12.01	3.23	0.05	76.31	0.51	1.26	93.83	40.06	40.27	97.84	0.02	0.34	0.14	0.00	2.41	0.02	0.07	1.14	1.27	timt	
MAm-E-12_023	0.46	12.31	3.05	0.01	76.25	0.44	1.11	93.63	39.48	40.73	97.58	0.02	0.35	0.14	0.00	2.42	0.01	0.06	1.13	1.29	timt	
MAm-E-12_028	0.49	9.26	3.13	1.34	76.97	0.47	1.12	92.80	43.55	37.79	97.16	0.02	0.27	0.14	0.04	2.46	0.02	0.06	1.25	1.21	timt	
MAm-E-12_029	0.43	6.24	3.74	8.32	71.62	0.53	1.52	92.39	41.52	34.25	96.55	0.02	0.18	0.17	0.25	2.28	0.02	0.09	1.19	1.09	timt	
MAm-E-13_001	0.42	13.69	3.46	0.01	74.16	0.46	1.64	93.85	36.66	41.17	97.53	0.02	0.39	0.15	0.00	2.34	0.01	0.09	1.04	1.30	timt	
MAm-E-13_002	0.50	13.56	3.51	0.01	74.84	0.50	1.44	94.35	36.95	41.59	98.05	0.02	0.38	0.16	0.00	2.35	0.02	0.08	1.04	1.30	timt	
MAm-E-13_003	0.26	13.95	3.49	0.02	74.28	0.48	1.74	94.20	36.82	41.15	97.89	0.01	0.39	0.15	0.00	2.33	0.02	0.10	1.04	1.29	timt	
MAm-E-13_004	0.42	13.81	3.49	0.02	74.17	0.47	1.64	94.03	36.51	41.32	97.68	0.02	0.39	0.15	0.00	2.33	0.02	0.09	1.03	1.30	timt	
MAm-E-13_005	0.45	13.66	2.95	0.00	74.89	0.53	1.65	94.13	37.51	41.13	97.89	0.02	0.39	0.13	0.00	2.36	0.02	0.09	1.06	1.29	timt	
MAm-E-13_006	0.47	13.53	3.03	0.01	74.64	0.52	1.66	93.87	37.43	40.96	97.61	0.02	0.38	0.13	0.00	2.35	0.02	0.09	1.06	1.29	timt	
MAm-E-13_008	0.37	10.39	3.00	0.01	77.63	0.46	1.18	93.03	43.35	38.62	97.37	0.01	0.30	0.13	0.00	2.47	0.01	0.07	1.24	1.23	timt	
MAm-E-13_009	0.47	9.90	3.15	0.90	77.53	0.53	1.10	93.57	43.30	38.56	97.90	0.02	0.28	0.14	0.03	2.45	0.02	0.06	1.23	1.22	timt	
MAm-E-13_010	0.43	7.85	3.44	3.84	74.94	0.49	1.26	92.25	43.20	36.07	96.58	0.02	0.23	0.15	0.12	2.40	0.02	0.07	1.24	1.15	timt	
MAm-E-13_011	0.43	9.91	3.19	0.06	77.82	0.49	1.29	93.18	44.07	38.16	97.60	0.02	0.28	0.14	0.00	2.47	0.02	0.07	1.26	1.21	timt	
MAm-E-13_012	0.36	11.37	2.84	0.02	77.26	0.57	1.45	93.87	42.32	39.18	98.11	0.01	0.32	0.13	0.00	2.44	0.02	0.08	1.20	1.24	timt	
MAm-E-13_013	0.41	11.22	2.83	0.02	77.56	0.56	1.34	93.93	42.51	39.31	98.18	0.02	0.32	0.13	0.00	2.45	0.02	0.08	1.21	1.24	timt	
MAm-E-13_014	0.37	11.32	2.83	0.19	76.78	0.51	1.48	93.50	41.93	39.05	97.70	0.01	0.32	0.13	0.01	2.43	0.02	0.08	1.19	1.24	timt	
MAm-E-14_003	0.49	3.12	0.67	0.00	91.90	0.23	0.27	96.68	63.24	35.00	103.01	0.02	0.09	0.03	0.00	2.84	0.01	0.02	1.76	1.08	mt*	1
MAm-E-14_006	0.47	15.92	5.51	0.01	71.84	0.29	0.24	94.28	28.83	45.89	97.16	0.02	0.45	0.24	0.00	2.26	0.01	0.01	0.82	1.45	timt*	1
MAm-E-14_010	0.41	17.72	5.50	0.04	70.77	0.29	0.41	95.14	25.96	47.41	97.74	0.02	0.50	0.24	0.00	2.21	0.01	0.02	0.73	1.48	timt*	1
MAm-E-14_011	0.38	17.16	4.75	0.03	72.12	0.29	0.38	95.11	28.13	46.80	97.92	0.01	0.48	0.21	0.00	2.26	0.01	0.02	0.79	1.47	timt*	1
MAm-E-14_015	0.42	11.23	2.77	0.01	79.76	0.28	0.40	94.85	42.67	41.37	99.13	0.02	0.32	0.12	0.00	2.51	0.01	0.02	1.21	1.30	mt*	1
MAm-E-14_016	0.38	12.20	2.85	0.01	79.12	0.26	0.38	95.21	40.91	42.31	99.30	0.01	0.34	0.13	0.00	2.49	0.01	0.02	1.16	1.33	mt*	1
MAm-E-14_020	0.46	24.56	5.52	0.07	65.25	0.32	0.61	96.80	12.94	53.60	98.10	0.02	0.68	0.24	0.00	2.01	0.01	0.03	0.36	1.66	timt*	1
MAm-E-14_016a	0.38	10.03	2.39	0.01	82.08	0.22	0.39	95.51	46.20	40.51	100.13	0.01	0.28	0.11	0.00	2.57	0.01	0.02	1.30	1.27	mt*	1
MAm-E-14_016b	0.43	5.03	1.28	0.01	88.92	0.22	0.44	96.33	58.50	36.28	102.19	0.02	0.14	0.06	0.00	2.76	0.01	0.02	1.63	1.12	mt*	1
MAm-E-14_025a*	0.48	13.88	3.62	0.02	74.68	0.53	0.49	93.70	35.13	43.07	97.22	0.02	0.40	0.16	0.00	2.38	0.02	0.03	1.01	1.37	timt	
MAm-E-14_25a*	0.45	12.61	3.56	0.02	75.71	0.40	0.40	93.14	37.46	41.99	96.89	0.02	0.36	0.16	0.00	2.42	0.01	0.02	1.08	1.34	timt	
MAm-E-14_28a*	0.47	13.09	3.54	0.01	75.72	0.46	0.56	93.85	37.05	42.38	97.56	0.02	0.37	0.16	0.00	2.40	0.01	0.03	1.06	1.35	timt	
MAm-E-14_29a	0.41	13.01	2.94	0.00	75.68	0.53	0.50	93.08	37.53	41.91	96.84	0.02	0.38	0.13	0.00	2.43	0.02	0.03	1.08	1.35	timt	

Appendix H (Continued). Spinel Oxide Composition Data

Sample/spot[a]	SiO_2	TiO_2	Al_2O_3	Cr_2O_3	FeO(t)	MnO	MgO	Total	Fe_2O_3[b]	FeO[b]	Corr. Total[b]	Si	Ti	Al	Cr	Fe	Mn	Mg	Fe^{3+} [b]	Fe^{2+} [b]	Phase[c]	Exsolution types[d]
MAm-E-15_001	0.46	13.55	3.36	0.08	74.58	0.41	0.50	92.95	35.57	42.57	96.51	0.02	0.39	0.15	0.00	2.39	0.01	0.03	1.03	1.37	timt	
MAm-E-15_002	0.28	13.74	3.37	0.01	75.83	0.23	0.60	94.07	36.58	42.91	97.73	0.01	0.39	0.15	0.00	2.40	0.01	0.03	1.04	1.36	timt	
MAm-E-15_005	0.47	9.21	3.00	0.78	78.98	0.30	0.34	93.09	44.24	39.17	97.52	0.02	0.27	0.14	0.02	2.53	0.01	0.02	1.27	1.25	timt	
MAm-E-15_006	0.39	9.66	2.87	0.03	79.55	0.27	0.34	93.11	44.52	39.49	97.57	0.01	0.28	0.13	0.00	2.55	0.01	0.02	1.28	1.27	timt	
MAm-E-15_007	0.36	9.04	2.97	0.04	78.99	0.30	0.32	92.02	44.93	38.56	96.52	0.01	0.26	0.14	0.00	2.56	0.01	0.02	1.31	1.25	timt	
MAm-E-15_009	0.48	16.58	3.08	0.24	72.24	0.46	0.85	93.92	30.38	44.91	96.96	0.02	0.47	0.14	0.01	2.30	0.01	0.05	0.87	1.43	timt	
MAm-E-15_010	0.48	14.44	3.23	0.06	74.32	0.37	0.55	93.46	34.27	43.48	96.89	0.02	0.42	0.15	0.00	2.38	0.01	0.03	0.99	1.39	timt	
MAm-E-15_03a	0.48	13.70	2.97	0.05	74.70	0.46	0.36	92.73	35.49	42.77	96.28	0.02	0.40	0.14	0.00	2.41	0.02	0.02	1.03	1.38	timt	
MAm-E-15_11	0.48	6.40	4.65	1.49	76.83	0.48	2.10	92.42	47.73	33.88	97.20	0.02	0.18	0.21	0.04	2.42	0.02	0.12	1.35	1.07	timt	
MB2-48_5-1-1	0.47	16.46	3.29	0.37	67.45	1.27	4.91	94.23	32.80	37.93	97.52	0.02	0.45	0.14	0.01	2.07	0.04	0.27	0.90	1.16	timt	
MB2-48_2-2-1	0.49	16.90	3.36	2.11	65.49	1.31	4.73	94.40	29.88	38.61	97.39	0.02	0.47	0.15	0.06	2.01	0.04	0.26	0.82	1.18	timt	
MB2-48_6-1-1	0.48	16.33	3.23	0.97	67.19	1.37	4.90	94.47	32.63	37.82	97.73	0.02	0.45	0.14	0.03	2.06	0.04	0.27	0.90	1.16	timt	
MB2-48_4_1	0.48	17.10	3.40	1.38	65.48	1.27	4.80	93.92	29.91	38.56	96.92	0.02	0.47	0.15	0.04	2.02	0.04	0.26	0.83	1.19	timt	
MB2-48_2_1	0.47	17.02	3.41	1.22	66.08	1.28	4.80	94.28	30.53	38.61	97.34	0.02	0.47	0.15	0.04	2.03	0.04	0.26	0.84	1.18	timt	
MB2-48_2_2	0.50	16.59	3.42	2.10	64.93	1.24	4.91	93.69	30.00	37.93	96.69	0.02	0.46	0.15	0.06	2.00	0.04	0.27	0.83	1.17	timt	
MB2-48_3_1	0.41	17.38	3.47	1.45	66.70	1.28	4.75	95.43	30.44	39.32	98.48	0.02	0.47	0.15	0.04	2.02	0.04	0.26	0.83	1.19	timt	
MB2-48_1-01	0.49	17.19	3.42	1.34	65.89	1.26	4.67	94.25	29.89	38.99	97.25	0.02	0.48	0.15	0.04	2.02	0.04	0.26	0.83	1.20	timt	
MB2-48_4_2	0.42	16.37	3.55	3.50	64.91	1.28	4.83	94.86	29.78	38.11	97.85	0.02	0.45	0.15	0.10	1.98	0.04	0.26	0.82	1.16	timt	
MB2-48_5_1*	0.50	16.22	3.33	0.71	66.08	1.36	4.82	93.02	31.87	37.41	96.21	0.02	0.45	0.15	0.02	2.05	0.04	0.27	0.89	1.16	timt	
MB2-48_5_2	0.40	16.45	3.29	0.96	66.81	1.37	4.72	94.00	32.07	37.95	97.21	0.01	0.46	0.14	0.03	2.06	0.04	0.26	0.89	1.17	timt	
MB2-48_2-01	0.44	16.15	3.53	1.53	66.98	1.39	4.94	94.95	32.51	37.73	98.21	0.02	0.44	0.15	0.04	2.04	0.04	0.27	0.89	1.15	timt	
MB2-48_2-02	0.40	16.25	3.49	0.90	67.48	1.34	5.04	94.89	33.18	37.63	98.21	0.01	0.44	0.15	0.03	2.05	0.04	0.27	0.91	1.14	timt	
MB2-48_01*	0.45	17.10	3.39	0.72	67.13	1.28	4.76	94.82	31.40	38.88	97.97	0.02	0.47	0.15	0.02	2.05	0.04	0.26	0.86	1.19	timt	
MB2-48_02	0.46	16.77	3.41	0.75	66.83	1.31	4.69	94.23	31.50	38.49	97.38	0.02	0.46	0.15	0.02	2.05	0.04	0.26	0.87	1.18	timt	
MB2-48_03	0.49	17.20	3.38	0.60	67.03	1.37	4.82	94.90	31.30	38.87	98.03	0.02	0.47	0.15	0.02	2.04	0.04	0.26	0.86	1.19	timt	
MB2-48_04	0.48	16.47	3.38	1.66	65.43	1.36	4.87	93.64	30.80	37.72	96.72	0.02	0.46	0.15	0.05	2.02	0.04	0.27	0.86	1.16	timt	
MB2-E-09_3-1	0.47	16.53	3.40	5.45	61.74	1.13	4.35	93.07	25.80	38.52	95.66	0.02	0.46	0.15	0.16	1.93	0.04	0.24	0.73	1.20	timt	
MB2-E-09_3-2	0.42	15.86	3.59	6.87	61.69	1.26	4.54	94.22	26.48	37.86	96.87	0.02	0.44	0.16	0.20	1.90	0.04	0.25	0.73	1.17	timt	
MB2-E-09_9-1	0.38	15.89	3.53	4.56	65.06	1.21	4.39	95.02	29.62	38.40	97.99	0.01	0.44	0.15	0.13	1.99	0.04	0.24	0.81	1.17	timt	
MB2-E-09_9-2	0.39	16.03	3.69	3.59	63.00	1.18	4.63	92.49	28.45	37.39	95.34	0.01	0.45	0.16	0.11	1.97	0.04	0.26	0.80	1.17	timt	
MB2-E-09_7-1	0.45	17.74	3.24	0.66	63.86	1.19	4.11	91.25	27.27	39.32	93.98	0.02	0.51	0.15	0.02	2.04	0.04	0.23	0.78	1.25	timt	
MB2-E-09_7-1_2	0.42	17.56	3.12	0.75	66.74	1.16	4.47	94.21	30.19	39.57	97.24	0.02	0.49	0.14	0.02	2.06	0.04	0.25	0.84	1.22	timt	
MB2-E-09_2-1_2	0.47	16.51	3.34	3.72	63.76	1.24	4.43	93.46	28.14	38.44	96.28	0.02	0.46	0.15	0.11	1.98	0.04	0.25	0.79	1.19	timt	
MB2-E-09_3-1_2	0.40	16.66	3.47	5.90	62.39	1.21	4.63	94.67	26.46	38.59	97.32	0.01	0.46	0.15	0.17	1.91	0.04	0.25	0.73	1.18	timt	
MB2-E-09_3-2_2	0.44	15.99	3.67	6.83	61.46	1.14	4.70	94.23	26.22	37.87	96.86	0.02	0.44	0.16	0.20	1.89	0.04	0.26	0.73	1.16	timt	
MB2-E-09_1-4a	0.39	18.01	3.24	3.31	64.49	1.21	4.54	95.17	27.13	40.07	97.89	0.01	0.50	0.14	0.10	1.97	0.04	0.25	0.75	1.22	timt	
MB2-E-09_5-2a	0.47	18.23	3.25	2.63	64.88	1.20	4.37	95.03	26.99	40.59	97.73	0.02	0.50	0.14	0.08	1.99	0.04	0.24	0.74	1.24	timt	
MB2-E-09_1-3a	0.46	17.75	3.17	1.90	65.94	1.23	4.50	94.95	28.94	39.90	97.85	0.02	0.49	0.14	0.06	2.02	0.04	0.25	0.80	1.22	timt	

Appendix H (Continued). Spinel Oxide Composition Data

Sample/spot[a]	SiO_2	TiO_2	Al_2O_3	Cr_2O_3	FeO(t)	MnO	MgO	Total	Fe_2O_3[b]	FeO[b]	Corr. Total[b]	Si	Ti	Al	Cr	Fe	Mn	Mg	Fe^{3+} [b]	Fe^{2+} [b]	Phase[c]	Exsolution types[d]
MB2-E-10_1-2	0.45	17.81	3.17	2.79	62.17	1.04	4.36	91.79	25.45	39.27	94.34	0.02	0.51	0.14	0.08	1.97	0.03	0.25	0.73	1.24	timt	
MB2-E-10_3-3	0.44	17.53	3.28	3.18	62.64	1.12	3.96	92.14	25.52	39.68	94.70	0.02	0.50	0.15	0.10	1.98	0.04	0.22	0.73	1.26	timt	
MB2-E-10_4-2	0.41	17.43	3.41	3.27	63.29	1.23	4.80	93.84	27.27	38.75	96.57	0.02	0.48	0.15	0.10	1.95	0.04	0.26	0.76	1.20	timt	
MB2-E-10_4-5	0.41	17.93	3.25	3.02	63.28	1.21	4.55	93.65	26.44	39.50	96.30	0.02	0.50	0.14	0.09	1.96	0.04	0.25	0.74	1.23	timt	
MB2-E-10_4-5_2	0.46	17.81	3.42	3.03	64.05	1.18	4.38	94.33	26.74	39.99	97.00	0.02	0.49	0.15	0.09	1.97	0.04	0.24	0.74	1.23	timt	
MB2-E-10_6-1	0.43	18.29	2.95	0.26	66.77	1.22	4.19	94.11	29.15	40.54	97.03	0.02	0.51	0.13	0.01	2.07	0.04	0.23	0.81	1.26	timt	
MB2-E-10_6-1_2	0.41	18.52	2.95	0.30	66.74	1.27	4.26	94.45	28.96	40.68	97.35	0.02	0.51	0.13	0.01	2.06	0.04	0.23	0.80	1.26	timt	
MB2-E-10_9-2	0.45	17.64	3.17	0.36	67.01	1.16	3.26	93.07	28.73	41.16	95.94	0.02	0.50	0.14	0.01	2.11	0.04	0.18	0.81	1.30	timt	
MB2-E-10_9-2_2	0.44	17.57	3.15	0.35	67.68	1.15	3.51	93.87	29.68	40.97	96.84	0.02	0.49	0.14	0.01	2.11	0.04	0.20	0.83	1.28	timt	
MB2-E-10_5-4	0.49	17.37	3.08	0.79	66.95	1.22	4.21	94.12	30.17	39.80	97.15	0.02	0.48	0.13	0.02	2.07	0.04	0.23	0.84	1.23	timt	
MB2-E-10_5-5	0.45	17.00	2.98	1.40	67.33	1.16	3.48	93.79	29.85	40.47	96.78	0.02	0.48	0.13	0.04	2.10	0.04	0.19	0.84	1.26	timt	
MB2-E-10_5-6	0.49	16.72	3.13	0.60	66.64	1.10	4.14	92.84	30.67	39.05	95.91	0.02	0.47	0.14	0.02	2.09	0.04	0.23	0.86	1.22	timt	
MB2-E-10_8-2	0.50	17.07	2.95	1.34	67.68	1.15	3.15	93.84	29.52	41.12	96.80	0.02	0.48	0.13	0.04	2.12	0.04	0.18	0.83	1.29	timt	
MB2-E-10_10-1	0.48	15.18	3.42	1.21	67.02	1.29	4.84	93.45	33.71	36.68	96.82	0.02	0.42	0.15	0.04	2.07	0.04	0.27	0.94	1.13	timt	
MB2-E-10_10-3	0.48	15.22	3.28	1.11	68.44	1.23	3.42	93.18	32.91	38.82	96.47	0.02	0.43	0.14	0.03	2.15	0.04	0.19	0.93	1.22	timt	
MB2-E-10_10-7	0.50	15.13	3.20	1.24	67.67	1.22	3.72	92.69	32.82	38.14	95.98	0.02	0.43	0.14	0.04	2.13	0.04	0.21	0.93	1.20	timt	
MB2-E-10_12-3	0.49	16.40	3.29	1.02	67.17	1.15	4.04	93.57	31.17	39.12	96.69	0.02	0.46	0.14	0.03	2.09	0.04	0.22	0.87	1.22	timt	
MB2-E-10_12-4_2	0.45	16.21	3.25	0.96	67.86	1.22	3.76	93.70	31.74	39.31	96.88	0.02	0.45	0.14	0.03	2.11	0.04	0.21	0.89	1.22	timt	
MB2-E-10_12-13	0.45	16.19	3.22	1.09	67.53	1.19	3.94	93.62	31.69	39.02	96.79	0.02	0.45	0.14	0.03	2.10	0.04	0.22	0.89	1.21	timt	
MB2-E-10_12-14	0.44	16.26	3.19	0.97	68.06	1.26	3.63	93.82	31.70	39.54	96.99	0.02	0.46	0.14	0.03	2.12	0.04	0.20	0.89	1.23	timt	
MB2-E-11_6-1	0.31	12.88	4.71	20.05	52.39	1.17	3.87	95.38	17.62	36.54	97.14	0.01	0.35	0.20	0.58	1.60	0.04	0.21	0.49	1.12	chr	
MB2-E-11_6-2	0.31	3.52	13.03	36.64	37.04	1.04	4.78	96.37	9.65	28.36	97.34	0.01	0.09	0.53	1.01	1.08	0.03	0.25	0.25	0.82	chr	
MB2-E-11_6-3	0.37	16.19	3.79	13.33	57.05	1.17	3.91	95.80	19.43	39.56	97.74	0.01	0.44	0.16	0.39	1.74	0.04	0.21	0.53	1.21	chr	
MB2-E-11_6-5	0.29	15.52	3.93	14.50	56.20	1.11	3.86	95.40	19.24	38.89	97.33	0.01	0.43	0.17	0.42	1.72	0.03	0.21	0.53	1.19	chr	
MB2-E-11_4-1	0.34	12.33	4.55	13.74	57.68	1.04	4.22	93.90	24.86	35.30	96.39	0.01	0.34	0.20	0.40	1.78	0.03	0.23	0.69	1.09	chr	
MB2-E-11_4-2	0.31	8.35	6.04	22.58	51.24	1.05	4.50	94.07	21.97	31.48	96.27	0.01	0.23	0.26	0.65	1.57	0.03	0.25	0.60	0.96	chr	
MB2-E-11_4-3	0.32	4.31	9.78	31.35	42.85	0.98	4.98	94.58	16.67	27.85	96.25	0.01	0.12	0.41	0.89	1.28	0.03	0.27	0.45	0.83	chr	
MB2-E-11_4-4	0.36	1.76	15.52	35.57	35.64	0.93	5.85	95.62	11.30	25.47	96.75	0.01	0.05	0.63	0.97	1.02	0.03	0.30	0.29	0.73	chr	
MB2-E-11_4-5	0.35	1.14	17.62	37.12	32.70	0.98	6.18	96.09	8.79	24.79	96.97	0.01	0.03	0.70	0.99	0.92	0.03	0.31	0.22	0.70	chr	
MB2-E-11_4-6	0.37	1.03	18.09	38.05	32.32	0.97	6.25	97.07	8.12	25.01	97.89	0.01	0.03	0.71	1.01	0.90	0.03	0.31	0.20	0.70	chr	
MB2-E-11_4-7	0.36	1.02	18.44	37.64	31.79	0.93	6.30	96.48	7.75	24.81	97.25	0.01	0.03	0.73	1.00	0.89	0.03	0.32	0.20	0.70	chr	
MB2-E-11_4-8	0.41	15.25	3.73	7.49	61.54	1.06	4.12	93.58	26.21	37.95	96.21	0.02	0.43	0.16	0.22	1.91	0.03	0.23	0.73	1.18	chr	
MB2-E-11_3	0.38	17.71	3.34	2.20	66.02	1.03	4.00	94.68	28.18	40.66	97.50	0.01	0.49	0.15	0.06	2.03	0.03	0.22	0.78	1.25	timt	
MB2-E-11_1-1	0.48	17.66	3.32	3.72	64.71	1.05	3.86	94.80	26.42	40.94	97.44	0.02	0.49	0.14	0.11	2.00	0.03	0.21	0.73	1.26	timt	
MB2-E-11_1-3	0.50	14.14	3.88	9.05	60.05	1.08	4.00	92.69	25.65	36.97	95.26	0.02	0.40	0.17	0.27	1.88	0.03	0.22	0.72	1.16	timt	
MB2-E-11_1-4	0.47	18.06	3.26	3.19	64.25	1.07	3.92	94.21	25.87	40.97	96.80	0.02	0.50	0.14	0.09	1.99	0.03	0.22	0.72	1.27	timt	
MB2-E-11_2-1	0.43	17.93	3.29	3.46	64.28	1.08	3.78	94.25	25.85	41.02	96.84	0.02	0.50	0.14	0.10	2.00	0.03	0.21	0.72	1.27	timt	
MB2-E-11_2-3	0.48	18.40	3.18	1.78	65.40	1.05	3.37	93.67	26.03	41.98	96.28	0.02	0.52	0.14	0.05	2.05	0.03	0.19	0.73	1.31	timt	

Appendix H (Continued). Spinel Oxide Composition Data

Sample/spot[a]	SiO_2	TiO_2	Al_2O_3	Cr_2O_3	FeO(t)	MnO	MgO	Total	Fe_2O_3[b]	FeO[b]	Corr. Total[b]	Si	Ti	Al	Cr	Fe	Mn	Mg	Fe^{3+} [b]	Fe^{2+} [b]	Phase[c]	Exsolution types[d]
MB2-E-11_10-1	0.29	1.45	17.63	39.91	31.66	0.93	5.48	97.34	5.75	26.48	97.92	0.01	0.04	0.70	1.06	0.89	0.03	0.27	0.15	0.75	chr	
MB2-E-11_10-2	0.35	1.53	17.44	38.96	31.91	0.92	5.47	96.58	6.15	26.37	97.20	0.01	0.04	0.70	1.04	0.90	0.03	0.28	0.16	0.75	chr	
MB2-E-11_10-3	0.29	1.71	17.04	38.29	32.96	0.89	5.35	96.54	7.04	26.62	97.24	0.01	0.04	0.68	1.03	0.94	0.03	0.27	0.18	0.76	chr	
MB2-E-11_10-4	0.34	3.28	14.15	36.24	36.14	0.98	5.03	96.15	9.11	27.95	97.06	0.01	0.09	0.58	0.99	1.05	0.03	0.26	0.24	0.81	chr	
MB2-E-11_10-5	0.32	5.86	10.37	32.80	40.28	1.02	4.56	95.22	11.35	30.06	96.36	0.01	0.16	0.44	0.92	1.20	0.03	0.24	0.30	0.90	chr	
MB2-E-11_10-6	0.31	10.62	5.74	24.95	48.50	1.02	4.15	95.28	15.74	34.33	96.86	0.01	0.29	0.25	0.72	1.48	0.03	0.23	0.43	1.05	chr	
MB2-E-11_10-7	0.35	15.22	4.03	15.78	54.16	1.13	4.09	94.77	17.84	38.11	96.55	0.01	0.42	0.18	0.46	1.67	0.04	0.22	0.49	1.18	chr	
MB2-E-11_10-8	0.31	16.57	3.77	13.51	56.32	1.18	4.05	95.70	18.63	39.55	97.56	0.01	0.46	0.16	0.39	1.72	0.04	0.22	0.51	1.21	chr	
MB2-E-11_10-9	0.36	18.09	3.45	10.60	57.66	1.13	4.06	95.35	18.69	40.85	97.23	0.01	0.50	0.15	0.31	1.77	0.04	0.22	0.52	1.26	chr	
MB2-E-11_10-10	0.39	18.60	3.27	9.50	58.70	1.13	3.95	95.54	19.05	41.56	97.45	0.01	0.51	0.14	0.28	1.80	0.04	0.22	0.53	1.28	chr	
MB2-E-11_10-11	0.45	18.76	3.30	8.69	58.47	1.11	3.60	94.38	18.35	41.96	96.22	0.02	0.53	0.14	0.26	1.82	0.03	0.20	0.51	1.31	chr	
MB2-E-11_9-1	0.42	16.42	3.42	6.29	62.80	1.03	3.75	94.14	25.64	39.72	96.70	0.02	0.46	0.15	0.18	1.95	0.03	0.21	0.72	1.23	timt	
MB2-E-11_9-2	0.35	12.95	4.27	14.88	57.72	1.03	4.00	95.19	23.50	36.57	97.55	0.01	0.36	0.18	0.43	1.77	0.03	0.22	0.65	1.12	timt	
MB2-E-11_6-1_2	0.32	1.77	16.96	38.85	33.33	1.02	5.19	97.44	6.93	27.09	98.14	0.01	0.04	0.68	1.04	0.94	0.03	0.26	0.18	0.77	chr	
MB2-E-11_10-1_2	0.32	1.46	17.71	39.77	31.57	0.95	5.53	97.31	5.71	26.44	97.88	0.01	0.04	0.70	1.06	0.89	0.03	0.28	0.14	0.74	chr	
MB2-E-11_10-5_2	0.31	1.59	17.38	38.66	32.37	0.90	5.42	96.62	6.55	26.48	97.27	0.01	0.04	0.69	1.04	0.92	0.03	0.27	0.17	0.75	chr	
MB2-E-12_002	0.43	18.43	3.19	1.90	65.77	1.34	3.77	94.83	27.07	41.42	97.54	0.02	0.51	0.14	0.06	2.03	0.04	0.21	0.75	1.28	timt	
MB2-E-12_003	0.39	16.79	3.42	5.04	64.12	1.07	3.72	94.55	26.61	40.18	97.21	0.01	0.47	0.15	0.15	1.98	0.03	0.20	0.74	1.24	timt	
MB2-E-12_004	0.32	12.85	4.17	13.77	58.66	1.06	4.16	94.99	25.06	36.11	97.50	0.01	0.35	0.18	0.40	1.80	0.03	0.23	0.69	1.11	timt	
MB2-E-12_005	0.46	16.99	3.37	3.24	65.45	1.16	3.26	93.93	27.32	40.87	96.67	0.02	0.48	0.15	0.10	2.04	0.04	0.18	0.77	1.28	timt	
MB2-E-12_006	0.41	17.84	3.03	1.05	67.24	1.20	3.51	94.27	28.92	41.22	97.16	0.02	0.50	0.13	0.03	2.09	0.04	0.19	0.81	1.28	timt	
MB2-E-12_007	0.37	17.18	3.23	3.13	66.44	1.14	3.85	95.34	28.82	40.50	98.23	0.01	0.47	0.14	0.09	2.04	0.04	0.21	0.80	1.24	timt	
MB2-E-12_010	0.48	16.34	3.34	2.17	66.22	1.21	4.03	93.79	30.18	39.07	96.81	0.02	0.46	0.15	0.06	2.06	0.04	0.22	0.84	1.21	timt	
MB2-E-12_011	0.43	15.77	3.34	2.29	67.24	1.16	3.56	93.79	31.07	39.27	96.90	0.02	0.44	0.15	0.07	2.09	0.04	0.20	0.87	1.22	timt	
MB2-E-12_014	0.45	16.31	3.33	1.90	66.66	1.10	4.00	93.73	30.56	39.16	96.79	0.02	0.46	0.15	0.06	2.07	0.03	0.22	0.85	1.22	timt	
MB2-E-12_017	0.46	16.11	3.21	0.67	69.40	1.14	2.89	93.87	31.90	40.69	97.07	0.02	0.45	0.14	0.02	2.17	0.04	0.16	0.90	1.27	timt	
MB2-E-12_018	0.46	16.35	3.28	1.42	67.20	1.22	3.53	93.46	30.55	39.71	96.52	0.02	0.46	0.14	0.04	2.10	0.04	0.20	0.86	1.24	timt	
MB2-E-12_019	0.47	16.08	3.23	1.77	66.91	1.21	4.04	93.70	31.25	38.78	96.83	0.02	0.45	0.14	0.05	2.08	0.04	0.22	0.87	1.20	timt	
MB2-E-12_020	0.50	15.89	3.17	1.69	67.09	1.28	3.77	93.39	31.35	38.88	96.53	0.02	0.45	0.14	0.05	2.10	0.04	0.21	0.88	1.21	timt	
MB2-E-13_001	0.46	16.89	3.34	4.96	62.41	1.16	3.81	93.03	25.34	39.61	95.57	0.02	0.48	0.15	0.15	1.96	0.04	0.21	0.72	1.24	timt	
MB2-E-13_003	0.46	17.62	3.16	3.48	64.24	1.21	3.86	94.05	26.44	40.45	96.69	0.02	0.49	0.14	0.10	2.00	0.04	0.21	0.74	1.26	timt	
MB2-E-13_004*	0.37	15.30	3.57	8.38	61.75	1.07	4.15	94.60	26.19	38.18	97.22	0.01	0.42	0.16	0.24	1.90	0.03	0.23	0.73	1.18	timt	
MB2-E-13_005*	0.45	18.52	3.00	3.05	64.95	1.15	3.59	94.71	25.61	41.91	97.28	0.02	0.52	0.13	0.09	2.01	0.04	0.20	0.71	1.30	timt	
MB2-E-13_006	0.41	18.28	3.12	3.45	64.16	1.17	3.73	94.33	25.42	41.29	96.88	0.02	0.51	0.14	0.10	1.99	0.04	0.21	0.71	1.28	timt	
MB2-E-13_007	0.37	17.08	3.29	4.89	63.74	1.15	3.68	94.21	26.10	40.25	96.82	0.01	0.48	0.14	0.14	1.98	0.04	0.20	0.73	1.25	timt	

Appendix H (Continued). Spinel Oxide Composition Data

Sample/spot[a]	SiO_2	TiO_2	Al_2O_3	Cr_2O_3	FeO(t)	MnO	MgO	Total	Fe_2O_3[b]	FeO[b]	Corr. Total[b]	Si	Ti	Al	Cr	Fe	Mn	Mg	Fe^{3+} [b]	Fe^{2+} [b]	Phase[c]	Exsolution types[d]
MB2-E-13_008	0.34	14.64	3.81	9.73	60.92	1.15	4.09	94.69	25.88	37.63	97.28	0.01	0.41	0.17	0.28	1.87	0.04	0.22	0.72	1.16	timt	
MB2-E-13_009	0.46	17.75	3.18	2.98	65.30	1.13	3.40	94.21	26.55	41.41	96.87	0.02	0.50	0.14	0.09	2.03	0.04	0.19	0.74	1.29	timt	
MB2-E-13_010	0.36	10.00	5.23	17.90	54.89	1.14	4.57	94.08	24.60	32.75	96.55	0.01	0.28	0.23	0.52	1.68	0.04	0.25	0.68	1.00	timt	
MB2-E-13_011	0.49	18.45	2.94	1.04	67.08	1.25	2.99	94.24	27.24	42.57	96.96	0.02	0.52	0.13	0.03	2.10	0.04	0.17	0.77	1.33	timt	
MB2-E-13_012	0.46	19.22	2.88	0.40	66.68	1.22	3.72	94.57	27.15	42.25	97.29	0.02	0.54	0.13	0.01	2.07	0.04	0.21	0.76	1.31	timt	
MB2-E-13_013	0.39	17.45	3.12	3.56	64.67	1.22	3.93	94.34	27.20	40.19	97.06	0.01	0.49	0.14	0.10	2.00	0.04	0.22	0.76	1.25	timt	
MB2-E-13_014	0.41	17.56	3.11	3.44	64.11	1.46	4.05	94.14	27.00	39.82	96.84	0.02	0.49	0.14	0.10	1.99	0.05	0.22	0.75	1.24	timt	
MB2-E-14_01a	0.49	15.22	3.51	1.01	68.49	1.42	3.42	93.56	33.00	38.79	96.86	0.02	0.43	0.15	0.03	2.14	0.04	0.19	0.93	1.21	timt	
MB2-E-14_12	0.47	15.46	3.37	0.86	68.42	1.33	3.74	93.65	33.14	38.60	96.97	0.02	0.43	0.15	0.03	2.13	0.04	0.21	0.93	1.20	timt	
MB2-E-14_04a	0.50	15.64	3.52	1.09	70.66	1.19	1.26	93.86	30.96	42.80	96.96	0.02	0.45	0.16	0.03	2.24	0.04	0.07	0.88	1.35	timt	
MB2-E-14_10a	0.48	13.12	4.55	10.80	59.19	1.22	4.37	93.74	26.07	35.74	96.35	0.02	0.36	0.20	0.32	1.83	0.04	0.24	0.72	1.10	timt	
MB2-E-15_001	0.35	17.10	3.06	4.67	63.62	1.38	3.52	93.70	26.17	40.07	96.33	0.01	0.48	0.14	0.14	1.99	0.04	0.20	0.74	1.25	timt	
MB2-E-15_002	0.37	15.07	3.35	6.22	64.08	1.26	3.26	93.59	28.07	38.82	96.41	0.01	0.42	0.15	0.18	2.01	0.04	0.18	0.79	1.22	timt	
MB2-E-15_003	0.44	15.74	2.92	0.80	70.27	1.21	1.58	92.96	31.51	41.92	96.11	0.02	0.45	0.13	0.02	2.25	0.04	0.09	0.91	1.34	timt	
MB2-E-15_005	0.40	16.11	2.85	0.55	70.27	1.12	2.04	93.33	31.74	41.71	96.51	0.02	0.46	0.13	0.02	2.23	0.04	0.12	0.91	1.32	timt	
MB2-E-15_006	0.40	15.49	2.95	1.53	71.29	0.71	1.07	93.43	31.35	43.08	96.57	0.02	0.44	0.13	0.05	2.28	0.02	0.06	0.90	1.38	timt	
MB2-E-15_007	0.41	17.18	2.82	1.09	68.86	1.41	2.29	94.05	29.64	42.19	97.02	0.02	0.49	0.13	0.03	2.17	0.05	0.13	0.84	1.33	timt	
MB2-E-15_008	0.33	16.94	2.77	0.82	69.72	1.37	2.47	94.42	31.04	41.79	97.53	0.01	0.48	0.12	0.02	2.18	0.04	0.14	0.87	1.31	timt	
MB2-E-15_011	0.39	20.01	3.12	7.44	60.44	1.21	2.67	95.28	17.63	44.57	97.04	0.01	0.56	0.14	0.22	1.88	0.04	0.15	0.49	1.39	timt	
MB2-E-15_012	0.36	15.01	3.93	14.87	56.37	1.10	2.92	94.56	18.54	39.68	96.42	0.01	0.42	0.17	0.44	1.76	0.03	0.16	0.52	1.24	timt	
MB2-E-15_013	0.39	15.66	3.83	12.61	57.53	1.14	3.12	94.27	19.61	39.88	96.24	0.01	0.44	0.17	0.37	1.80	0.04	0.17	0.55	1.24	timt	

Oxides in wt.%, cations in atoms per unit formula with 4 oxygen basis.

[a] Shaded samples/spots bounded with dotted lines indicate that they are the analyses within the same oxide grains. The spots also analyzed by Raman spectroscopy are denoted with asterisk. The samples MAm-E -12, 13, 15, MB2-E-12, 14 were also analyzed, but on grains not analyzed by EPMA. Some spots within the second grain in MAm-E-14 were also analyzed but not the same spots as EPMA. More analyses were conducted for other grains than those analyzed by EPMA for MB2-48 and MB2-E-13.

[b] FeO(t) was differentiated into Fe_2O_3 and FeO using a technique of Droop (1987), and corrected total was obtained.

[c] Phase abbreviations: femgal=Fe-Mg-Al spinel oxide, mt=magnetite, femg=Fe-Mg spinel oxide, mgf=magnesioferrite, timt=titanomagnetite, chr=chromite. *=exsolved phases.

[d] Exsolution types: (1) magnetite - Al-bearing titanomagnetite, (2) Fe-Mg-Al spinel oxide - Fe-Mg spinel oxide, (3) Fe-Mg-Al spinel oxide - Al-bearing magnesioferrite.

Sample/spot	SiO_2	TiO_2	Al_2O_3	Cr_2O_3	FeO(t)	MnO	MgO	Total	Fe_2O_3[a]	FeO[a]	Corr. Total[a]	Si	Ti	Al	Cr	Fe	Mn	Mg	Fe^{3+} [a]	Fe^{2+} [a]	Phase[b]
MAm-36_in_01b*	0.43	6.29	1.62	0.21	76.01	0.52	2.55	87.63	83.26	1.09	95.97	0.01	0.13	0.05	0.00	1.69	0.01	0.10	1.67	0.02	hem
MAm-36_in_02b	0.46	6.88	1.70	0.26	74.93	0.61	2.82	87.67	82.05	1.10	95.88	0.01	0.14	0.05	0.01	1.67	0.01	0.11	1.64	0.02	hem
MAm-36_in_03b*	0.39	6.55	1.63	0.14	74.94	0.60	2.60	86.85	82.05	1.11	95.06	0.01	0.13	0.05	0.00	1.68	0.01	0.10	1.66	0.02	hem
MAm-36_in_04b*	0.45	6.16	1.75	1.09	74.73	0.53	2.47	87.16	81.77	1.15	95.35	0.01	0.12	0.06	0.02	1.67	0.01	0.10	1.65	0.03	hem
MAm-36_in_05b*	0.31	6.42	1.85	0.31	75.93	0.57	2.38	87.77	82.92	1.32	96.08	0.01	0.13	0.06	0.01	1.69	0.01	0.09	1.66	0.03	hem
MAm-36_in_06b*	0.44	4.15	1.75	1.05	77.47	0.38	1.62	86.85	84.99	0.99	95.36	0.01	0.08	0.06	0.02	1.75	0.01	0.07	1.73	0.02	hem
MAm-36_in_07b	0.44	5.06	1.94	0.25	76.33	0.61	2.06	86.71	83.96	0.78	95.11	0.01	0.10	0.06	0.01	1.72	0.01	0.08	1.70	0.02	hem
MAm-36_in_12b*	0.49	4.44	1.80	0.60	77.15	0.50	1.77	86.74	84.70	0.93	95.23	0.01	0.09	0.06	0.01	1.74	0.01	0.07	1.72	0.02	hem
MAm-36_in_26b	0.39	3.92	1.94	1.37	77.58	0.56	1.63	87.39	85.64	0.52	95.97	0.01	0.08	0.06	0.03	1.74	0.01	0.07	1.73	0.01	hem
MB2-31_004*	0.31	6.03	1.76	1.25	74.83	0.49	2.04	86.71	81.32	1.65	94.85	0.01	0.12	0.06	0.03	1.69	0.01	0.08	1.66	0.04	hem
MB2-31_007*	0.49	11.23	1.44	0.35	69.00	0.65	3.93	87.11	73.32	3.02	94.46	0.01	0.23	0.05	0.01	1.54	0.01	0.16	1.47	0.07	hem
MB2-31_010*	0.33	6.20	1.80	2.01	73.94	0.52	2.28	87.08	80.65	1.37	95.16	0.01	0.13	0.06	0.04	1.66	0.01	0.09	1.63	0.03	hem
MB2-31_012	0.33	7.51	1.78	0.44	73.83	0.51	2.33	86.73	79.29	2.48	94.67	0.01	0.15	0.06	0.01	1.67	0.01	0.09	1.61	0.06	hem
MB2-48-5-1-2	0.41	44.32	0.58	0.13	44.53	1.17	5.54	96.68	16.95	29.28	98.37	0.01	0.82	0.02	0.00	0.92	0.02	0.20	0.31	0.60	ilm
MB2-48-5-2-1	0.48	44.72	0.60	0.06	44.22	1.18	5.57	96.83	16.17	29.66	98.45	0.01	0.83	0.02	0.00	0.91	0.02	0.20	0.30	0.61	ilm
MB2-48-4-1-1	0.44	45.95	0.58	0.31	43.02	1.15	5.51	96.96	13.52	30.85	98.31	0.01	0.85	0.02	0.01	0.89	0.02	0.20	0.25	0.64	ilm
MB2-48-2-1-1	0.43	45.36	0.53	0.35	43.44	1.14	5.53	96.76	14.61	30.29	98.23	0.01	0.84	0.02	0.01	0.90	0.02	0.20	0.27	0.63	ilm
MB2-48-6-1-2	0.42	44.75	0.56	0.20	44.41	1.23	5.57	97.15	16.51	29.55	98.80	0.01	0.83	0.02	0.00	0.91	0.03	0.20	0.31	0.61	ilm
MB2-E-09_2-1	0.39	46.02	0.65	0.59	42.85	1.10	5.14	96.73	12.53	31.57	97.99	0.01	0.86	0.02	0.01	0.89	0.02	0.19	0.23	0.65	ilm
MB2-E-09_7-2_2	0.45	45.76	0.54	0.08	43.45	1.09	5.43	96.80	13.94	30.91	98.20	0.01	0.85	0.02	0.00	0.90	0.02	0.20	0.26	0.64	ilm
MB2-E-09_2-2_2	0.41	45.69	0.68	0.55	42.41	1.05	5.48	96.27	12.95	30.75	97.57	0.01	0.85	0.02	0.01	0.88	0.02	0.20	0.24	0.64	ilm
MB2-E-09_10-3_2	0.43	46.28	0.59	0.08	43.11	1.19	5.30	96.98	12.94	31.46	98.28	0.01	0.86	0.02	0.00	0.89	0.02	0.20	0.24	0.65	ilm
MB2-E-09_4-4_2	0.44	47.81	0.54	0.10	42.33	1.20	5.44	97.85	10.80	32.61	98.93	0.01	0.88	0.02	0.00	0.87	0.02	0.20	0.20	0.67	ilm
MB2-E-10_1-3	0.46	44.99	0.51	0.43	40.73	1.03	4.64	92.79	10.05	31.69	93.80	0.01	0.88	0.02	0.01	0.88	0.02	0.18	0.20	0.69	ilm
MB2-E-10_7-1	0.37	46.66	0.51	0.11	43.28	1.15	5.27	97.35	12.73	31.83	98.63	0.01	0.86	0.01	0.00	0.89	0.02	0.19	0.24	0.66	ilm
MB2-E-10_7-4	0.44	46.03	0.51	0.07	43.82	1.21	5.21	97.31	13.81	31.40	98.69	0.01	0.85	0.01	0.00	0.90	0.03	0.19	0.26	0.65	ilm
MB2-E-10_6-3	0.32	46.21	0.54	0.08	43.86	1.13	5.00	97.12	13.31	31.88	98.45	0.01	0.86	0.02	0.00	0.91	0.02	0.18	0.25	0.66	ilm
MB2-E-10_8-1	0.43	44.65	0.54	0.10	43.70	1.13	5.15	95.70	14.84	30.34	97.19	0.01	0.84	0.02	0.00	0.91	0.02	0.19	0.28	0.64	ilm
MB2-E-10_10-8	0.45	43.16	0.62	0.22	44.93	1.18	5.53	96.09	18.49	28.29	97.94	0.01	0.81	0.02	0.00	0.93	0.02	0.20	0.35	0.59	ilm
MB2-E-10_11-1	0.41	43.34	0.59	0.29	44.43	1.07	5.43	95.56	17.48	28.70	97.31	0.01	0.81	0.02	0.01	0.93	0.02	0.20	0.33	0.60	ilm
MB2-E-10_1-3_2	0.41	47.21	0.52	0.45	42.22	1.17	5.52	97.49	11.45	31.91	98.64	0.01	0.87	0.02	0.01	0.87	0.02	0.20	0.21	0.66	ilm
MB2-E-10_6-3_2	0.32	46.61	0.51	0.08	43.94	1.16	5.14	97.77	13.32	31.96	99.10	0.01	0.86	0.01	0.00	0.90	0.02	0.19	0.25	0.66	ilm

Appendix I (Continued). Rhombohedral Oxide Composition Data

Sample/spot	SiO_2	TiO_2	Al_2O_3	Cr_2O_3	FeO(t)	MnO	MgO	Total	Fe_2O_3[a]	FeO[a]	Corr. Total[a]	Si	Ti	Al	Cr	Fe	Mn	Mg	Fe^{3+} [a]	Fe^{2+} [a]	Phase[b]
MB2-E-11_6-4	0.49	49.25	0.45	0.69	41.02	1.25	4.71	97.86	6.44	35.22	98.51	0.01	0.91	0.01	0.01	0.85	0.03	0.17	0.12	0.73	ilm
MB2-E-11_7-2	0.38	51.08	0.39	0.12	40.01	1.30	4.97	98.25	4.21	36.22	98.67	0.01	0.94	0.01	0.00	0.82	0.03	0.18	0.08	0.74	ilm
MB2-E-11_5-1	0.49	48.41	0.51	0.17	42.32	1.11	4.73	97.74	8.61	34.57	98.60	0.01	0.90	0.01	0.00	0.87	0.02	0.17	0.16	0.71	ilm
MB2-E-11_5-2	0.47	48.31	0.46	0.13	41.98	1.15	4.70	97.20	8.34	34.47	98.03	0.01	0.90	0.01	0.00	0.87	0.02	0.17	0.16	0.72	ilm
MB2-E-11_5-3	0.46	48.58	0.48	0.10	42.29	1.15	4.62	97.68	8.29	34.84	98.51	0.01	0.90	0.01	0.00	0.87	0.02	0.17	0.15	0.72	ilm
MB2-E-11_5-4	0.45	48.58	0.48	0.16	42.29	1.12	4.74	97.81	8.50	34.64	98.66	0.01	0.90	0.01	0.00	0.87	0.02	0.17	0.16	0.71	ilm
MB2-E-11_11-2	0.49	51.49	0.41	0.19	39.44	1.43	5.25	98.70	3.73	36.09	99.08	0.01	0.95	0.01	0.00	0.81	0.03	0.19	0.07	0.74	ilm
MB2-E-11_12-2	0.48	51.19	0.39	0.29	39.71	1.37	5.04	98.47	3.86	36.24	98.86	0.01	0.94	0.01	0.01	0.81	0.03	0.18	0.07	0.74	ilm
MB2-E-11_8-1	0.44	48.18	0.46	0.12	42.47	1.19	4.65	97.52	9.00	34.37	98.42	0.01	0.90	0.01	0.00	0.88	0.02	0.17	0.17	0.71	ilm
MB2-E-11_8-2	0.41	47.90	0.49	0.11	42.93	1.19	4.70	97.73	9.95	33.98	98.72	0.01	0.89	0.01	0.00	0.89	0.02	0.17	0.18	0.70	ilm
MB2-E-11_8-3	0.47	47.74	0.48	0.12	42.89	1.06	4.74	97.50	9.92	33.96	98.49	0.01	0.89	0.01	0.00	0.89	0.02	0.17	0.18	0.70	ilm
MB2-E-11_8-5	0.43	47.75	0.50	0.12	42.37	1.09	4.65	96.90	9.23	34.07	97.83	0.01	0.89	0.01	0.00	0.88	0.02	0.17	0.17	0.71	ilm
MB2-E-11_8-6	0.44	48.06	0.47	0.11	42.72	1.14	4.69	97.63	9.43	34.23	98.58	0.01	0.89	0.01	0.00	0.88	0.02	0.17	0.18	0.71	ilm
MB2-E-11_8-7	0.44	47.79	0.48	0.11	42.49	1.12	4.63	97.06	9.31	34.11	97.99	0.01	0.89	0.01	0.00	0.88	0.02	0.17	0.17	0.71	ilm
MB2-E-12_008	0.36	46.15	0.59	0.09	43.97	1.07	4.57	96.80	12.55	32.68	98.06	0.01	0.86	0.02	0.00	0.92	0.02	0.17	0.24	0.68	ilm
MB2-E-12_009	0.32	45.95	0.59	0.08	44.47	1.01	4.17	96.59	12.46	33.26	97.83	0.01	0.87	0.02	0.00	0.93	0.02	0.16	0.23	0.70	ilm
MB2-E-12_013	0.42	45.05	0.60	0.29	44.50	1.06	5.13	97.06	15.24	30.79	98.58	0.01	0.84	0.02	0.01	0.92	0.02	0.19	0.28	0.64	ilm
MB2-E-12_015	0.41	43.64	0.63	0.21	45.42	1.04	5.08	96.43	17.55	29.63	98.19	0.01	0.81	0.02	0.00	0.94	0.02	0.19	0.33	0.61	ilm
MB2-E-13_002	0.45	48.07	0.50	0.26	42.38	1.19	4.87	97.72	9.44	33.89	98.66	0.01	0.89	0.01	0.01	0.87	0.02	0.18	0.18	0.70	ilm
MB2-E-13_015	0.41	52.12	0.42	0.20	40.33	1.27	4.64	99.37	2.80	37.81	99.65	0.01	0.96	0.01	0.00	0.82	0.03	0.17	0.05	0.77	ilm
MB2-E-13_016	0.43	52.13	0.38	0.23	39.64	1.30	4.51	98.62	1.78	38.03	98.79	0.01	0.97	0.01	0.00	0.82	0.03	0.17	0.03	0.78	ilm
MB2-E-13_017	0.43	52.28	0.39	0.22	39.48	1.40	4.65	98.85	1.84	37.82	99.04	0.01	0.96	0.01	0.00	0.81	0.03	0.17	0.03	0.78	ilm
MB2-E-14_02a	0.47	49.73	1.25	0.58	42.49	1.28	2.63	98.43	3.55	39.30	98.78	0.01	0.93	0.04	0.01	0.88	0.03	0.10	0.07	0.82	ilm
MB2-E-14_11a	0.48	44.77	1.77	0.25	47.56	1.57	1.98	98.38	13.16	35.71	99.70	0.01	0.84	0.05	0.01	0.99	0.03	0.07	0.25	0.74	ilm
MB2-E-15_010	0.35	49.62	0.86	0.75	43.20	1.23	2.14	98.14	3.57	39.99	98.50	0.01	0.94	0.03	0.01	0.91	0.03	0.08	0.07	0.84	ilm

Oxides in wt.%, cations in atoms per unit formula with 3 oxygen basis.

[a] FeO(t) was differentiated into Fe_2O_3 and FeO using a technique of Droop (1987), and corrected total was obtained. The spots also analyzed by Raman spectroscopy are denoted with asterisk. The samples MB2-E- 12-14 were also analyzed, but on grains not analyzed by EPMA.

[b] Phase abbreviations: hem=hematite, ilm=ilmenite.

Appendix J. Olivine Reaction Rim Composition Data

Sample/spot[a]	SiO_2	TiO_2	Al_2O_3	Cr_2O_3	FeO(t)	MnO	MgO	Total	Si	Ti	Al	Cr	Fe	Mn	Mg	Mg_2SiO_4 (Fo)	Fe_2SiO_4 (Fa)
MAm-E-14_002	28.42	0.29	2.48	0.01	61.30	0.71	3.89	97.10	0.96	0.01	0.10	0.00	1.72	0.02	0.19	10.2	89.9
MAm-E-14_007	26.40	1.35	1.95	0.01	61.75	0.71	3.75	95.92	0.90	0.03	0.08	0.00	1.77	0.02	0.19	9.8	90.2
MAm-E-14_009	28.56	0.50	2.48	0.00	61.02	0.75	4.09	97.40	0.96	0.01	0.10	0.00	1.71	0.02	0.20	10.7	89.3
MAm-E-14_013*	28.79	0.47	3.14	0.02	58.11	0.65	5.83	97.00	0.95	0.01	0.12	0.00	1.61	0.02	0.29	15.2	84.8
MAm-E-14_013a*	29.05	0.59	2.52	0.00	58.42	0.63	5.84	97.04	0.96	0.01	0.10	0.00	1.62	0.02	0.29	15.1	84.9
MAm-E-14_014*	31.51	0.52	1.85	0.00	56.72	0.67	5.85	97.13	1.04	0.01	0.07	0.00	1.57	0.02	0.29	15.6	84.5
MAm-E-14_017	4.15	16.81	5.06	0.05	69.65	0.33	1.43	97.48	0.15	0.45	0.21	0.00	2.09	0.01	0.08	3.4	96.5
MAm-E-14_018	13.05	12.55	4.23	0.05	64.75	0.46	3.17	98.26	0.45	0.33	0.17	0.00	1.87	0.01	0.16	8.0	92.0
MAm-E-14_019	24.19	3.98	4.76	0.02	56.47	0.59	5.33	95.35	0.82	0.10	0.19	0.00	1.60	0.02	0.27	14.4	85.6
MAm-E-14_021	2.84	19.72	6.45	0.03	62.29	0.39	0.90	92.63	0.11	0.56	0.29	0.00	1.98	0.01	0.05	2.5	97.5
MAm-E-14_022	2.40	18.17	6.17	0.01	62.83	0.38	0.80	90.76	0.09	0.53	0.28	0.00	2.04	0.01	0.05	2.2	97.8

Oxides in wt.%, cations in atoms per unit formula with 4 oxygen basis. Note: the same calibration as oxide phase was used.

[a] Spots separated by dotted line are the analyses for the same oxide grains. The spots also analyzed by Raman spectroscopy are denoted with asterisk.

Appendix K. Raman Spectra of the Oxide Grains

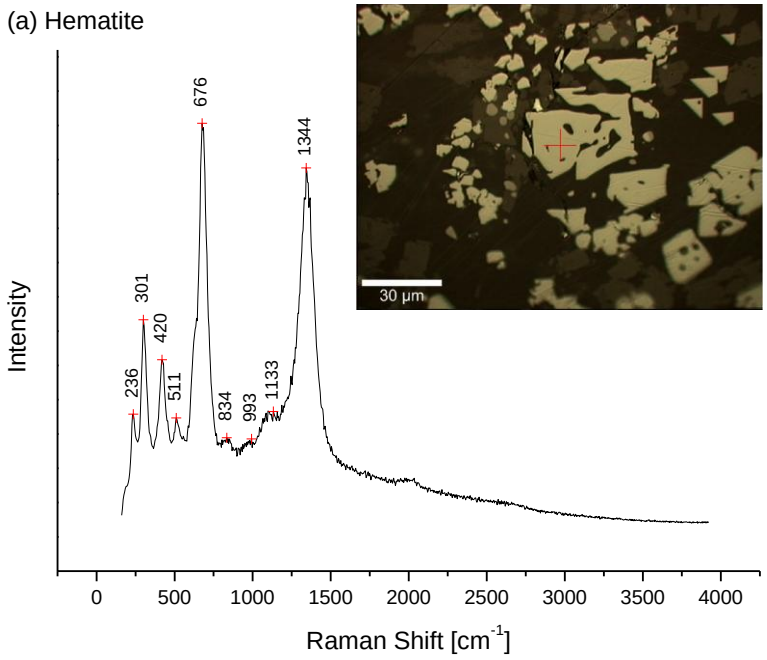

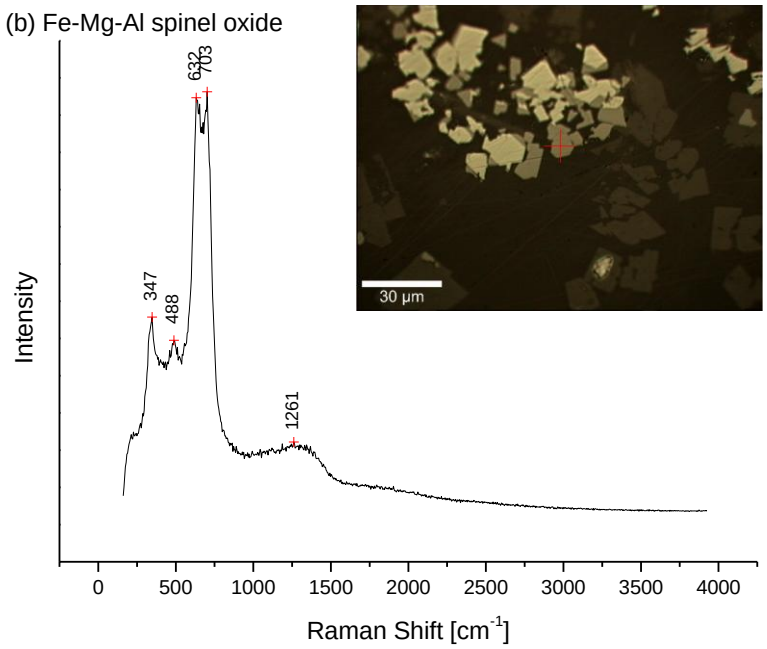

The oxide grains from the Group 1 M-type starting material (MAm-36). The oxides in the Group 1 T-type starting material (MB2-31) showed the same spectra for the same phases. Rough approximations of the peaks were made using a software Origin 6.0 without removing backgrounds.

Appendix K (Continued). Raman Spectra of the Oxide Grains

(c) Type (1) Exsolved Titanomagnetite

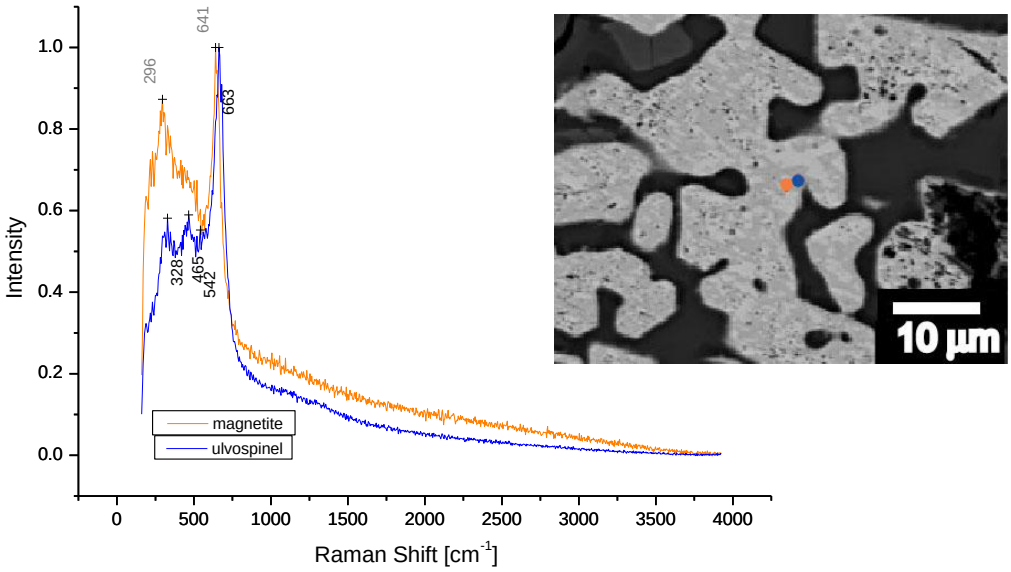

(d) Types (2) and (3) Exsolved Fe-Mg-Al Spinel Oxides

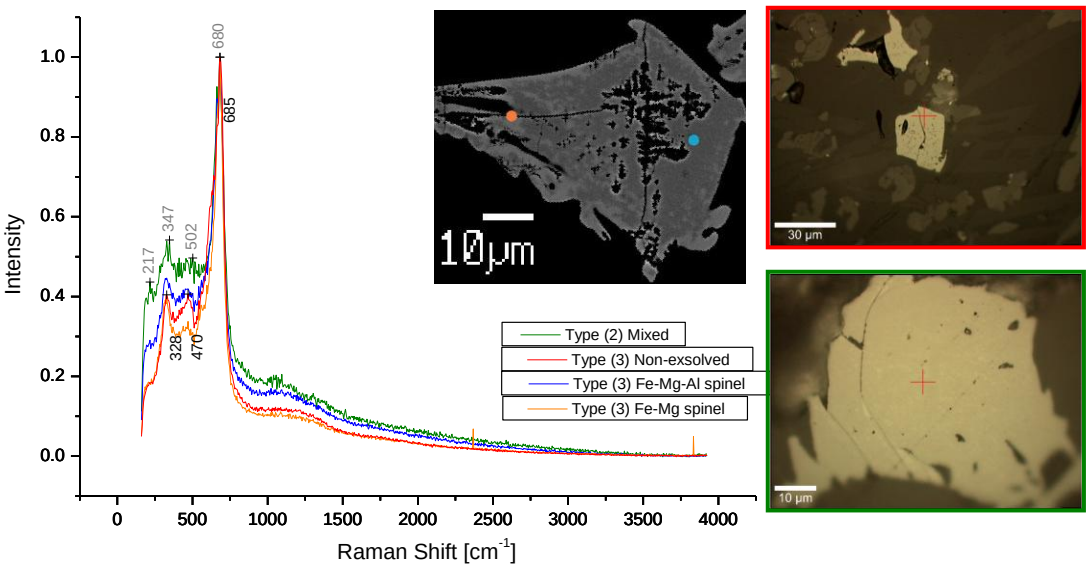

(c) is from the Group 1 M-type annealed run (MAm-E-03). (d) is from the Group 1 T-type annealed run (MB2-E-03). For (c-f), the intensities were normalized by the highest intensity within the spectrum after removing the lowest intensity as a background.

Appendix K (Continued). Raman Spectra of the Oxide Grains

(e) Batch 2 M-type samples

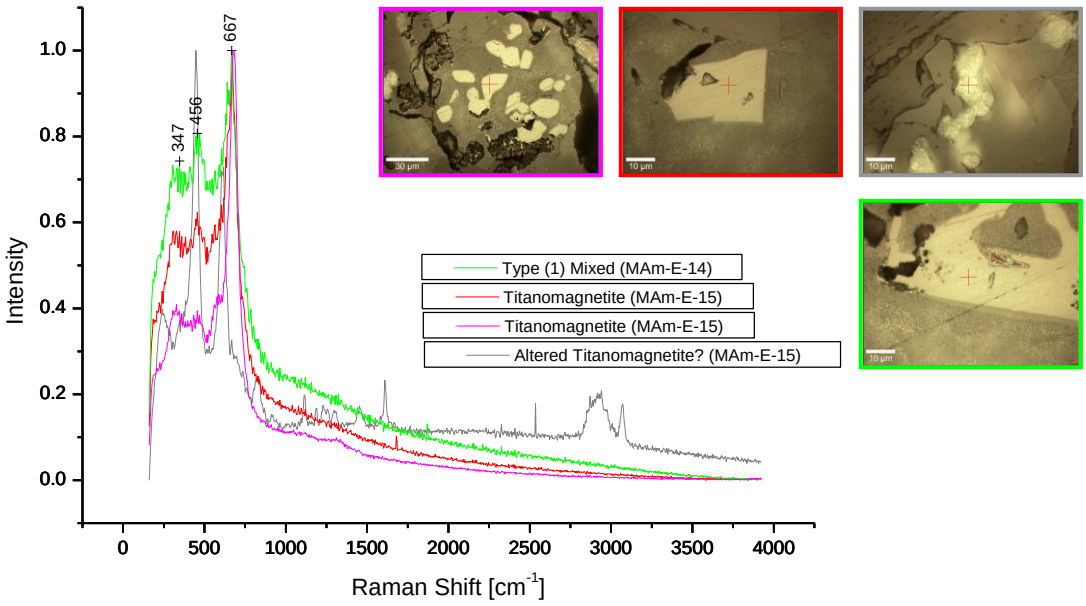

(f) Batch 2 T-type samples

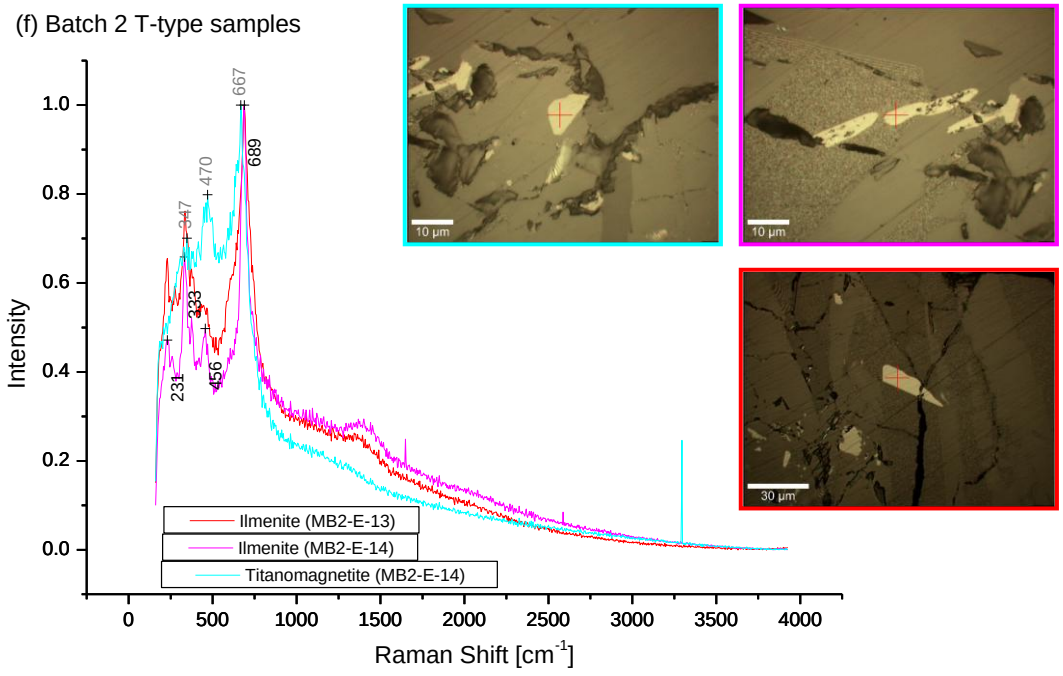

Appendix L. An Example of Intra-Sample Heterogeneity

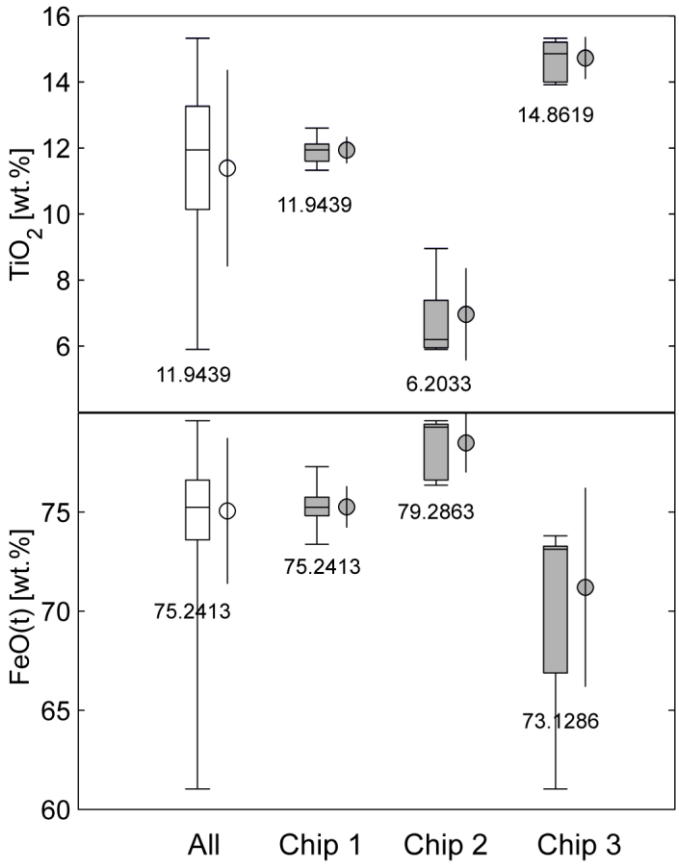

The major element oxides in the Group 2 M-type sample annealed for 21 days (MAm-E-09) shows sample rock chip-dependency of compositional variations. There were three rock chips in the thin sections for quantitative compositional analysis. The numbers of the analyzed oxides for each chip are: 12, 6, and 6 in the order of Chip 1 to 3. The compositional data are also listed in Appendix H. Chip 1 includes analyses MAm-E-09_2 – 7, Chip 2 includes 09_8 and 11, and Chip 3 includes 09_12, 13, and 15-17. Here, the box-and-whisker plots show: middle horizontal bar=median (value denoted on the bottom), box top and bottom=25/75% quartiles, bar top and bottom horizontal bars=maximum and minimum values. Circles are mean values coupled with standard deviations as bars.

Appendix M. X-Ray Element Maps

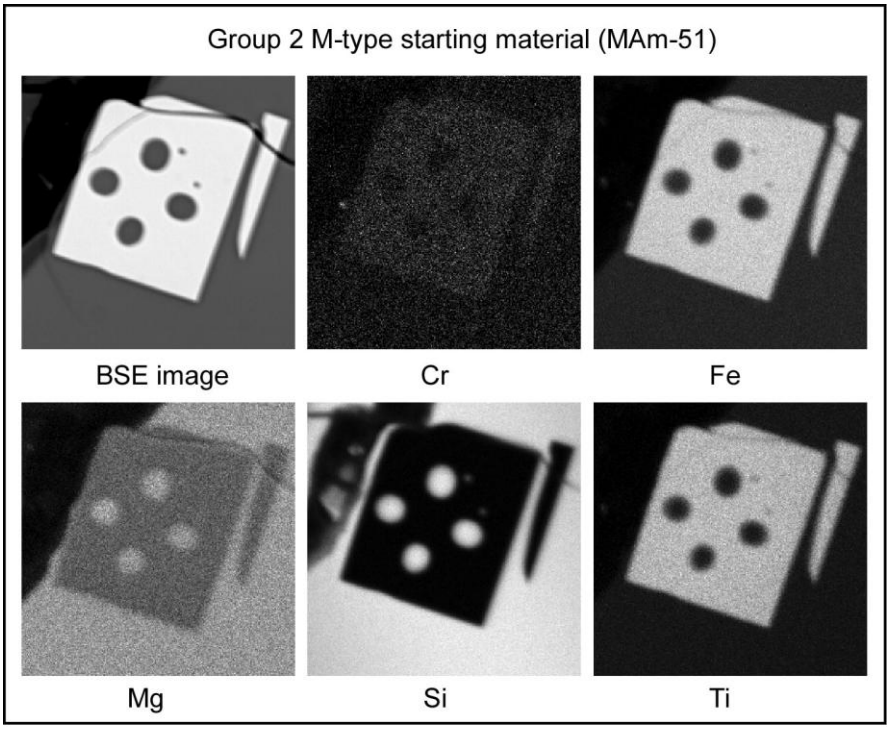

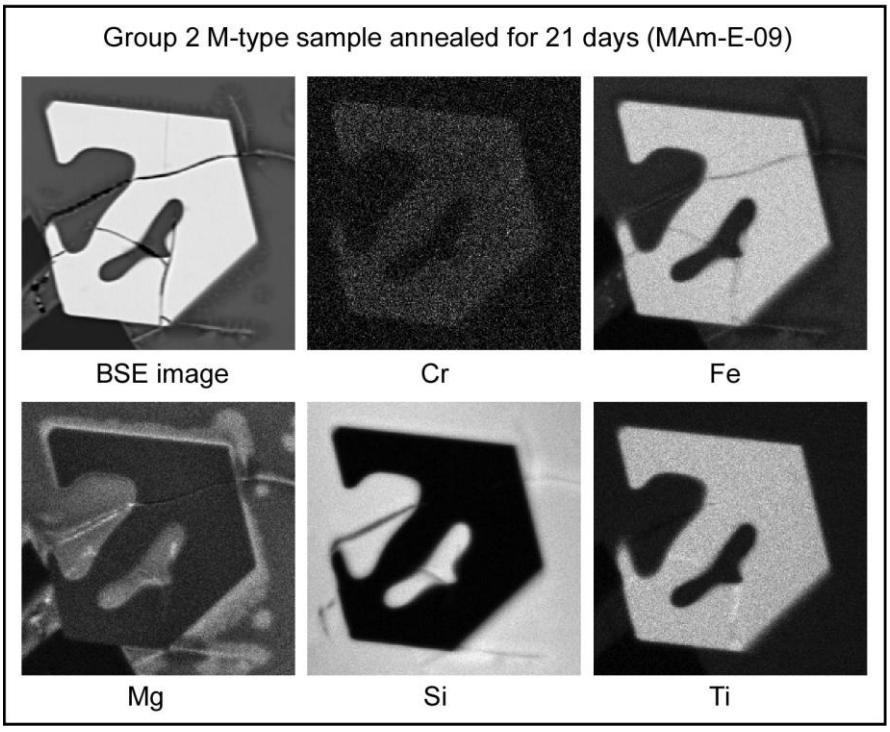

The size of the images is 50 x 50 µm.
Note Mg enrichment in glass following anneal treatment.

Appendix N. M_s-T Curves

Group 1 M-type

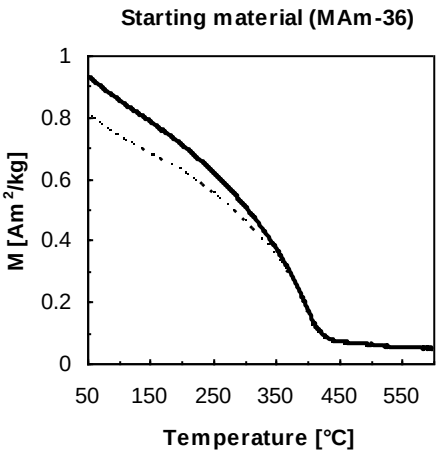

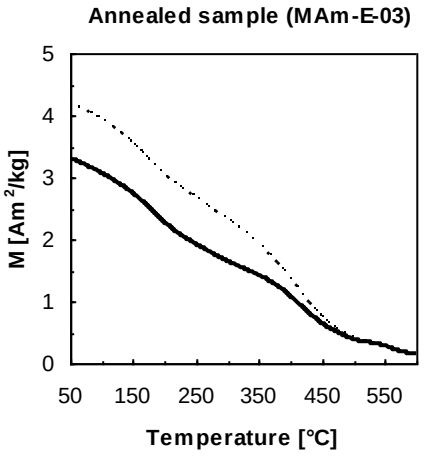

Group 1 T-type

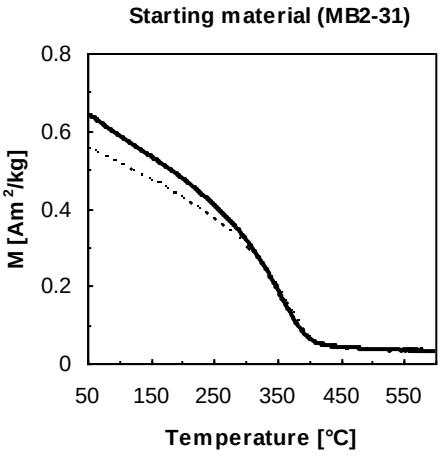

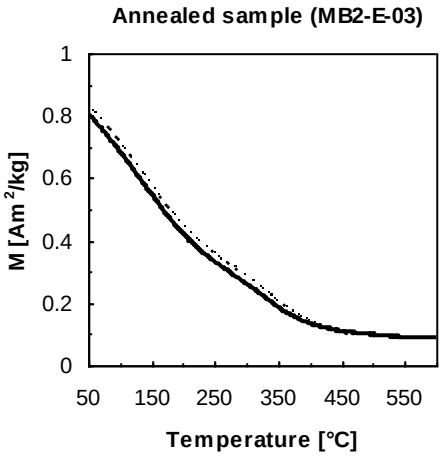

Solid line: Heating
Dotted line: Cooling

Appendix N (Continued). M_s-T Curves

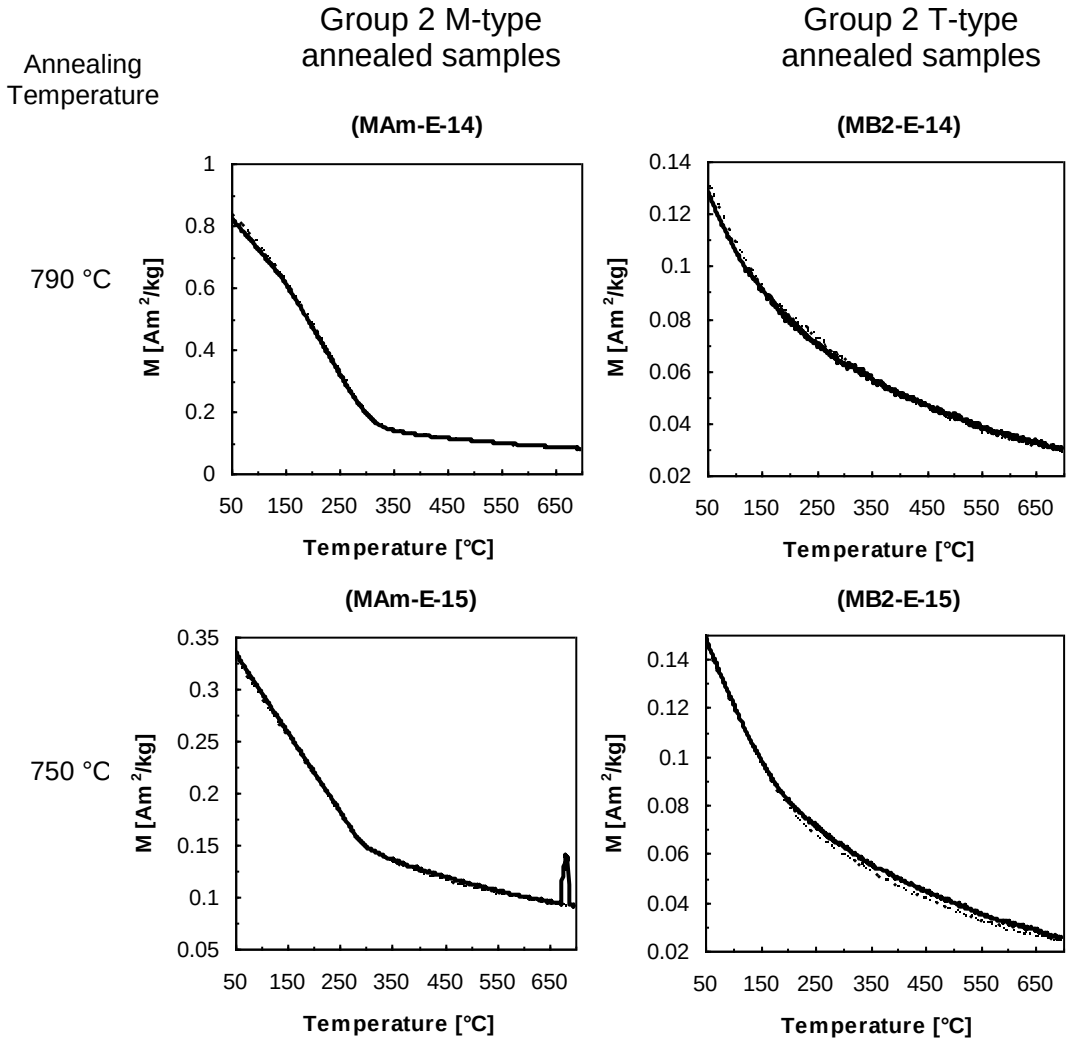

Appendix O. Curie Temperatures Calculated for Oxides Based on their Compositions

Sample	Phase[a]	Exsolution type[c]	Composition[d]	T_C[e] [ºC]
	hem[b]			675
	ilm/gk[b]			-233
	mt[b]			580
	usp/hc[b]			-153
	mgf[b]			440
Group 1				
MAm-36	hem		$Hem_{87}Ilm_{3}Gk_{10}$	557
	femgal		$Mt_{16}Mgf_{68}Hc_{10}Z_{6}$	368
MAm-E-03	mt*	1	$Mt_{90}Mgf_{7}Z_{3}$	548
	timt*	1	$Mt_{60}Usp_{29}Hc_{6}Z_{5}$	316
	femgal*	2	$Mt_{37}Usp_{2}Mgf_{42}Hc_{12}Chr_{7}$	406
	femgal	2	$Mt_{34}Mgf_{49}Hc_{13}Z_{4}$	387
MB2-31	hem		$Hem_{85}Ilm_{5}Gk_{10}$	539
	femgal		$Mt_{16}Mgf_{67}Hc_{8}Z_{9}$	362
MB2-E-03	femg*	2	$Mt_{45}Mgf_{47}Z_{8}$	456
	femgal*	2	$Mt_{44}Mgf_{34}Hc_{13}Z_{9}$	371
	mgf*	3	$Mgf_{84}Hc_{6}Z_{10}$	393
	femgal*	3	$Mt_{34}Mgf_{47}Usp_{8}Hc_{10}Chr_{1}$	380
	femgal	3	$Mt_{17}Mgf_{66}Hc_{8}Z_{9}$	374
Group 2				
MAm-E-14	mt*	1	$Mt_{88}Usp_{9}Z_{3}$	492
	timt*	1	$Mt_{15}Usp_{69}Hc_{12}Z_{4}$	-19
	timt		$Mt_{51}Usp_{38}Mgf_{3}Hc_{8}$	239
MAm-E-15	timt		$Mt_{50}Usp_{40}Mgf_{3}Hc_{7}$	231
MB2-E-14	timt		$Mt_{27}Usp_{43}Mgf_{20}Hc_{8}Chr_{2}$	170
MB2-E-15	timt		$Mt_{26}Usp_{47}Mgf_{15}Hc_{7}Chr_{5}$	141

[a] Phase abbreviations: hem=hematite, ilm=ilmenite, gk=geikielite, mt=magnetite, usp=ulvöspinel, hc=hercynite, mgf=magnesioferrite, femgal=Fe-Mg-Al spinel oxide, timt=titanomagnetite, femg=Fe-Mg spinel oxide, chr=chromite. *=exsolved phases.

[b] Data from Hunt et al. (1995), except for geikielite. Geikielite was assumed to have similar TC as ilmenite, considering their common crystal structure and valances of constituent ions.

[c] Exsolution types: (1) magnetite - Al-bearing titanomagnetite, (2) Fe-Mg-Al spinel oxide - Fe-Mg spinel oxide, (3) Fe-Mg-Al spinel oxide - Al-bearing magnesioferrite.

[d] Based on selected end-members. See section 3.1.1 for abbreviations and formula of end-members.

[e] Curie temperature calculated from oxide composition

REFERENCES

Part I

Acuña, M. H., Connerney, J. E. P., Ness, N. F., Lin, R. P., Mitchell, D., Carlson, C. W., McFadden, J., Anderson, K. A., Rème, H., Mazelle, C., Vignes, D., Wasilewski, P., and Cloutier, P. (1999) Global distribution of crustal magnetization discovered by the Mars Global Surveyor MAG/ER Experiment. Science, 284, 790-793.

Acuña, M. H., Connerney, J. E. P., Wasilewski, P., Lin, R. P., Anderson, K. A., Carlson, C. W., McFadden, J., Curtis, D. W., Mitchell, D., Reme, H., Mazelle, C., Sauvaud, J. A., d'Uston, C., Cros, A., Medale, J. L., Bauer, S. J., Cloutier, P., Mayhew, M., Winterhalter, D., and Ness, N. F. (1998) Magnetic field and plasma observations at Mars: initial results of the Mars Global Surveyor Mission. Science, 279, 1676-1680.

Andersen, D. J., Lindsley, D. H., and Davidson, P. M. (1993) QUILF: A pascal program to assess equilibria among Fe-Mg-Mn-Ti oxides, pyroxenes, olivine, and quartz. Computers and Geosciences, 19, 1333-1350, doi:10.1016/0098-3004(93)90033-2.

Bernal, J., Dasgupta, D., and Mackay, A., Oriented transformation in iron oxides and hydroxides. Nature, 180, 645-647.

Bowles, J. A., Hammer, J., Tatsumi, L., and Brachfeld, S. (2008) Spinel unmixing in Martian analog crustal rocks: implications for the magnetization of Mars, Lunar and Planetary Scence Conference XXXIX.

Bowles, J. A., Hammer, J. E., and Brachfeld, S. A. (2009) Magnetic and petrologic characterization of synthetic Martian basalts and implications for the surface magnetization of Mars. Journal of Geophysical Research, 114, E10003, doi:10.1029/2009JE003378.

Brachfeld, S. A. and Hammer, J. (2006) Rock-magnetic and remanence properties of synthetic Fe-rich basalts: Implications for Mars crustal anomalies. Earth and Planetary Science Letters, 248, 599-617, doi:10.1016/j.epsl.2006.04.015.

Burton, B.P. (1991) The interplay of chemical and magnetic ordering. Reviews in Mineralogy and Geochemistry, Mineralogical Society of America, 25, 303-321.

Connerney, J. E. P., Acuña, M. H., Wasilewski, P., Kletetschka, G., Ness, N. F., Rème, H., Mazelle, C., Vignes, D., Lin, R. P., and Mitchell, D. (2001) The global magnetic field of Mars and implications for crustal evolution. Geophysical Research Letters, 28, 4015-4018.

Connerney, J. E. P., Acuña, M. H., Wasilewski, P., Ness, N. F., Rème, H., Mazelle, C., Vignes, D., Lin, R. P., Mitchell, D., and Cloutier, P. (1999) Magnetic interactions in the ancient crust of Mars. Science, 284, 794-798.

Cuomo, D. M., Tatsumi-Petrohilos, L., Brachfeld, S. A., Bowles, J. A., and Hammer, J. E., (2010) Properties of synthetic Martian basaltic intrusions: implications for Mars crustal anomalies. (in preparation).

Day, R., Fuller, M. D., Schmidt, V. A., (1977) Hysteresis properties of titanomagnetites: grain size and composition dependence. Physics of the Earth Planetary Interiors, 13, 260-266.

Deer, W. A., Howie, R. A., and Zussmann, J. (1962) Rock-Forming Minerals, vol. 5, Non Silicates. Wiley, New York.

de Faria, D. L. A., Venâncio Silva, S., de Oliveira, M. T., (1997) Raman Microspectroscopy of some iron oxides and oxyhydroxides. Journal of Raman Spectroscopy, 28, 873-878.

Donovan, J. J., Kremser, D., and Fournelle, J. H., (2007) Probe for Windows User's Guide and Reference, Enterprise Edition, 355 p., Probe Software, Inc., Eugene, OR.

Droop, G. T. R. (1987) A general equation for estimating Fe^{3+} concentrations in ferromagnesian silicates and oxides from microprobe analyses, using stoichiometric criteria. Mineralogical Magazine, 51, 431-435.

Dunlop, D. J. (2002) Theory and application of the Day plot (M_{rs}/M_s versus H_{cr}/H_c): 1. Theoretical curves and tests using titanomagnetite data, Journal of Geophysical Research, 107(B3), 2056, doi:10.1029/2001JB000486.

Dunlop, D. J., and Özdemir, Ö. (1997) Rock Magnetism: Fundamentals and Frontiers, Cambridge University Press, Cambridge, U. K.

Et-Tabirou, M., Dupré, B., and Gleitzer, C. (1988) Hematite single crystal reduction into magnetite with CO-CO_2. Metallurgical and Materials Transactions B, 19B, 311-317.

Evans, M. E., Krása, D., Williams, W., and Winklhofer, M. (2006) Magnetostatic interactions in a natural magnetite-ulvöspinel system. Journal of Geophysical Research, 111, B12S16, doi:10.1029/2006JB004454.

Evans, M. E., and Wayman, M. L. (1974) An investigation of the role of ultra-fine titanomagnetite intergrowths in paleomagnetism. Geophysical Journal of the Royal Astronomical Society, 36, 1-10.

Frost, B. R. (1991) Stability of oxide minerals in metamorphic rocks. Reviews in Mineralogy and Geochemistry, Mineralogical Society of America, 25, 469-488.

Frost, B. R. and Lindsley, D. H. (1991) Occurrence of iron-titanium oxides in igneous rocks. Reviews in Mineralogy and Geochemistry, Mineralogical Society of America, 25, 433-468.

Frost, B. R., Lindsley, D. H., Andersen, D. J. (1988) Fe-Ti oxidesilicate equilibria: Assemblages with fayalitic olivine. American Mineralogist, 73, 727-740.

Garcia, M. O., Pietruszka, A. J., Rhodes, J. M., and Swanson, K. (2000) Magmatic processes during the prolonged Pu'u 'O'o eruption of Kilauea volcano, Hawaii. Journal of Petrology, 41, 967-990.

Ghiorso, M. S. and Sack, R. O. (1991) Thermochemistry of the oxide minerals. Reviews in Mineralogy and Geochemistry, Mineralogical Society of America, 25, 221–264.

Ghiorso, M. S., and Sack, O. (1995) Chemical mass transfer in magmatic processes. IV. A revised and internally consistent thermodynamic model for the interpolation and extrapolation of liquid-solid equilibria in magmatic systems at elevated temperatures and pressures. Contributions to Mineralogy and Petrology, 119, 197-212, doi:10.1007/BF00307281.

Gibbs, J. W. (1961) The Scientific papers of J. Willard Gibbs, 1. Dover Publications, New York, N.Y., 434 pp.

Golla-Schindler, U., O'Neill, H. St.C., and Putnis, A. (2005) Direct observation of spinodal decomposition in the magnetite-hercynite system by susceptibility measurements and transmission electron microscopy. American Mineralogist, 90, 1278-1283.

Grommé, C. S., Wright, T. L., and Peck, D. L. (1969) Magnetic Properties and Oxidation of Iron-Titanium Oxide Minerals in Alae and Makaopuhi Lava Lakes, Hawaii. Journal of Geophysical Research, 74, 5277-5293.

Haggerty, S. E. (1991) Oxide textures; a mini-atlas. Reviews in Mineralogy and Geochemistry, Mineralogical Society of America, 25, 129-219.

Hammer, J. E. (2006) Influence of fO2 and cooling rate on the kinetics and energetics of Fe-rich basalt crystallization, Earth and Planetary Science Letters, 248, 618-637, doi:10.1016/j.epsl.2006.04.022.

Hargraves, R. B., Knudsen, J. M., Madsen, M. B., and Bertelsen, P. (2001) Finding the right rocks on Mars. Eos Transaction AGU, 82, 292-293.

Harrison, R. J. (2006) Microstructure and magnetism in the ilmenite-hematite solid solution: a Monte Carlo simulation study. American Mineralogist, 91, 1006-1023.

Harrison, R. J. and Putnis, A. (1999) The magnetic properties and crystal chemistry of oxide spinel solid solutions. Surveys in Geophysics, 19, 461-520.

Harrison, R. J., Dunin-Borkowski, R. E., and Putnis, A. (2002) Direct imaging of nanoscale magnetic interactions in minerals. Proceedings of National Academy of Science U.S.A., 99, 16556-16561.

Hayes, P. and Grieveson, P. (1981) Microstructural changes on the reduction of hematite to magnetite. Metallurgical and Materials Transactions B, 12B, 579-587.

Hunt, C. P., Moskowitz, B. M., and Banerjee, S. K. (1995) Magnetic properties of rocks and minerals. Rock Physics and Phase Relations: A Handbook of Physical Constants AGU Reference Shelf 3, 189-204.

Kawai, N. (1956) Exsolution of titanomagnetites and its effect on rock-magnetism III. Proceedings of the Japanese Academy, 32, 464-468.

Kilinc, A., Carmichael, I. S. E., Rivers, M. L., and Sack, R. O. (1983) The ferric-ferrous ration of natural silicate liquids equilibrated in air. Contributions for Mineralogy and Petrology, 83, 136-140, doi:10.1007/BF00373086.

Krása, D., Wilkinson, C. D. W., Gadegaard, N., Kong, X., Zhou, H., Roberts, A. P., Muxworthy, A. R., and Williams, W. (2009) Nanofabrication of two-dimensional arrays of magnetite particles for fundamental rock magnetic studies. Journal of Geophysical Research, 114, B02104, doi:10.1029/2008JB006017.

Lindsley, D. H. (1981) Some experiments pertaining to the magnetite-ulvöspinel miscibility gap. American Mineralogist, 66, 759-762.

McEnroe, S. A., Robinson, P., Langenhorst, F., Frandsen, C., Terry, M. P., and Ballaran, T. B. (2007) Magnetization of exsolution intergrowths of hematite and ilmenite: mineral chemistry, phase relations, and magnetic properties of hemo-ilmenite ores with micron-to nanometer-scale lamellae from Allard Lake, Quebec. Journal of Geophysical Research, 112, B10103, doi: 10.1029/2007JB004973.

McSween, H. Y. Jr., Taylor, G. J., and Wyatt, M. B. (2009) Elemental composition of the Martian crust. Science, 324, 736, doi: 10.1126/science.1165871.

Merrill, R. T. and McElhinny, M. W. (1983) The Earth's magnetic field: its history, origin, and planetary perspective, Academic Press, Orlando.

Muan, A., Hauck, J., and Löfall, T. (1972) Equilibrium studies with a bearing on lunar rocks. Proceedings of the Third Lunar Science Conference, Supplement 3. Geochimica et Cosmochimica Acta, 1, 185-196.

Muxworthy, A., Williams, W., and Virdee, D. (2003) Effect of magnetostatic interactions on the hysteresis parameters of single-domain and pseudosingle-domain grains. Journal of Geophysical Research, 108(B11), 2517, doi:10.1029/2003JB002588.
Price, G. D. (1980) Exsolution microstructures in titanomagnetites, and their magnetic significance. Physics of the Earth Planetary Interiors, 23, 2-12.
Price, G. D. (1981) Subsolidus phase relations in the titanomagnetite solid solution series. American Mineralogist, 66, 751-758.
Purucker, M., Ravat, D., Frey, H., Voorhies, C., Sabaka, T., and Acuna, M. (2000) An altitude-normalized magnetic map of Mars and its interpretation. Geophysical Research Letters, 27, 249-2452.
Putnis, A. (1992) Introduction to Mineral Sciences, 206 p. Cambridge University Press, Cambridge.
Smith, P. P. K. (1980) Spinodal decomposition in titanomagnetite. American Mineralogist 65, 1038-1043.
Swann, P. R. and Tighe, N. J. (1977) High voltage microscopy of the reduction of hematite to magnetite. Metallurgical and Materials Transactions, 8B, 479-487.
Turnock, A. C. and Eugster, H. P. (1962) Fe-Al oxides: phase relations below 1000 °C. Journal of Petrology, 3, 533-565.
Vincent, E. A. and Phillips, R. (1954) Iron-titanium oxide minerals in layered gabbros of the Skaergaard intrusion, East Greenland. Geochimica et Cosmochimica Acta, 6, l-26.
Wang, A., Kuebler, K. E., Jolliff, B. L., Haskin, L. A., (2004) Raman spectroscopy of Fe-Ti-Cr-oxides, case study: Martian meteorite EETA79001. American Mineralogist, 89, 665-680.
Weinbruch, S. Styrsa, V., and Müller, W. F. (2003) Exsolution and coarsening in iron-free clinopyroxene during isothermal annealing. Geochimica et Cosmochimica Acta, 67, 5071-5082, doi:10.1016/S0016-7037(03)00205-9.
Yund, R. A. and McCallister, R. H. (1970) Kinetics and mechanisms of exsolution. Chemical Geology, 6, 5-30.

Part II

Akimoto, S. (1962) Magnetic properties of FeO-Fe_2O_3-TiO_2 system as a basis of rock magnetism. Journal of Physical Society of Japan, 17 Suppl. B-1, 706-710.
Blasse, G. (1964) Crystal chemistry and some magnetic properties of mixed metal oxides with spinel structure. Philips Research Report Supplement, 3, 1-139.
de Faria, D. L. A., Venâncio Silva, S., and de Oliveira M. T. (1997) Raman microspectroscopy of some iron oxides and oxyhydroxides. Journal of Raman Spectroscopy, 28, 873-878.
Degiorgi, L., Blatter-Mörke, I., and Wachter, P. (1987) Magnetite: Phonon modes and the Verwey transition. Physical Review B, 35, 5421-5424.
Gasparov, L. V., Tanner, D. B., Romero, D. B., Berger, H., Margaritondo, G., and Forró, L. (2000) Infrared and Raman studies of the Verwey transition in magnetite. Physical Review B, 62, 7939-7944.

Graves, P. R., Johnston, C., and Campaniello, J. J. (1988) Raman scattering in spinel structure ferrites. Materials Research Bulletin, 23, 1651-1660.
Gilder, S. A. and Le Goff, M. (2008) Systematic pressure enhancement of titanomagnetite magnetization. Geophysical Research Letters, 35, L10302, doi:10.1029/2008GL033325.
Herd, C. D. K. (2006) Insights into the redox history of the NWA 1068/1110 Martian basalt from mineral equilibria and vanadium oxybarometry. American Mineralogist, 91, 1616-1627.
Herd, C. D. K., Borg, L. E., Jones, J. H., and Papike, J. J. (2002) Oxygen fugacity and geochemical variations in the Martian basalts: implications for Martian basalt petrogenesis and the oxidation state of the upper mantle of Mars, Geochimica et Cosmochimica Acta, 66, 2025-2036.
Kakol, Z., Sabol, J., and Honig, J. M. (1991) Cation distribution and magnetic properties of titanomagnetites $Fe_{3-x}Ti_xO_4$, $0 \leq x < 1$. Physical Review B, 43, 649-654.
O'Reilly, W. (1984) Rock and Mineral Magnetism, 222 pp., Blackie, Glasgow.
Popp, J. and Schmitt, M. (2004) Raman spectroscopy breaking terrestrial barriers. Journal of Raman Spectroscopy, 35, 429-432.
Richards, J. C. W., O'Donovan, J. B., Hauptmann, Z., O'Reilly, W., and Creer, K. M. (1973) A magnetic study of titanomagnetite substituted by magnesium and aluminium. Physics of the Earth and Planetary Interiors, 7, 437-444.
Rutherford, M. J. and Hermes, D. O. (1984) Melatroctolite-anorthositic gabbro complex, Cumberland, Rhode Island: Petrology, origin, and regional setting. Geological Society of America Bulletin, 95, 844-854.
Sharma, S. K. (2007) New trends in telescopic remote Raman spectroscopic instrumentation. Spectrochimica Acta Part A, 68, 1008-1022.
Shebanova, O. N. and Lazor, P. (2003a) Raman study of magnetite (Fe_3O_4): laser-induced thermal effects and oxidation. Journal of Raman Spectroscopy, 34, 845-852.
Shebanova, O. N. and Lazor, P. (2003b) Raman spectroscopic study of magnetite ($FeFe_2O_4$): a new assignment for the vibrational spectrum. Journal of Solid State Chemistry, 174, 424-430.
Stacy, F. D. and Banerjee, S. K. (1974) The Physical Principles of Rock Magnetism. 195 pp., Elsevier Science, New York.
Verble, J. L. (1974) Temperature-dependent light-scattering studies of the Verwey transition and electronic disorder in magnetite. Physical Review B, 9, 5236-5248.
Verwey, E. J., Haayman, P. W., and Romeijn, F. C. (1947) Physical properties and cation arrangement of oxides with spinel structures II. electronic conductivity. Journal of Chemical Physics, 15, 181.
Wanamaker, B. J. and Moskowitz, B. M. (1994) Effect of nonstoichiometry on the magnetic and electrical properties of synthetic single crystal $Fe_{2.4}Ti_{0.6}O_4$. Geophysical Research Letters, 21, 983–986.
Wang, A., Kuebler, K., Jolliff, B., and Haskin, L. A. (2004a) Mineralogy of a Martian meteorite as determined by Raman spectroscopy. Journal of Raman Spectroscopy, 35, 504-514.

Wang, A., Kuebler, K. E., Jolliff, B. L., and Haskin, L. A. (2004b) Raman spectroscopy of Fe-Ti-Cr-oxides, case study: Martian meteorite EETA79001. American Mineralogist, 89, 665-680.
White, W. B. and DeAngelis, B. A. (1967) Interpretation of the vibrational spectra of spinels. Spectrochimica Acta Part A, 23, 985-995.